# Cold Nuclear Matter Effects on Heavy Quark Production in Relativistic Heavy Ion Collisions

A Dissertation Presented

by

**John Matthew Durham**

to

The Graduate School

in Partial Fulfillment of the Requirements

for the Degree of

**Doctor of Philosophy**

in

**Physics**

Stony Brook University

May 2011





ProQuest LLC.
789 East Eisenhower Parkway
P.O. Box 1346
Ann Arbor, MI 48106 - 1346

**Stony Brook University**

The Graduate School

## John Matthew Durham

We, the dissertation committee for the above candidate for the Doctor of Philosophy degree, hereby recommend acceptance of this dissertation.

Thomas K. Hemmick – Dissertation Advisor
Professor, Department of Physics and Astronomy

Derek Teaney – Chairperson of Defense
Professor, Department of Physics and Astronomy

Michael Rijssenbeek
Professor, Department of Physics and Astronomy

David P. Morrison
Physicist, Brookhaven National Laboratory

This dissertation is accepted by the Graduate School.

Lawrence Martin
Dean of the Graduate School

Abstract of the Dissertation

# Cold Nuclear Matter Effects on Heavy Quark Production in Relativistic Heavy Ion Collisions

by

**John Matthew Durham**

**Doctor of Philosophy**

in

**Physics**

Stony Brook University

2011

The experimental collaborations at the Relativistic Heavy Ion Collider (RHIC) have established that dense nuclear matter with partonic degrees of freedom is formed in collisions of heavy nuclei at $\sqrt{s_{NN}} = 200$ GeV. Information from heavy quarks has given significant insight into the dynamics of this matter. Charm and bottom quarks are dominantly produced by gluon fusion in the early stages of the collision, and thus experience the complete evolution of the medium. The production baseline measured in $p + p$ collisions can be described by fixed order plus next to leading log perturbative QCD calculations within uncertainties. In central Au+Au collisions, suppression has been measured relative to the yield in

$p + p$ scaled by the number of nucleon-nucleon collisions, indicating a significant energy loss by heavy quarks in the medium. The large elliptic flow amplitude $v2$ provides evidence that the heavy quarks flow along with the lighter partons. The suppression and elliptic flow of these quarks are in qualitative agreement with calculations based on Langevin transport models that imply a viscosity to entropy density ratio close to the conjectured quantum lower bound of $1/4\pi$. However, a full understanding of these phenomena requires measurements of cold nuclear matter (CNM) effects, which should be present in Au+Au collisions but are difficult to distinguish experimentally from effects due to interactions with the medium.

This thesis presents measurements of electrons at midrapidity from the decays of heavy quarks produced in $d$+Au collisions at RHIC. A significant enhancement of these electrons is seen at a transverse momentum below 5 GeV/$c$, indicating strong CNM effects on charm quarks that are not present for lighter quarks. A simple model of CNM effects in Au+Au collisions suggests that the level of suppression in the hot nuclear medium is comparable for all quark flavors.

## Dedication

*Col. 3:23*

# Contents

# List of Figures

# List of Tables

# Acknowledgements

First off, thanks to my advisor and friend Tom Hemmick, whose enthusiasm for science was a constant inspiration for me, and will continue to be in the years to come. Many thanks are also due to Axel Drees and Barbara Jacak for the years of steady guidance they provided me.

All of the other graduate students in our group also deserve recognition. Sun Jiayin provided the finesse the HBD needed to be successful, and Sarah Campbell was constantly patient and helpful with my first attempts to analyze PHENIX data. The entire Stony Brook group has been a source of strength and friendship that I will never forget.

Finally, I have to thank my family, epsecially Abbey, for their constant support throughout my graduate career at Stony Brook.

# Chapter 1

# Introduction

It is now generally believed that Au+Au collisions at ultrarelativistic energies produce the quark-gluon plasma (QGP). In this unique state of matter, quarks and gluons are no longer confined inside color neutral hadrons, but instead exist in a strongly-coupled fluid. The creation and characterization of QGP is the ultimate goal of the physics program at the Relativistic Heavy Ion Collider (RHIC).

## 1.1 Relativistic Heavy Ion Collisions

Quantum Chromodynamics has been established as the correct theory of the strong interaction. At normal temperatures, the quarks and gluons that carry the QCD color charge are confined inside color neutral hadrons. However, at high temperature or density, QCD matter is expected to undergo a phase transition into a plasma of deconfined quarks and gluons [1] (see Fig. 1.1). Calculations on the lattice show the temperature of this transition to be $\sim$ 170 MeV, with a corresponding energy density of $\sim$ 1 GeV/fm$^3$ [2].

Ultrarelativistic collisions of heavy nuclei provide the conditions necessary for QGP formation. The energy density in the region of the collision of two Au nuclei at $\sqrt{s_{NN}} = 200$ GeV is expected to be at least 5 GeV/fm$^3$, well exceeding the critical density set by lattice calculations [3]. Therefore the phase transition of nuclear matter to a deconfined plasma is accessible in the laboratory. The Relativisitc Heavy Ion Collider (RHIC)was built for the express purpose of creating and studying the transition of normal nuclear matter to QGP.

The suite of measurements from RHIC suggest that a new form of matter with partonic degrees of freedom has been formed. Summaries of early measurements at RHIC are collected in [3], [4], [5], [6].

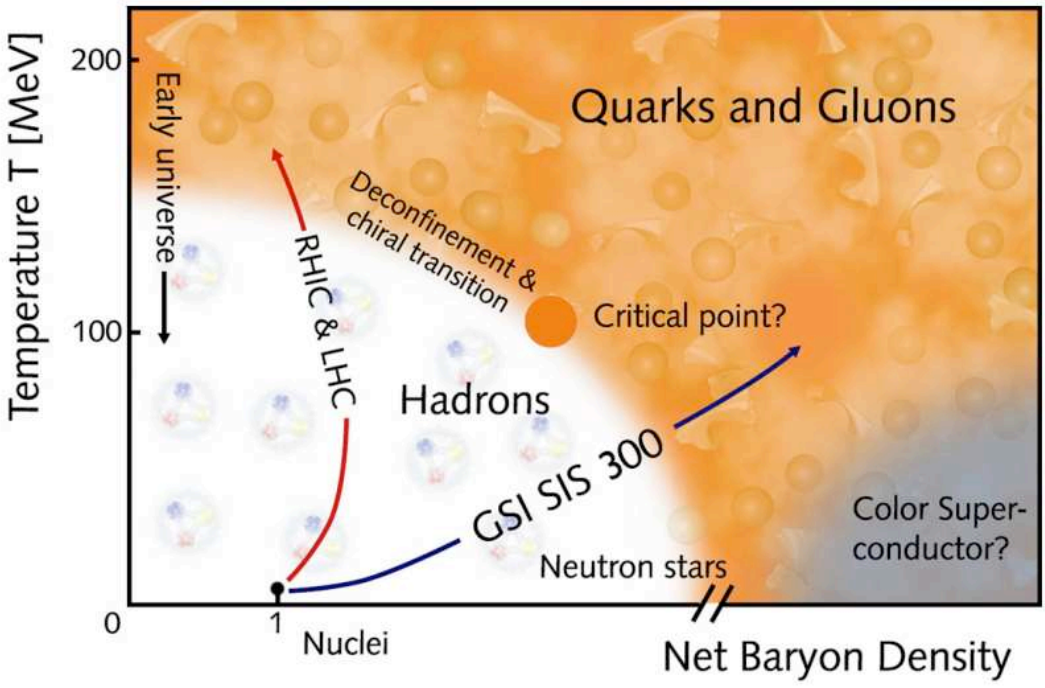


Figure 1.1: A schematic of the phases Quantum Chromodynamics.

### 1.1.1 Light Quarks in Nuclear Collisions

Since bare quarks themselves are not directly measurable due to confinement, the properties of the quarks produced in collisions of heavy nuclei must be inferred from the spectra of color neutral particles that are formed after hadronization. Measurement of charged and neutral pions are often interpreted as representing light quarks, as these hadrons are composed of $u$ and $d$ quarks and antiquarks.

As simple observable that illustrates the difference between nuclear collisions and elementary $p+p$ interactions is the nuclear modfication factor $R_{AA}$, defined as the ratio of the particle yield measured in $A+A$ collisions to the yield in $p+p$ scaled by the number of nucleon-nucleon collisions:

$$R_{AA} = \frac{dN_{AA}/dp_T}{< N_{coll} > \times dN_{pp}/dp_T} \tag{1.1}$$

If $R_{AA} = 1$, the particle yield in $A+A$ is well described by a superposition of independent nucleon-nucleon collisions. Fig. 1.2 shows the neutral pion $R_{AA}$ as a function of $p_T$ over a range of centralities. In the most peripheral centrality bin (80-92%), little or no change in the shape or magnitude of the pion spectrum is observed. However, as the collisions become more central,

a strong suppression is observed over a wide range of transverse momentum. This mechanism for this suppression is attributed to parton energy loss in the medium created in central Au+Au collisions [8], [9], [10].

### 1.1.2 Heavy Quarks in Nuclear Collisions

The masses of charm and bottom quarks (about 1.3 and 4.2 GeV/$c^2$, respectively) are large enough to ensure that the dominant production mechanism is gluon-gluon fusion in the early stages of the nuclear collision (see Fig. 1.3 for leaing order production diagrams). This makes heavy quarks a much cleaner probe than the lighter quarks, which can come from a variety of soft and hard processes that occur throughout the system's lifetime.

Matsui and Satz predicted the suppression of $J/\psi$ mesons in collisions of heavy nuclei as a signal of deconfinement, reasoning that Debye color screening in the medium would inhibit coalescence of the $c\overline{c}$ pair [12]. Indeed, a significant suppression of the $J/\psi$ is observed in central Au+Au collisions at 200 GeV [13]. Fig. 1.4 shows this suppression at a function of the $J/\psi$ transverse momentum at mid and forward rapidity. Note that the suppression increases at forward rapidities.

The dynamics of the $J/\psi$ in relativistic heavy ion collisions are far from simple. The simple picture of production then dissociation in QGP leaves out many important effects. Recombination of uncorrelated $c\overline{c}$ pairs at freeze-out can compete with dissociation of correlated pairs in the plasma [14], [15]. Feed-down of $J/\psi$ mesons from higher states, which is a significant source of the total amount of $J/\psi$ measured in $p+p$ [16], further complicates interpretation of the data.

#### Open Heavy Flavor

Mesons containing open heavy flavor (namely the $D$ and $B$ families) are another heavy probe of the QCD medium, without many of the complications that come with quarkonia. Tevatron data shows that bottom production in $p\overline{p}$ collisions at $\sqrt{s} = 1.8$ TeV is well described by perturbative QCD calculations [17]. At slightly higher energies, the measured charm cross section exceeds the predicted value by $\sim$50%, but agrees within large theoretical uncertainties [18].

At RHIC, open charm and bottom are primarily measured through their decay channels to leptons. The decay $D^{\pm} \rightarrow e^{\pm} + X$ has a branching ratio of 17.2%, while $B^{\pm} \rightarrow e^{\pm} + X$ has a branching ratio of 6.9% [19]. Fig. 1.5 shows the spectrum of electrons from heavy flavor decays produced in $p+p$ collisions

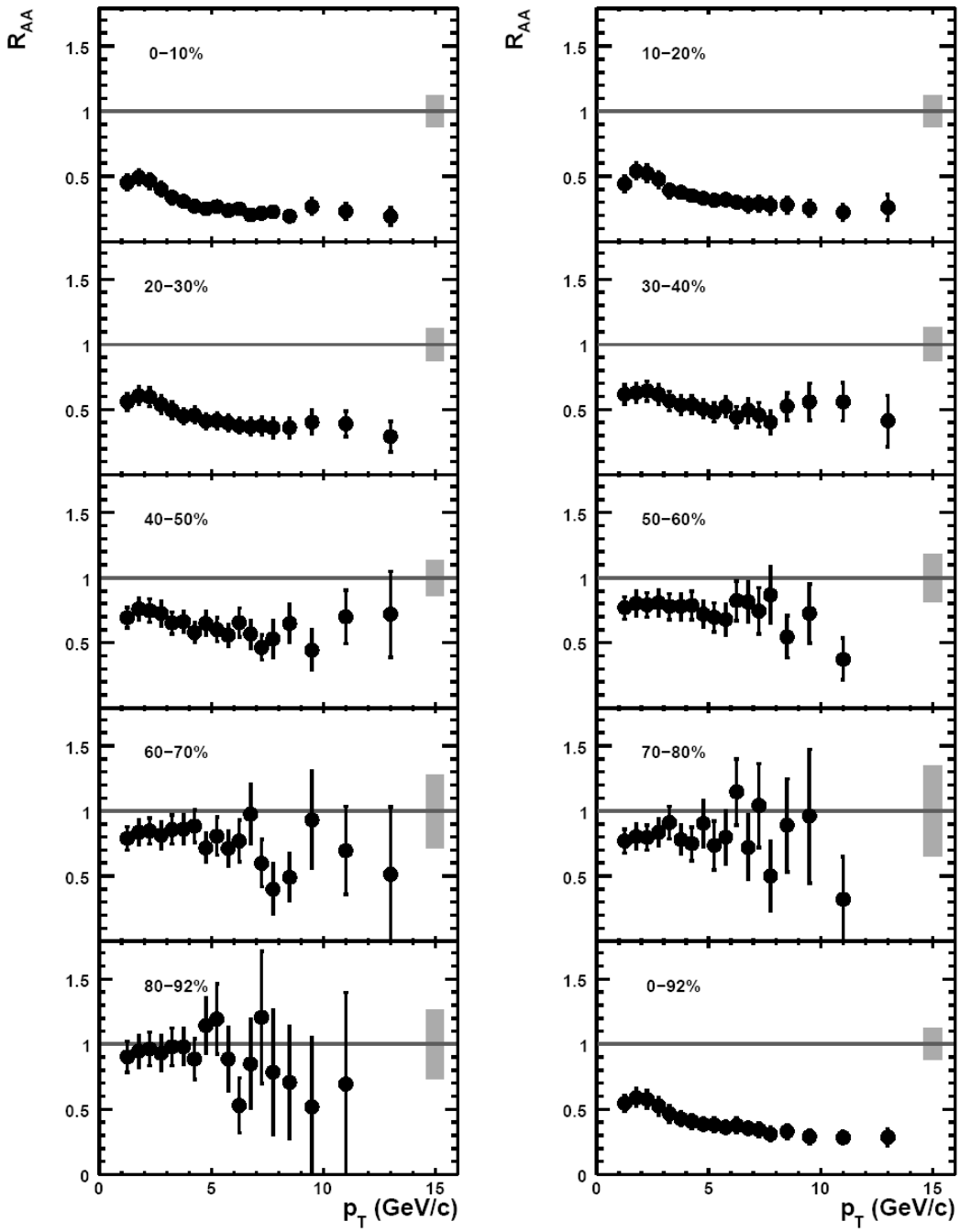


Figure 1.2: The $\pi^0$ nuclear modification factor $R_{AA}$ as a function of $p_T$ for Au+Au collisions at $\sqrt{s_{NN}} = 200$ GeV [7].

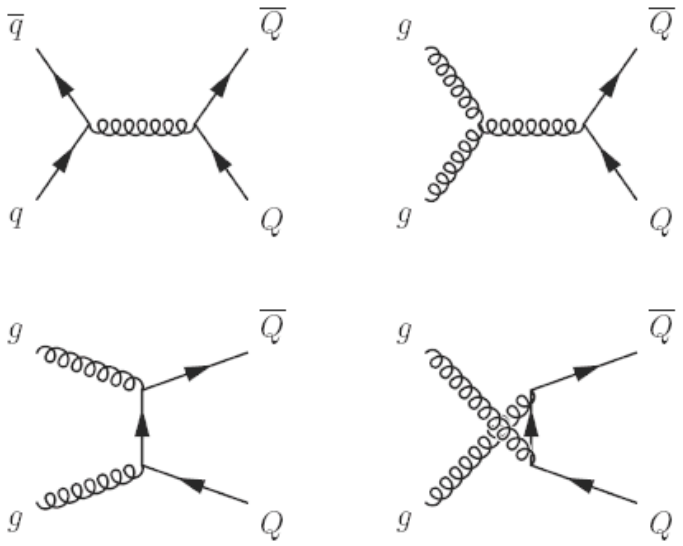


Figure 1.3: Leading order $Q\overline{Q}$ production diagrams.

at $\sqrt{s} = 200$ GeV [21]. The bottom panel shows a comparison with a first-order-plus-next-to-leading-log (FONLL) perturbative QCD calculation [20]. The measured cross section is higher than the calculation by a factor of about 1.7, similar to the comparison with Tevatron data. Above $p_T = 1.6$ GeV, the pQCD shape and data are in good agreement.

Heavy quarks are expected to radiate less energy when traversing the QGP, as compared to lighter quarks. Their large mass leads to a suppression of gluon radiation at forward angles $\theta < M_Q/E_Q$, known as the "dead cone effect" [11]. This effect leads to the expectation that $R_{AA}^{u,d} < R_{AA}^{c} < R_{AA}^{b}$.

With this important $p+p$ baseline measurement in hand, the heavy flavor electron nuclear modification factor can be calculated with Eqn. 1.1. The measurement of $R_{AA}$ and comparisons with the $\pi^0$ and several theoretical models are shown in Fig. 1.6 [22].

Contrary to expectation, a large supression of electrons from heavy flavor is observed in central Au+Au collisions, which is consistent with the $\pi^0 R_{AA}$ for $p_T > 5$ GeV/$c$. At lower momentum, however, the electrons exhibit less suppression that the light quarks. This technique of measuring heavy quarks through their decay to electrons does not allow separation of the contributions from charm quarks and bottom quarks. However, perturbative QCD calculations and measurements of correlations between hadrons and electrons

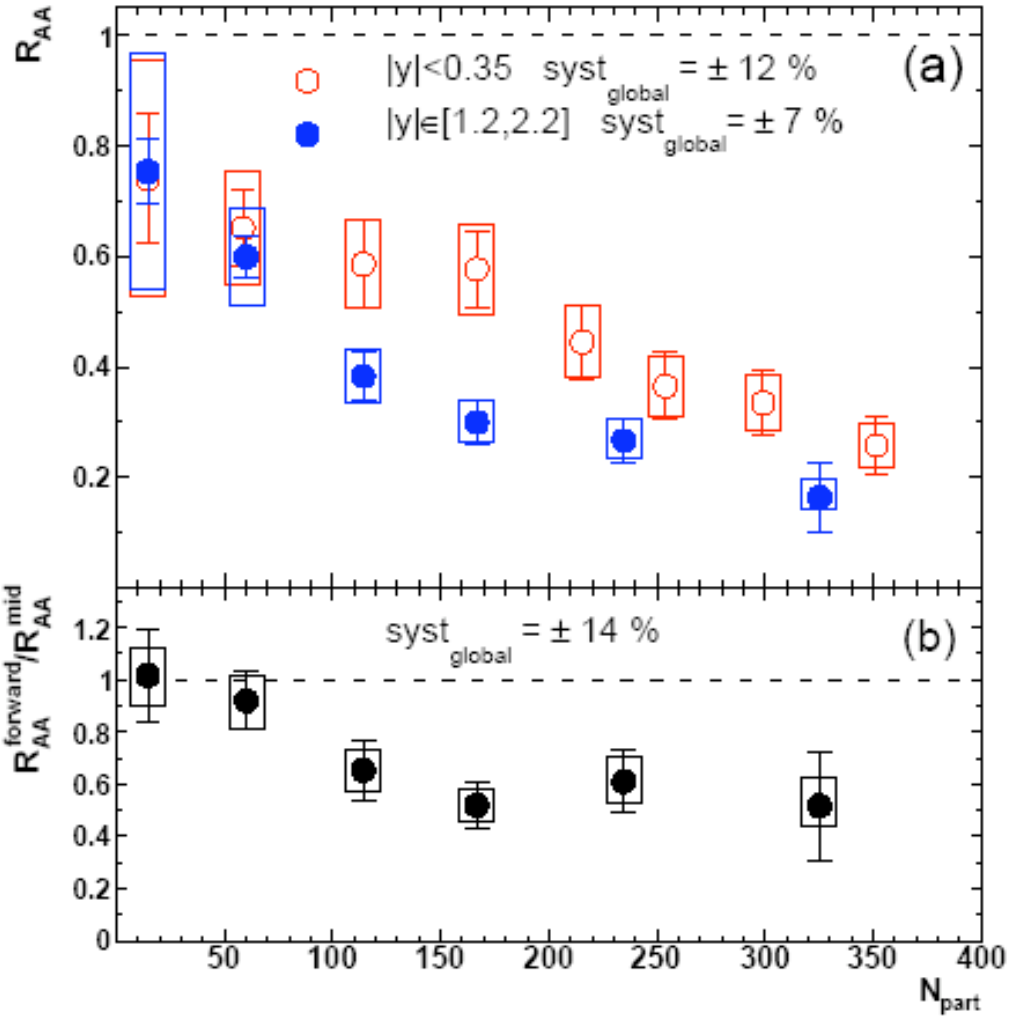


Figure 1.4: The $J/\psi$ nuclear modification factor in Au+Au collisions at 200 GeV [13].

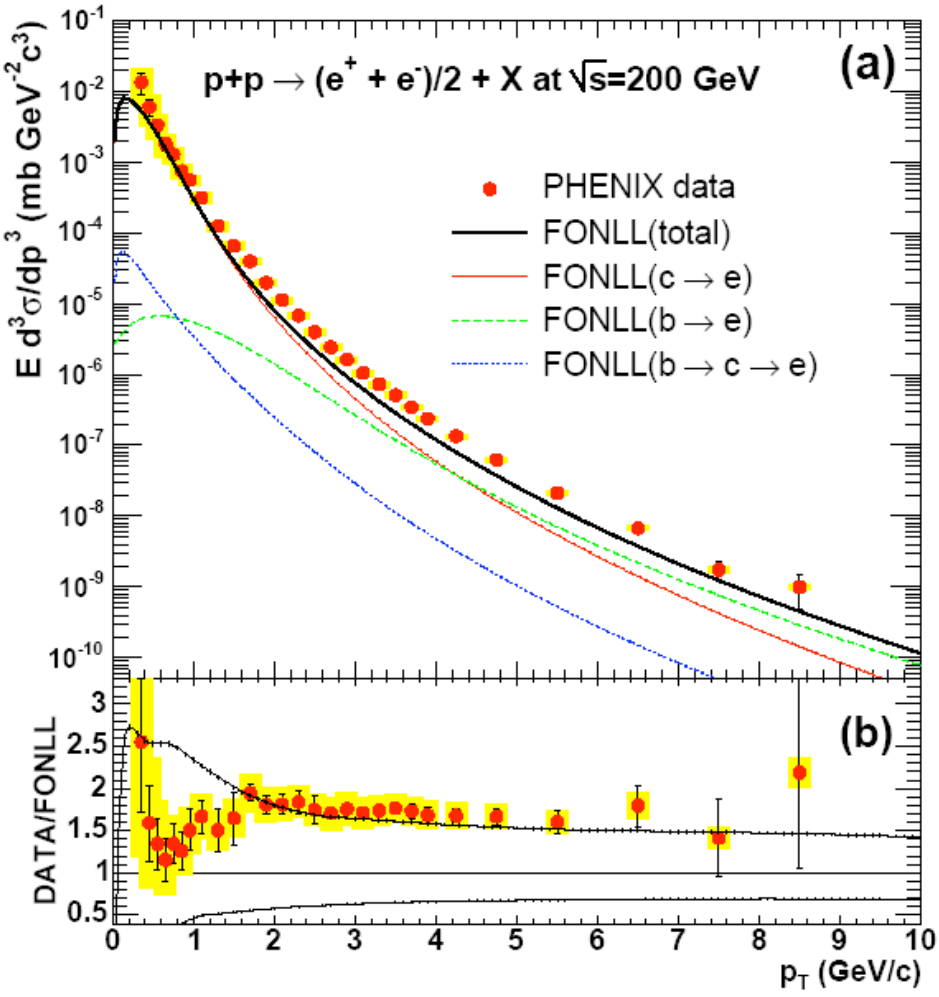


Figure 1.5: Heavy flavor electrons measured in $p+p$ collisions at RHIC [21].

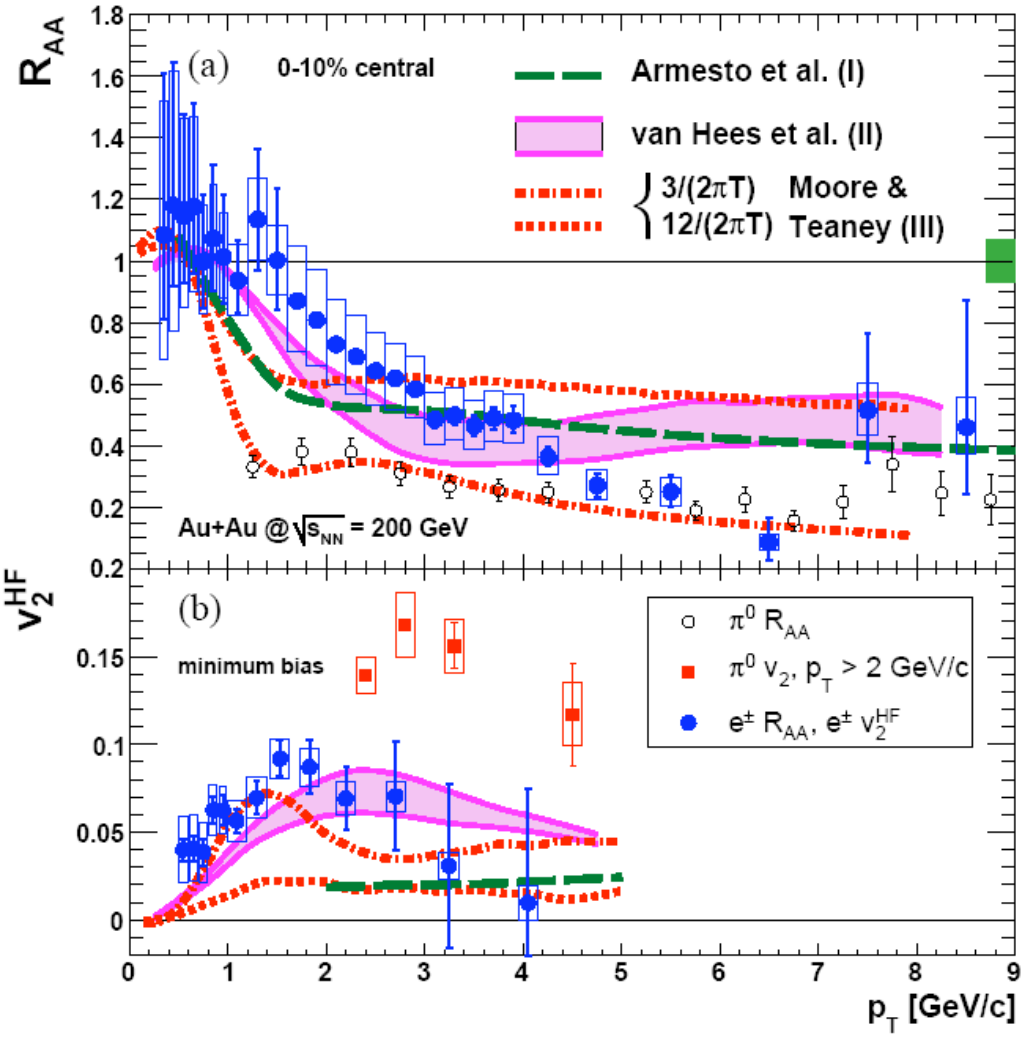


Figure 1.6: The nuclear modification factor $R_{AA}$ and elliptic flow amplitude $v_2$ for heavy flavor electrons and the neutral pion [22].

in $p+p$ collisions at RHIC show that electrons from bottom decays begin to dominate at $p_T \approx 5\text{GeV}/c$ [20], [23], [28]. With this in mind, the $R_{AA}$ data shown in Fig. 1.6 seem to suggest not only that bottom is highly suppressed, but that it is suppressed more than charm. This is, in fact, the exact opposite of expectations from the dead cone effect.

Several theoretical calculations that attempt to simultaneously describe the observed suppression and elliptic flow amplitde $v_2$ are shown in Fig. 1.6. The dashed green curve uses perturbative QCD to calculate radiative energy loss of heavy quarks and lights quarks [24], and matches the measured suppression well at high $p_T$. This model gives a larger suppression at intermediate $p_T$ and fails to accurately describe the heavy flavor electron $v_2$.

Langevin transport models are shown for different values of the heavy quark diffusion coefficient $D_{HQ}$ [25], [26]. The range of $D_{HQ}$ that most accurately matches the data implies the medium has an entropy density to viscosity ratio $\eta/s$ close to the quantum lower bound of $1/4\pi$, obtained with techniques exploiting the AdS/CFT correspondence [27].

An increase in the $\Lambda_c/D$ ratio in heavy ion collisions could also contribute to a suppression of electrons from heavy flavor decays [29]. Measurements at RHIC have shown that the proton to pion ratio increases by nearly a factor of 3 at $p_T = 3$ GeV/c in Au+Au collisions relative to $p+p$ [30]. If this baryon enhancement carries over into the family of charmed baryons, a suppression of electrons from charm could result from the smaller branching ratio of $\Lambda_c \rightarrow e^{\pm} + X$ (4.5 %), relative to the branching ratio $D^{\pm} \rightarrow e^{\pm} + X$ (17.2 %) [19]. However, at this time no measurements of the $\Lambda_c/D$ ratio at RHIC exist to constrain these calculations.

### 1.1.3 Cold Nuclear Matter Effects

Competing effects from different processes that occur in collisions of heavy nuclei are difficult to identify experimentally. Every measurement of particles produced in the collision includes elements from each stage of the evolution of the system. In order to quantitatively study the properties of the QGP, it is necessary to separate effects which are due to interactions with the medium from those which are intrinsic to interactions of cold nuclei. The $p+p$ baseline measurements used to calculate the nuclear modification factor $R_{AA}$ can not account for these nuclear effects, since none are present in free protons. Also, as the $^{197}$Au nucleus contains 118 neutrons, the majority of nucleon-nucleon collisions in a Au+Au event involve neutrons. Any isospin dependent effects can not be modeled with $p+p$ collisions.

Collisions of protons or deuterons with gold nuclei provide a way to experimentally probe the initial state of a nucleus-nucleus collision. The number of

binary nucleon-nucleon collisions in a typical $d$+Au collision is about 8, much smaller than the minimum bias Au+Au value of $N_{coll} \approx 250$. Since the number of nucleon collisions, and therefore the amount of produced particles is low, no hot thermalized system will form in a $d$+Au collision. However, all the nuclear effects present in Au+Au collisions can be probed. Together, these are called cold nuclear matter effects.

### The Nuclear Parton Distribution Function

As heavy quarks are produced via gluon fusion, the total $c$ and $b$ cross section is sensitive to the distribution of gluons inside the nucleus. The European Muon Collaboration [31] and subsequent experiments have mapped out rich structure in the ratio of nucleon structure functions $R^A_{F_2} = F^A_2/F^d_2$ as a function of Bjorken $x$ [32]. The modification in the region where the ratio is less than one is called shadowing (at low $x$) or the "EMC effect" at $0.3 < x < 0.7$, while in the $x-$range with $R^A_{F_2} > 1$ the modification is known as antishadowing (see Fig. 1.7).

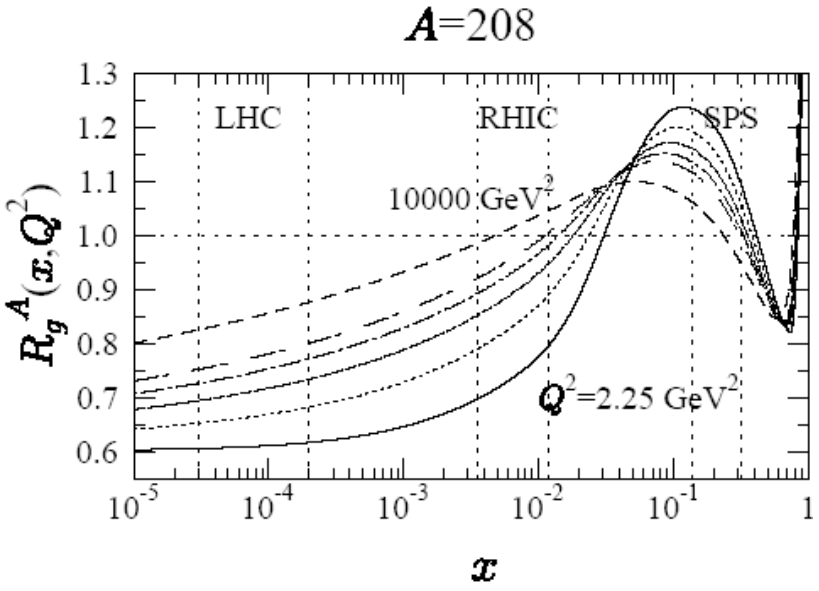


Figure 1.7: The ratio $R^A_g(x, Q^2)$ [33].

As these are purely nuclear effects, they can not be modeled with $p + p$ collisions. Collisions of deuterons with heavy nuclei provide an ideal system for studying these nuclear effects. In Au+Au, such effects will be larger than in

$d$+Au, due to the fact that both participants in the collision will have modified parton distributions.

### Cronin Enhancement

Measurements in $p$+A collisions in the 1970's showed that particle production at moderate transverse momentum increases faster than the number of binary nucleon-nucleon collisions $< N_{coll} >$ [34]. Furthermore, the magnitude of this so-called "Cronin" enhancement is seen to increase with the mass of the particle species. Figure 1.8 shows the nuclear modification factor $R_{dA}$ measured in $d$+Au collisions at $\sqrt{s_{NN}} = 200$ GeV for charged pions, kaons, and protons [35]. Note that the nuclear modification factor for the charged pion is very close to one, while the proton has significant enhancement. Fig. 1.9 shows the $\pi^0$ and $\eta$ meson $R_{dA}$ over a wide range of $p_T$ [41]. Below 10 GeV/$c$, $R_{dA} \sim 1$, indicating little or no cold nuclear matter effects on pions in this momentum range.

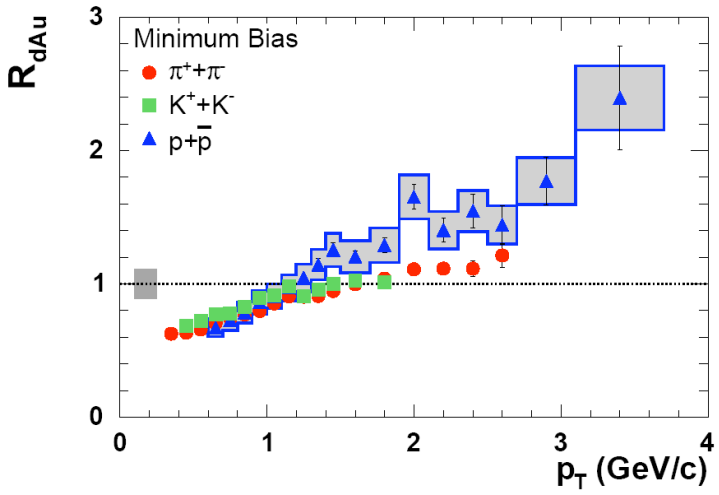


Figure 1.8: The nuclear modification factor $R_{dA}$ for $\pi^{\pm}, K$ and $p$ [35].

The broadening of the proton $p_T$ spectrum is usually attributed to multiple scattering of partons inside the nucleus. The scattering gives the parton a tranverse momentum boost before the interaction that leads to the production of the observed particle. The parton's altered momentum is reflected in the enhanced $p_T$ spectrum of the final state particles.

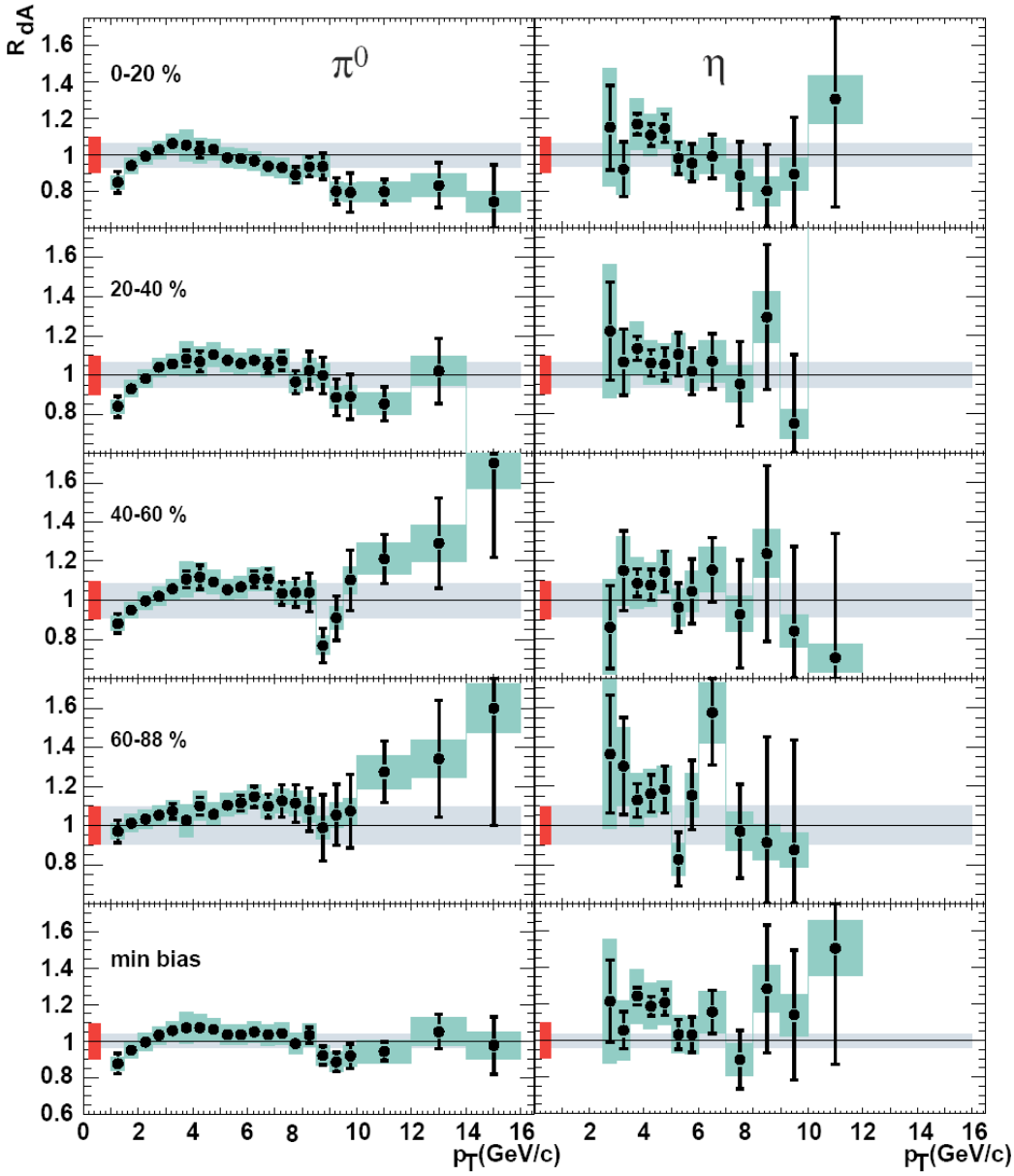


Figure 1.9: The nuclear modification factor $R_{dA}$ for the neutral pion and eta mesons [41].

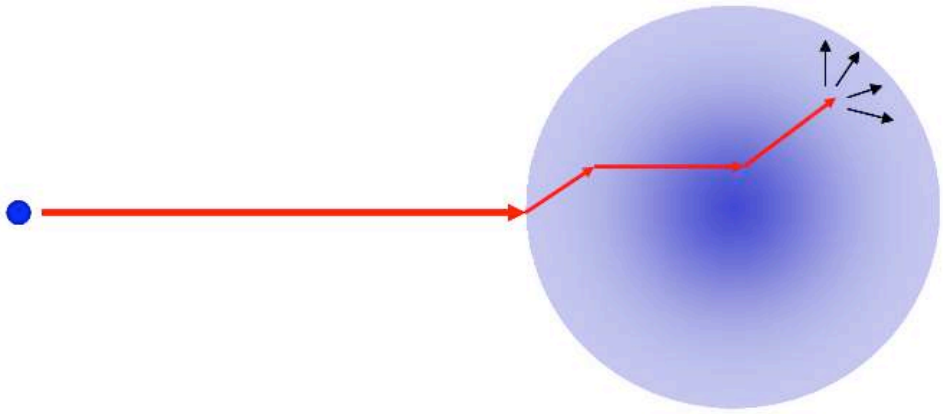

Figure 1.10: Illustration of a qualitative description of Cronin enhancement. The parton undergoes multiple scatterings in the nucleus, resulting in a transverse momentum boost, before the interaction that ultimately produces the final state particle.

### CNM Effects on the $J/\psi$

Although $J/\Psi$ suppression was predicted as an "unambiguous" signal of deconfinement in a quark gluon plasma [12], a significant suppression is seen in $d$+Au collisions [36]. The increase of suppression at forward rapidity observed in Au+Au collisions is also seen in d+Au, which suggests that this difference is not due to the presence of the hot medium, but rather is a consequence of intrinsic nuclear effects. This measurement clearly shows the importance of cold nuclear matter effects when considering heavy ion collisions. It is worth noting, however, that the suppression observed in Au+Au collisions exceeds extrapolations of CNM effects in the Au+Au collision system [39], which indicates that there is indeed additional $J/\psi$ suppression in the QGP.

Fig. 1.11 shows the $J/\psi$ nuclear modification factors $R_{dA}$ and $R_{cp}$ as a function of rapidity. The green line is a calculation based on gluon saturation in the nucleus that predicts a slight enhancement at midrapidity, which is not observed, but agrees well with the suppression at forward rapidity [37]. The red curves represent calculations based on parametrizations of the EPS09 modified nuclear PDF with a $J/\psi$ break-up cross section of $\sigma_{br} = 4$ mb [38]. These calculations significantly underestimate the suppression observed in central events compared to peripheral events at forward rapidity.

It is not immediately clear whether $J/\Psi$ suppression in $d$+Au is a consequence of a suppressed charm production mechanism or break-up of pairs in

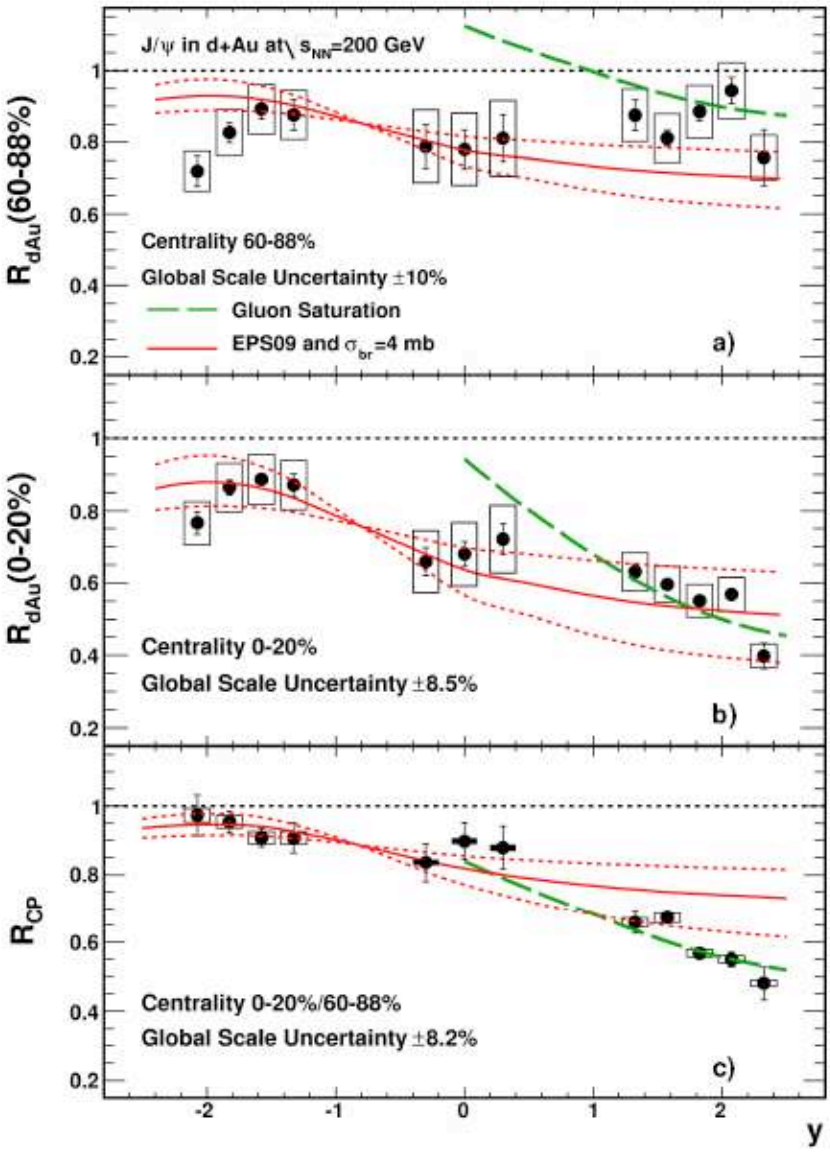


Figure 1.11: $J/\Psi$ suppression measured in $d$+Au collisions as a function of rapidity [36].

the cold nuclear medium. Information on the $p_T-$dependence of $J/\psi$ suppression in $d$+Au is of great interest, but no results exist at RHIC energies at this time.

### CNM Effects on Open Heavy Flavor

The measurement of electrons from the decays of $D$ and $B$ mesons in $d$+Au collisions at RHIC is the focus of this thesis. The apparent contrast between mass-ordered Cronin enhancement of light-flavor hadrons and suppression of the $J/\psi$ meson in cold nuclear matter can be addressed by measurements of open heavy flavor mesons produced in $d$+Au collisions, which have the same primordial production mechanism as the $J/\psi$ but are not subject to any break-up effects in the cold nuclear medium. The strong suppression of electrons from heavy flavor in Au+Au collisions is usually attributed to heavy quark energy loss in the medium, but the lack of a definitive measurement of CNM effects on open heavy flavor complicates the interpretation.

A model based on gluon saturation in the nucleus predicts an enhancement of open charm at midrapidity at RHIC energies [40]. Fig. 1.13 shows a prediction for the nuclear modification factor of mesons containing open charm for several rapidity ranges at RHIC and LHC energies. Of interest here is the $y = 0$ curve at RHIC. A modest enhancement for charm and a scaling with $N_{coll}$ for bottom is expected. Note that these curves represent the nuclear modification factors for the mesons themselves, while the measurements at RHIC are of electrons from the meson decays. Similar models also predict an enhancement of $J/\psi$ in $d$+Au collisions, which are not observed.

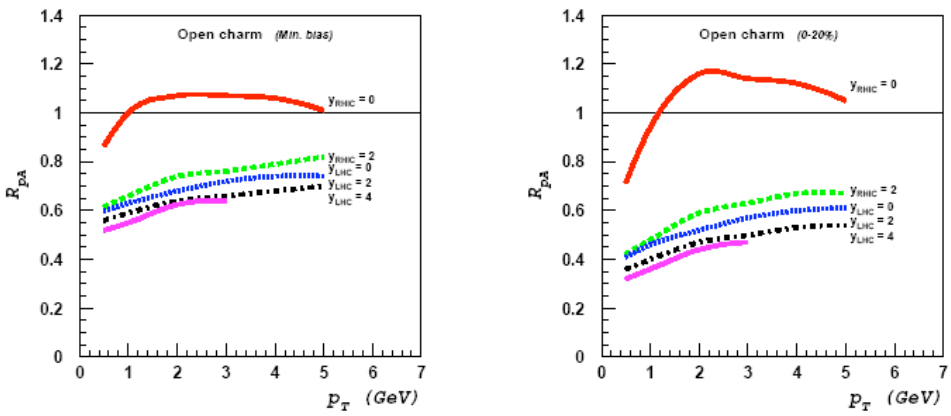


Figure 1.12: Prediction of open charm $R_{pA}$ from [40].

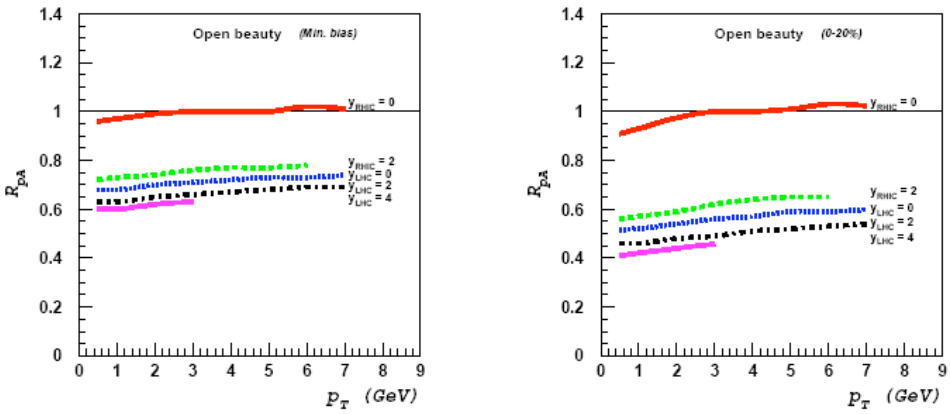


Figure 1.13: Prediction of open bottom $R_{pA}$ from [40].

# Chapter 2

# Experimental Apparatus

This chapter describes the accelerator and experimental apparatus used in the preparation of this manuscript. Although the PHENIX spectrometer is capable of making measurements of a large set of particle species, special focus is given to the detectors used to make electron measurements.

## 2.1 The Relativistic Heavy Ion Collider

Located at Brookhaven National Laboratory (BNL) in Upton, NY, the Relativistic Heavy Ion Collider (RHIC) is the largest heavy ion accelerator in North America. It is currently the only accelerator in the world capable of colliding beams of polarized protons. The versatility of the machine allows studies of nuclear matter at extremes over a wide range of system sizes and energy densities (see Tab 2.1). The upcoming Electron Beam Ion Source (EBIS) preinjector upgrade will be able to produce 2 MeV/u beams of any ion at the preinjector, further extending the flexibility of the accelerator [46].

| Beam Species | $\sqrt{s_{NN}}$ (GeV) |
|---|---|
| $p+p$ | 200, 500 |
| $d$+Au | 200 |
| Cu+Cu | 22, 64, 200 |
| Au+Au | 7.7, 9, 11, 19, 22, 39, 62, 130, 200 |

Table 2.1: Beam species and center of mass energies that are available at RHIC.

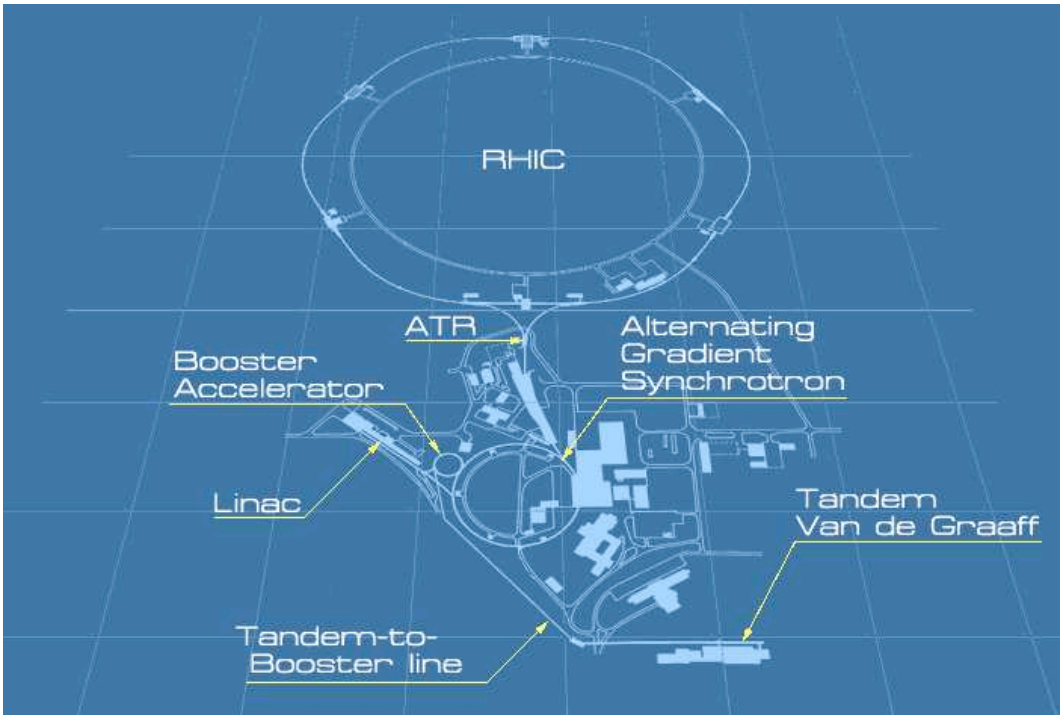


Figure 2.1: Schematic of the Relativistic Heavy Ion Collider complex.

## 2.2 The PHENIX Experiment

The Pioneering High Energy Nuclear Interaction eXperiment (PHENIX) detector consists of two central spectrometer arms covering the mid-rapidity region ($|\eta| < 0.35$) and two specialized muon detectors covering forward and backward rapidity ($1.2 < |\eta| < 2.4$). The various subsystems of the detector allow measurements from probes sensitive to all timescales of the interaction and enable a robust and diverse physics program.

### 2.2.1 Global Detectors

The PHENIX global detectectors are used to trigger the data acquisition system and characterize each event. These systems allow precise determination of the event $z$-vertex (which in turn allows precise track reconstruction and momentum determination), provide the START time for time-of-flight measurements, and are used to determine event centrality in heavy ion collisions (see section 2.2.1).

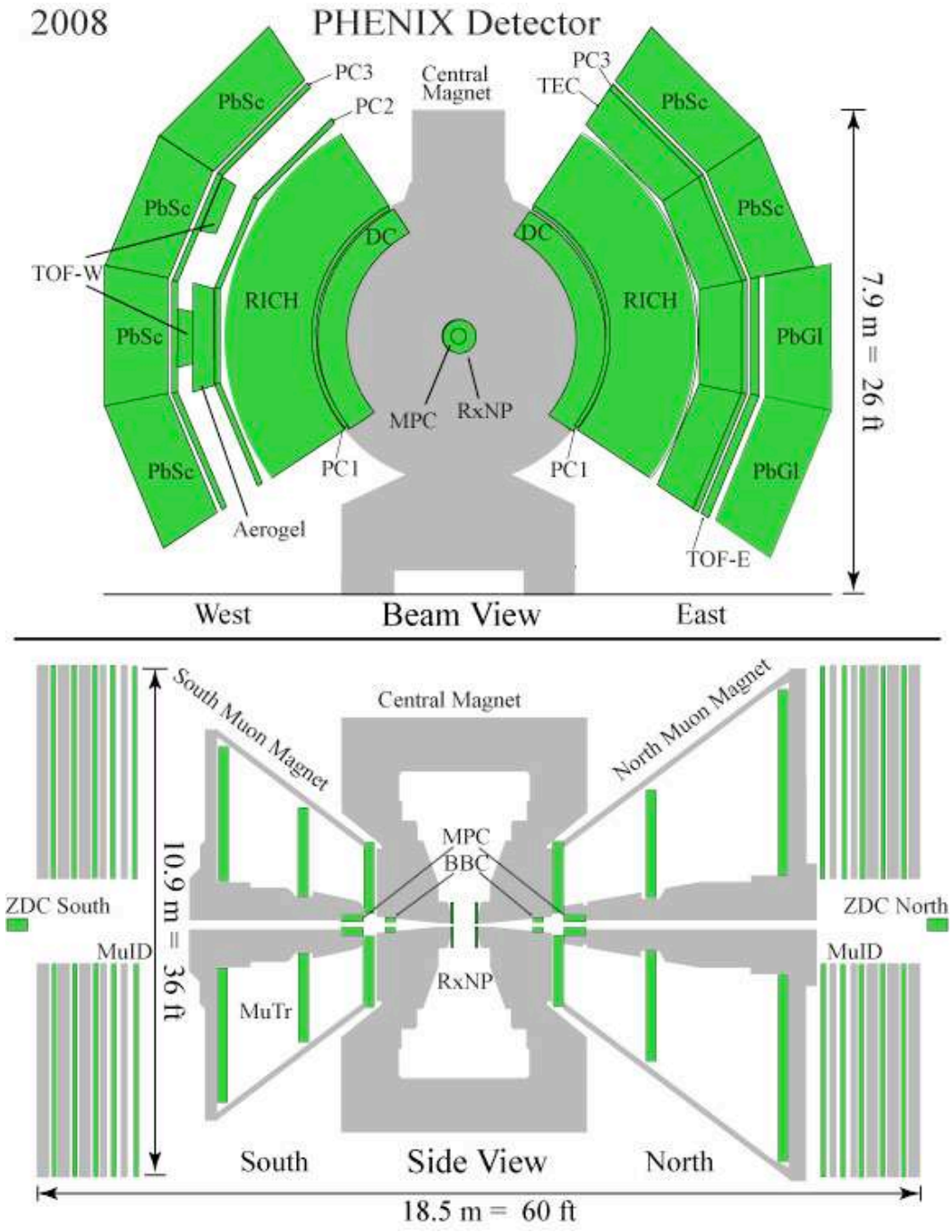


Figure 2.2: Schematic of the PHENIX detector configuration during the 2008 $d$+Au Run.

### Beam-Beam Counters

The PHENIX Experiment has a pair of beam-beam counters (BBCs) positioned 144 cm up and down the beam pipe from the center of the interaction diamond. This location places several strict requirements on the detector. First, the device must be able to withstand the high radiation environment near the interaction point. Second, the device must be able to function in the 3 kG magnetic field the PHENIX central magnets produce at this point. Finally, due to the versatility of the accelerator, the detector must provide a meaningful response in $p+p$ collisions (which will have at most a few particles in the BBC acceptance) and Au+Au (which can produce hundreds of particles in the BBC acceptance).

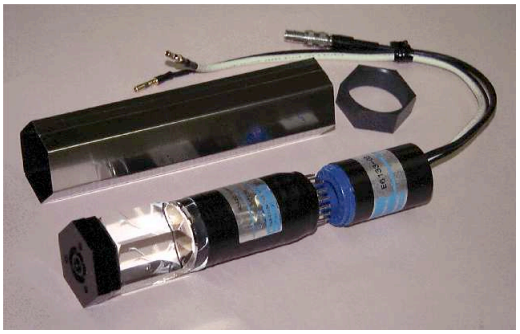

Figure 2.3: A single element of the PHENIX BBC [48].

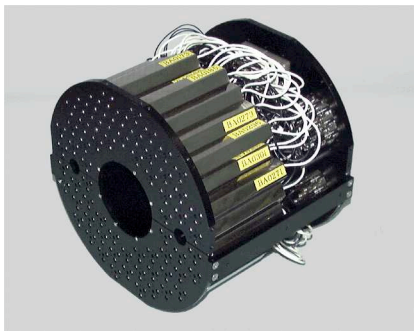

Figure 2.4: The assembled PHENIX BBC array.

The realization of the BBC is a Cherenkov counter, read out by photomultiplier tubes. The radiator is a 3 cm long block of quartz which also functions as the window to the PMT to maximize light transmission into the tube. The PMT uses fine mesh type dynodes, which are specially designed to function in a magnetic field. The measured timing resolution of a single BBC element is $52 \pm 4$ ps (rms) [49]. A completed BBC array consists of 64 individual PMTs, and covers the rapidity range $3.0 < |\eta| < 3.9$ over full azimuth.

Each BBC element that recieves a hit in a given collision measures an arrival time of the particles from the collision point. The time reported by the north and south BBC arrays($T_N$ and $T_S$) is the average of the times from each individual element in that array. Since the bunch length at RHIC is 25 cm RMS, the event vertex can be spread over a range of about 2 ns in time. The $z$ position (along the beam axis) of the collision is determined from the difference between the arrival times at each BBC:

$$z = \frac{c}{2}\{T_N - T_S\} \tag{2.1}$$

With the above timing resolution, the $z-$vertex resolution from the BBCs is about 1 cm.

The BBC also serves as the minimum bias trigger during heavy ion runs at PHENIX. For Au+Au collisions, the trigger condition is that at least one PMT in the north and south BBC arrays receive a hit. During the 2008 RHIC $d$+Au run, the Au beam moved in the north-to-south direction at the PHENIX interaction region. The PHENIX Minimum Bias trigger condition was that at least one PMT fired in the South BBC array.

### Zero Degree Calorimeters

In collisions of two Au nuclei at $\sqrt{s_{NN}} = 200\text{GeV/c}$, evaporation neutrons from the interaction diverge less than 2 milliradians from the beam axis. Two Zero Degree Calorimeters (ZDCs) were installed 18m from the interaction point to measure these neutrons. Since these small hadronic calorimeters are located behind accelerator dipole magnets, charged particles are bent away and only neutral particles are measured (see Fig. 2.5).

Each ZDC module consists of tungsten plates (total thickness = 2 hadronic interaction lengths) to absorb incoming neutron energy. Particles produced in the absorber plates radiate Cherenkov light in PMMA fibers between plates, which is then detected by photomultiplier tubes. Additional fibers feed light from an LED into the PMT for gain monitoring. A total of three modules (6 interaction lengths) make up each complete ZDC.

In addition to triggering and centrality determination, the ZDC can also tag the spectator neutron from the deuteron in peripheral $d$+Au collisions. This can be used to study isospin effects on particle production (see [50] for more information).

### Centrality Determination

For Au+Au collisions, the event centrality is determined by comparing the ZDC and BBC response. Since the ZDC primarily measures spectator neutrons, and the BBC measures particles produced in the collision, peripheral collisions will have a relatively high ZDC response and low BBC response, while central collisions will have the opposite. Fig. 2.7 shows a comparison of the energy measured in the BBC and ZDC, normalized by the maximum energy $E^{MAX}$ each detector receives. The 0-5% centrality bin in the figure represents the 5% of total events that produce the highest BBC response (i.e. most produced particles) and the lowest ZDC response (the least spectators). These centrality categories are then related to the number of nucleon-nucleon collisions ($N_{coll}$) and the number of participating nucleons ($N_{part}$) by a Monte

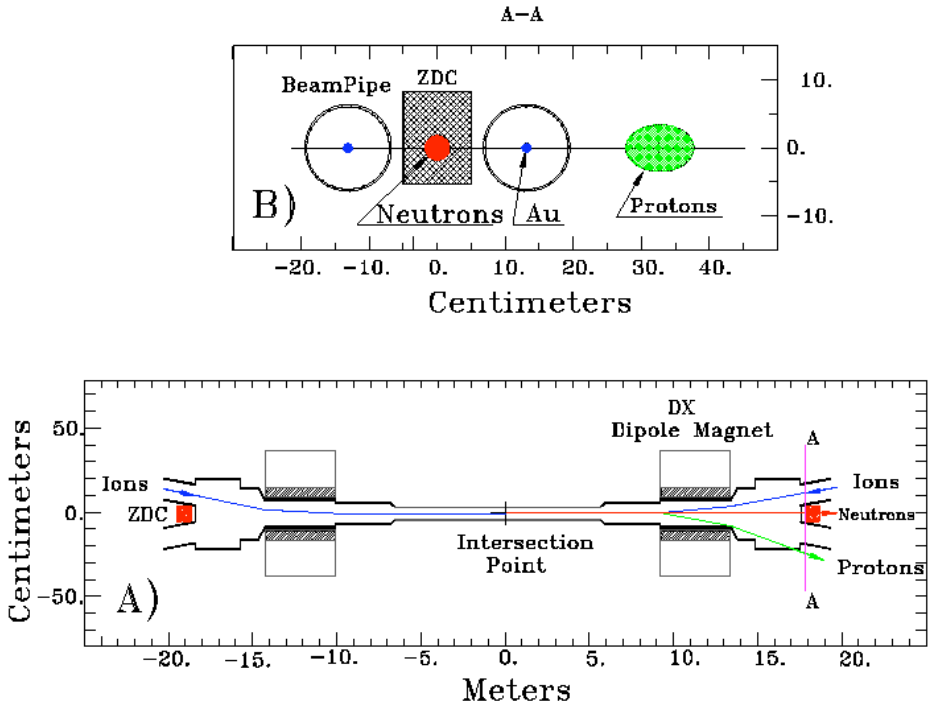


Figure 2.5: Schematic of the ZDC acceptance. Remaining Au ions and charged particles are swept away from the ZDC by dipole magnets, but neutrons continue into the detector [47].

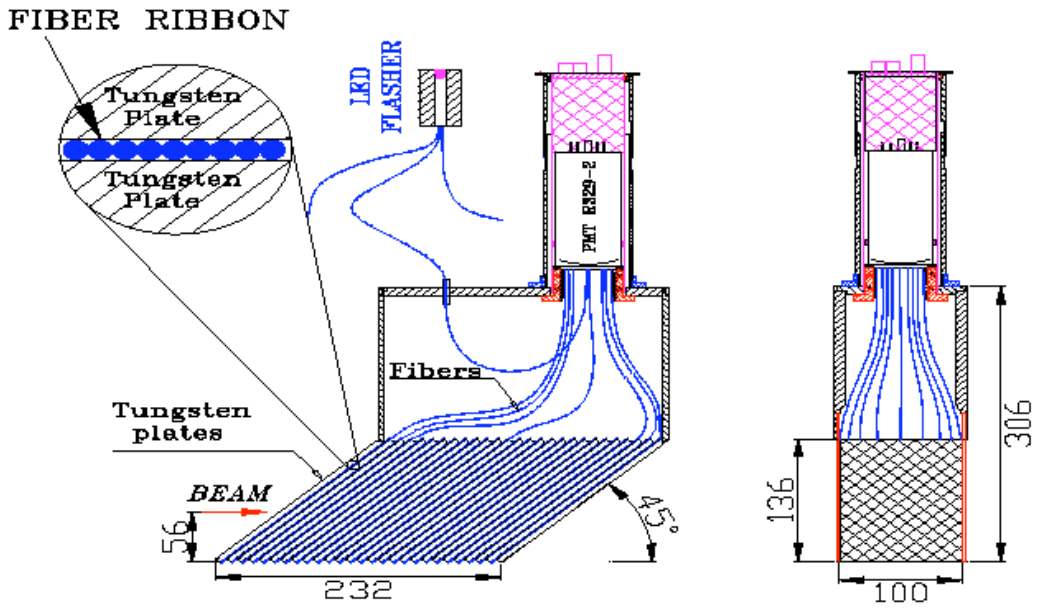


Figure 2.6: Schematic of a single ZDC module. Dimensions are given in mm [47].

Carlo calculation with a simulated BBC and ZDC response and a Glauber model of the colliding nuclei.

In $d$+Au collisions, since the average $N_{coll}$ and event multiplicity are so much smaller than in Au+Au, only the response of the BBC South array (which faces the incoming Au nuclei) is used to calculate centrality (see Fig. 2.8). The relatively large deuteron wave function causes significant overlap between the different centrality classes, as illustrated in Fig. 2.9. The average value of $N_{coll}$ for each centrality is given in Tab. 2.2.

| Centrality | $< N_{coll} >$ |
|---|---|
| 0-100% | 7.6± 0.4 |
| 0-20% | 15.1 ± 1.0 |
| 20-40% | 10.2 ± 0.7 |
| 40-60% | 6.6 ± 0.4 |
| 60-88% | 3.2 ± 0.2 |

Table 2.2: Average values of $N_{coll}$ for the five $d$+Au centrality categories.

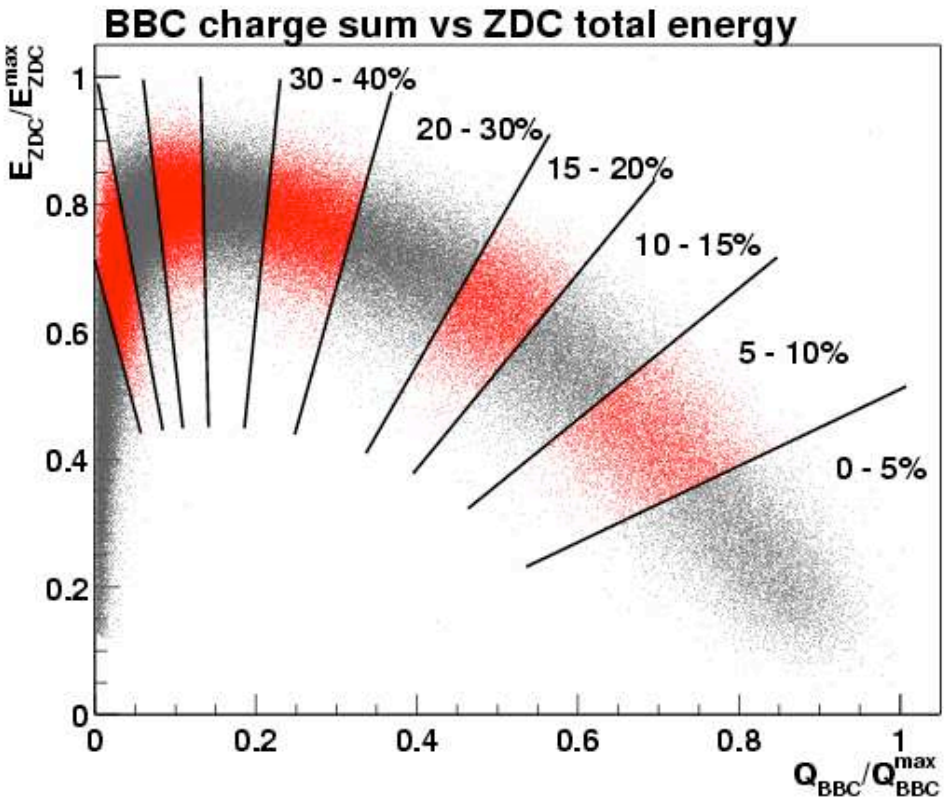


Figure 2.7: Centrality categories in Au+Au collisions are determined by comparing BBC and ZDC response. In the most central bin (0-5%), the charge deposited in the BBC is high, while the energy deposited in the ZDC from spectator neutrons is relatively low.

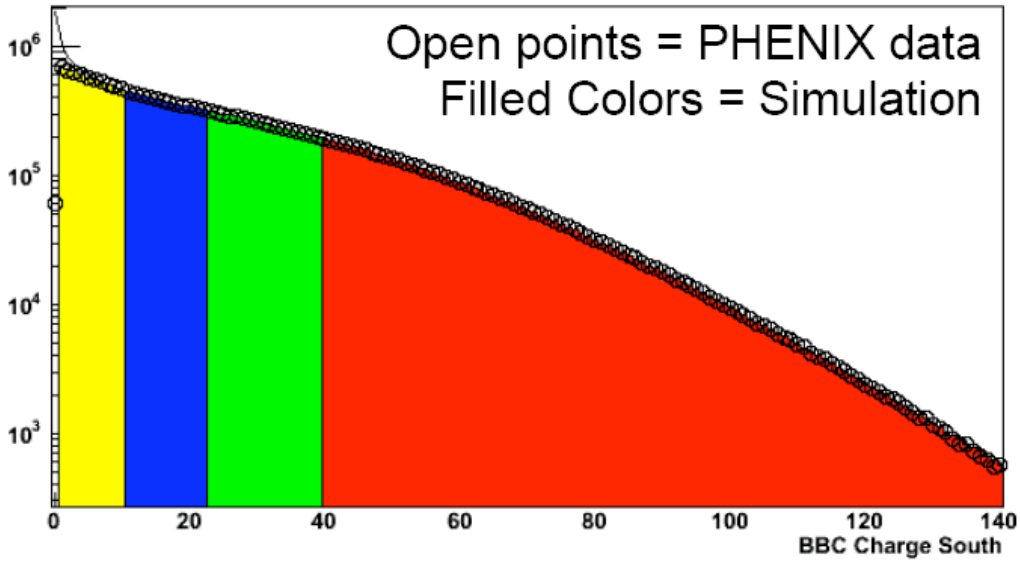


Figure 2.8: The BBC South array response in $d$+Au collisions, compared to simulation. Different colors represent the different centrality categories.

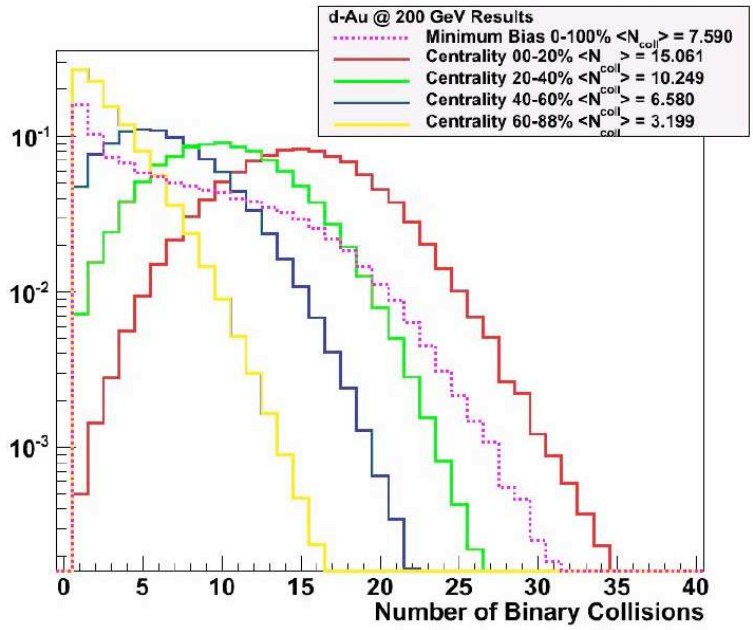


Figure 2.9: Distribution of $N_{coll}$ for the various centrality categories in $d$+Au.

### 2.2.2 Magnets

Measurements of the bend radius of charged particle tracks in the PHENIX magnetic field allows determination of the particles momentum. PHENIX has three magnet systems, central magnets and muon magnets, that provide this field. Each magnet provides a field integral of about 0.8 T·m, with field lines that are parallel to the beam in the central arm and perpendicular to the beam in the muon arms(see Fig. 2.11) [51].

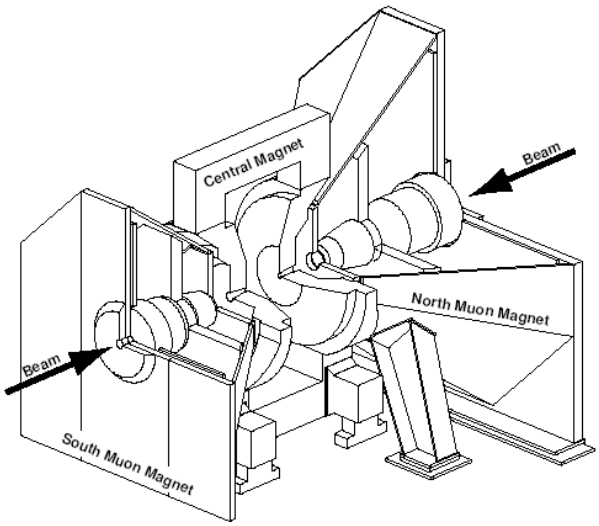


Figure 2.10: Cut-away view of the PHENIX magnets.

The central magnets were designed to have no material in the central arm aperture, but function as hadron absorbers for the muon arms. The poles of the central magnet contain two coils, which may be operated in "'++"' mode, where the magnetic fields add, or in "'+-"' mode, where the field within R¡50 cm largely cancels to enable operation of specific upgrades (for example, the Hadron Blind Detector). The field in central arms decreases quickly for R¿200 cm to avoid smearing Cherenkov rings generated by electrons in the RICH and avoid disrupting the RICH and EMcal phototubes. The fringe field past 200 cm will bend charged particles at most 5% past the original bend angle, which allows the tracking algorithm to assume all tracks are straight once they enter the drift chamber [55].

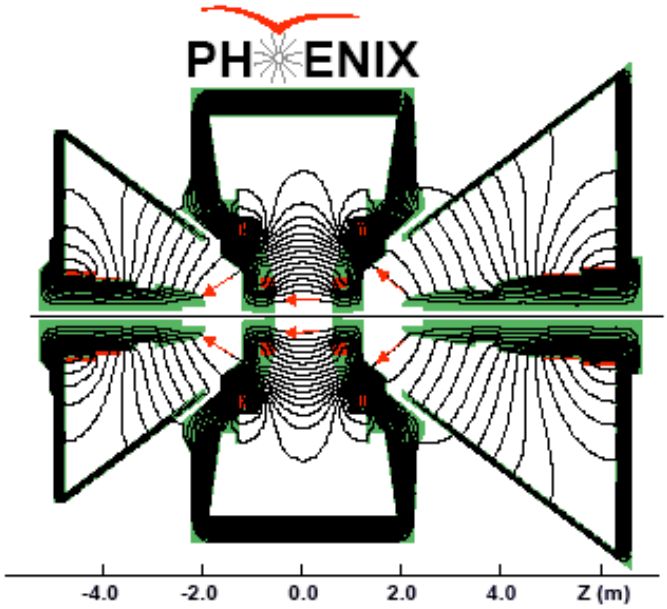


Figure 2.11: Schematic of the PHENIX magnetic field in the "++" configuration.

### 2.2.3 Central Arm Detectors

The PHENIX central arm detectors were specifically designed to measure electrons and photons. The following sections describing the various subsystems are organized in roughly the same order that an electron produced in an event would encounter them; that is, from inner to outer.

#### Drift Chamber

The first detector subsystem that electrons from the collision vertex encountered in Run-8 was the drift chamber. This multiwire chamber operates in a 50/50 mixture of argon and ethane at atmospheric pressure, which is bubbled through liquid ethanol. Ionization left by charged particles in the gas is drifted towards wires inside the gas volume and avalanched. This charge is read out at the end of each wire and registers as a hit.

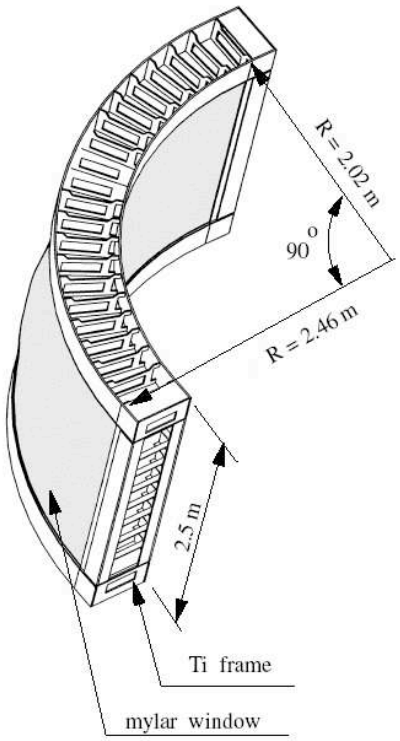


Figure 2.12: The frame of one arm of the PHENIX drift chamber [52].

Each arm of the drift chamber extends radially from 200 to 240 cm away from the interaction point. The arms cover 2 meters along the beam direction,

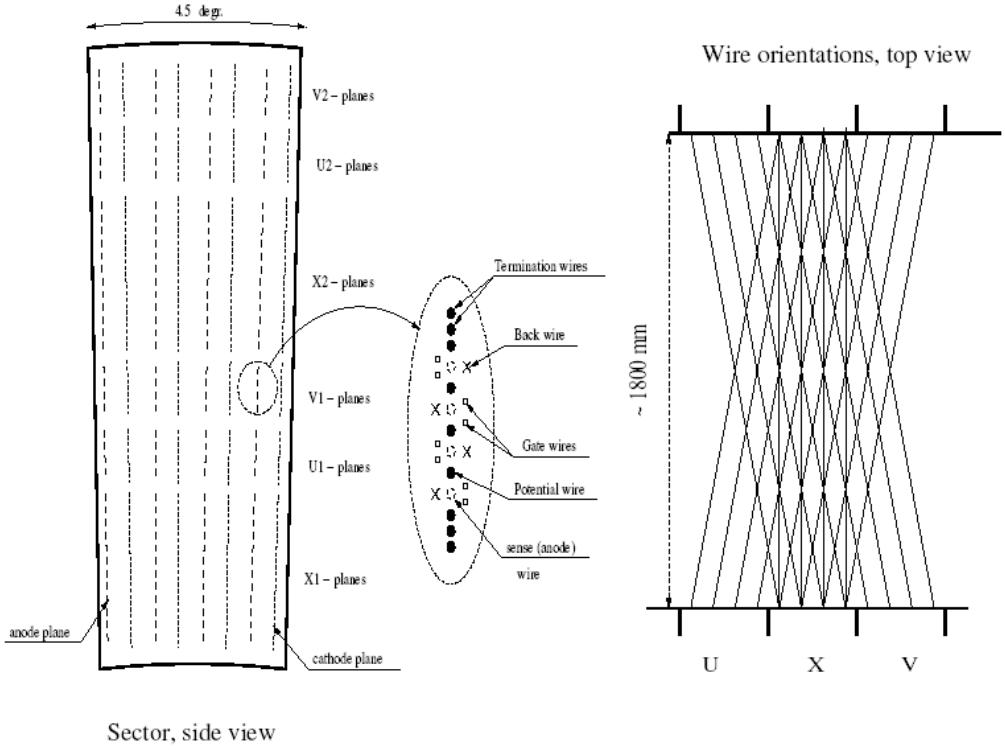


Figure 2.13: Schematic of the drift chamber wire layout [52].

corresponding to a pseudorapidity coverage of $\eta < 0.35$. The angular extent of each arm is $\pi/2$ in azimuth, with the East arm covering $\frac{11}{16}\pi < \phi < \frac{19}{16}\pi$ and the West arm covering $-\frac{3}{16}\pi < \phi < \frac{5}{16}\pi$. The arms are divided into 20 identical sectors.

Each DC sector houses 6 wire modules (see Fig. 2.13). The X1 and X2 wires run parallel to the beam to give measurements in the $r - \phi$ plane. The U1, U2, V1 and V2 wires are positioned behind the X wires, and are tilted at at stereo angle of about 6° allow allow determination of the $z-$coordinate.

### Pad Chambers

Similar to the drift chambers, the pad chambers (PCs) are multiwire proportional counters operating in a 50/50 argon/ethane mixture. Each pad chamber module contains one layer of wires in between a solid copper cathode and a pixelated cathode. Ionization left by charged particles is avalanched onto the

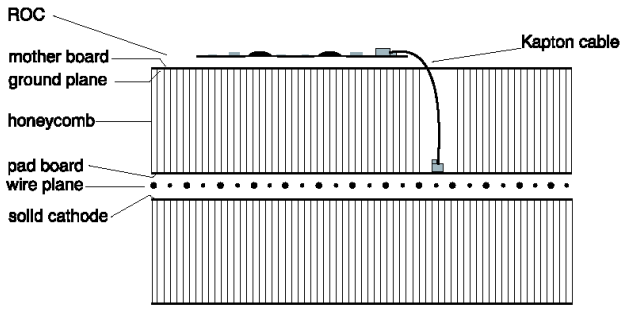


Figure 2.14: A cut away view of the PHENIX pad chamber. The FR4 honeycomb construction provides a rigid body with minimal material in the aperture.

wires, and the image charge induced on the pixelated cathode is read out to give a space point along the straight trajectory of the particle.

There are three distinct layers of pad chambers in PHENIX, known as PC1, PC2, and PC3 from inner to outer. The innermost pad chamber is directly behind the drift chamber. The PC1 measures the $z-$coordinate of tracks as they exit the drift chamber, which allows determination of the total momentum vector $\vec{p}$. The second layer is only present in the West spectrometer arm, directly behind the RICH. The third layer, in both arms, is located directly in fromt of the EMCal, and helps resolve abiguities that can arise when reconstructing tracks with the other susbsytems, which is especially important for removing partial tracks from conversions generated in the material of the tracking detectors themselves.

The momentum resolution of the PHENIX central arm tracking detectors is

$$\frac{\delta p}{p} = 0.7\% \oplus 1\% p/(GeV/c). \tag{2.2}$$

### Ring Imaging Cherenkov Counter

The primary electron ID device in PHENIX is the Ring Imaging Cherenkov Counter (RICH). Each of the two PHENIX central arms house one RICH detector, which extends from 2.575 to 4.1 m radially. The radiator is a volume of $CO_2$ at atmospheric pressure, with a length that varies from 0.9 m at $\theta = 90°$ to 1.5 m at $\theta = 70°$ and 110°. Relativistic electrons generate Cherenkov light in the gas, which is reflected by thin mirrors onto arrays of phototubes. Charged pions with $p_T$ below 4.9 GeV/$c$ do not radiate, so the RICH allows very clean electron/pion separation in this momentum range.

Fig. 2.16 shows a side view of the RICH. The spherical mirror arrays reflect

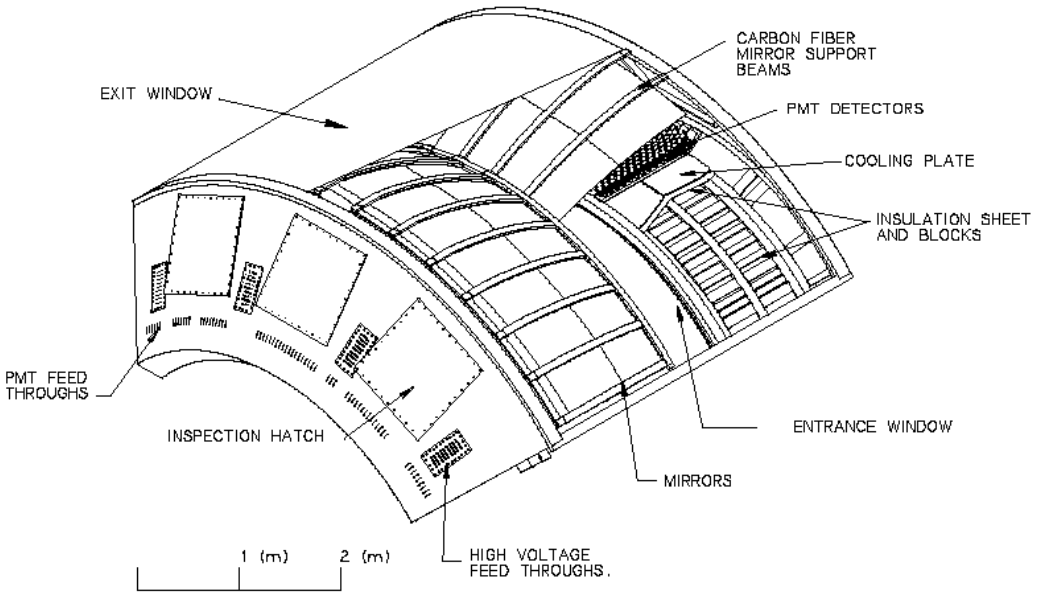


Figure 2.15: Cutaway view of one arm of the PHENIX RICH [53].

Cherenkov photons onto 16 $\times$ 80 arrays of phototubes, which are positioned behind the PHENIX central magnet to shield the PMTs from primary particles produced in the collision. Each phototube is enclosed in either mu-metal or ferroperm magnetic shielding, and is attached to a Winston cone with a 50 mm entrance diameter to maximize Cherenkov photon collection. The angular segmentation of the PMT arrays is about $1^\circ \times 1^\circ$ in $\theta$ and $\phi$.

### Electromagnetic Calorimeters

The electromagnetic calorimeters (EMCal) form the outermost layer of the PHENIX Central Arm spectrometers. Eight different sectors (four per arm) comprise the complete EMcal, 6 of which use lead scintillator technolgy, and 2 which use lead glass. The lead scintillator is a shashlik type sampling calorimeter, while the lead glass is a Cherenkov counter. Comparisons of measurements made with the two separate technologies give PHENIX a rigorous standard of quality control [56].

Each lead scintillator tower consists of 66 layers of alternating tiles of lead and scintillator, which add up to a total depth of 18 radiation lengths. Electrons and photons produce electromagnetic showers in the lead, which in turn produces light in the scintillator material. Thirty six wavelength shifting fibers

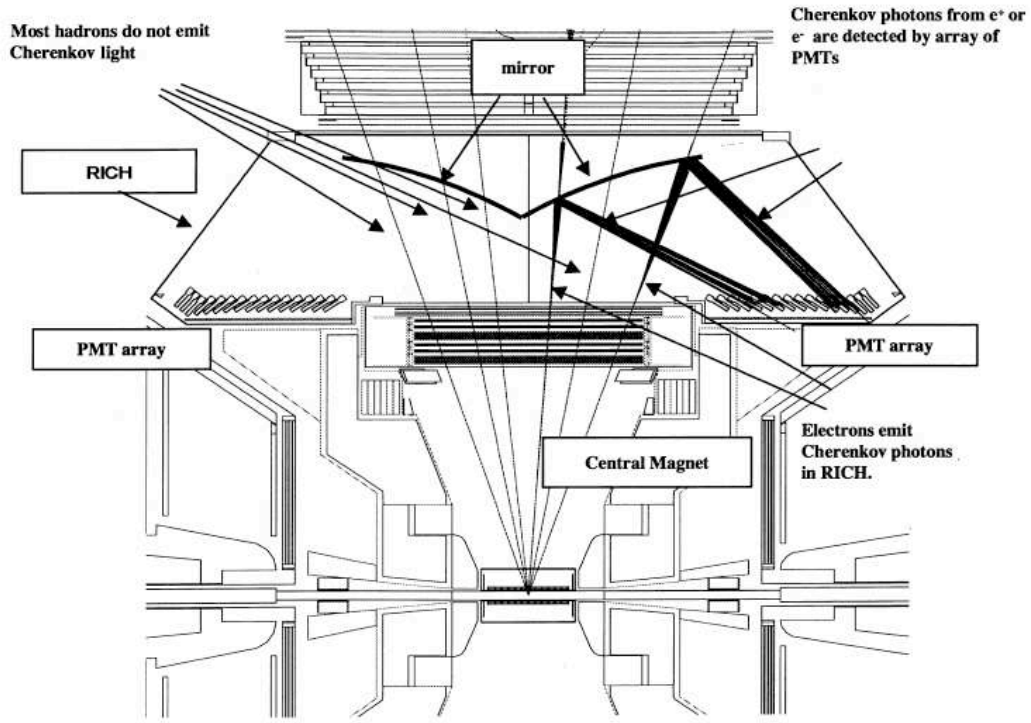


Figure 2.16: The PHENIX RICH detector [54]

run longitudinally through each tower and collect this light, which is then read out by photomultiplier tubes (see Fig. 2.17). For gain monitoring and calibration, an additional "leaky" fiber is inserted into each module. The leaky fiber delivers UV light from a YAG laser and simulates the energy deposited by a 1 GeV/c photon. The energy resolution for this section of the EMcal is

$$\frac{\sigma_E}{E} = \frac{8.1\%}{\sqrt{E}(GeV)} \oplus 2.1\% \ . \tag{2.3}$$

The face of each tower is 5.535 × 5.535 cm, and four individual towers are grouped together mechanically into a module. Groups of 36 modules form a supermodule, and eighteen supermodules form a sector, for a total of 15552 individual towers. The segmentation of the lead scintillator allows the separation of photons from the decay $\pi^0 \to \gamma\gamma$ out to a pion $p_T$ of 12 GeV/$c$.

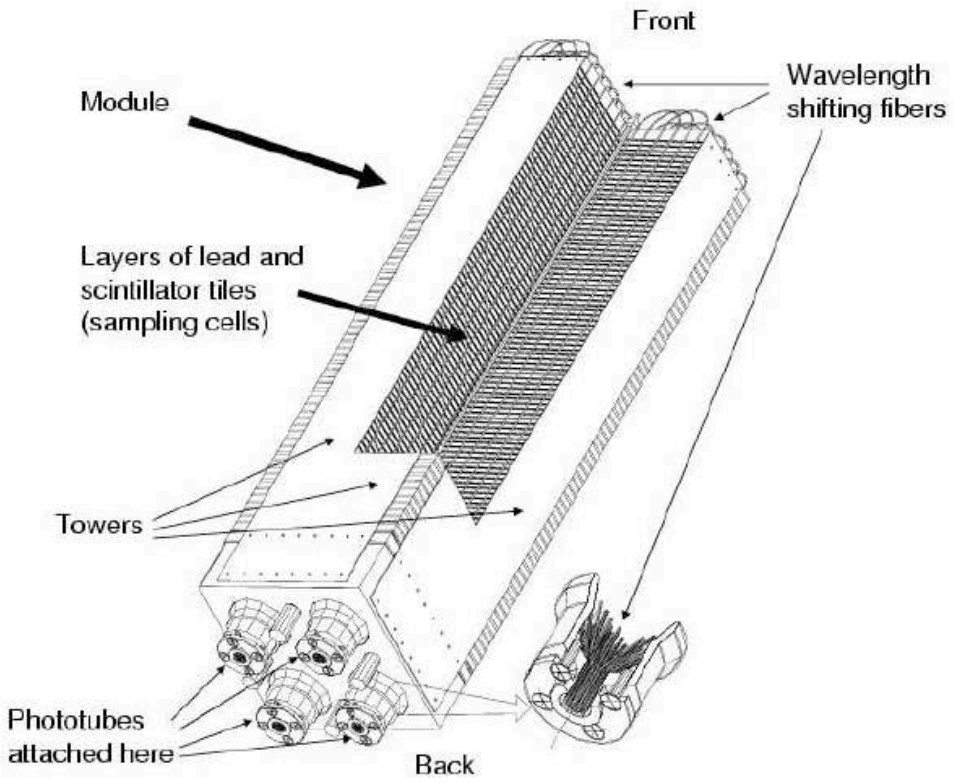


Figure 2.17: Interior view of a single lead scintillator tower [56].

The lead glass EMcal makes up the two lower sectors of the East spectrom-

eter arm. The name refers to the specialized glass in each tower that contains lead, which gives it a relatively high density and small Moliere radius while leaving it transparent to Cherenkov photons. Charged particles generated in electromagnetic showers from photons and leptons radiate UV photons in the glass, which are collected in PMTs mounted on the end of the glass towers. The energy deposited in the shower is directly proportional to the number of photons generated in the tower. Each tower is 14.4 radiation lengths deep with a face size of 40 × 40 mm. The finer segmentation of the lead glass array prevents pion decay photons from merging up to a pion $p_T$ of 16 GeV/$c$.

The lead glass towers are arrayed in 4 × 6 tower supermodules (see Fig. 2.18). For gain monitoring and calibration, each supermodule has 3 LED lights that be used to pulse the towers. The photodiode mounted on the front of the supermodule gives an absolute normalization of the amount of light produced by each LED. Arrays of 16 × 12 supermodules form a sector, and two lead glass sectors gives a total of 9216 individual towers. The energy resolution of the lead glass EMcal sectors is

$$\frac{\sigma_E}{E} = \frac{6\%}{\sqrt{E}(GeV)} \oplus 0.8\% \ . \tag{2.4}$$

## 2.3 Upgrades

As the physics program at RHIC matured, a series of detector upgrades were implemened with specific physics goals in mind. Below is a brief description of two such upgrades that complement the measurement described in this thesis.

### The Hadron Blind Detector

The overwhelming majority of background electrons at PHENIX come from the neutral pion Dalitz decay, $\pi^0 \rightarrow \gamma e^+ e^-$. The combinatorial background from these electrons introduces severe limitations on dielectron measurements at PHENIX. The electron pair produced in this decay has a small opening angle in the lab frame, while electrons from the decays of heavier mesons (such as the $J/\psi$) generally have a wider opening angle. Therefore a detector that can identify close electron pairs (the background pair) from open pairs (which may be a signal) can veto a large amount of the electron background.

The Hadron Blind Detector (HBD) is a windowless, unfocused Cherenkov counter that uses $CF_4$ as both the radiator and detector avalanche gas [57]. Triple stacks of gas electron multipliers (GEMs) amplify photoelectrons produced by Cherenkov light in a CsI photocathode deposited on the upper surface

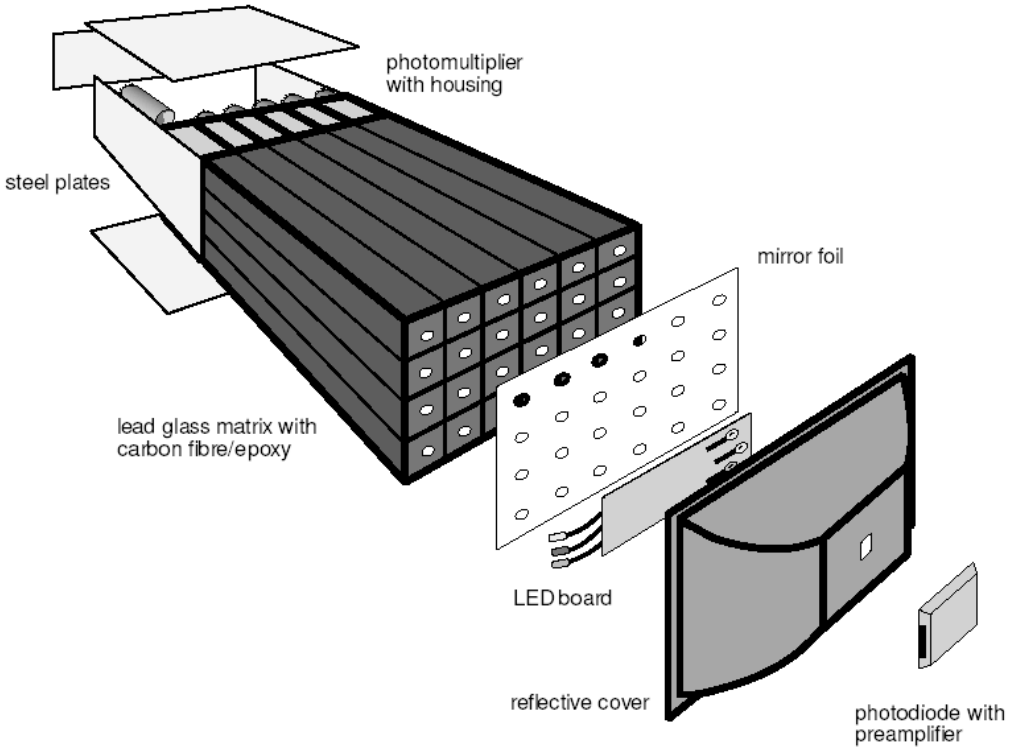


Figure 2.18: Exploded view of a lead glass supermodule [56].

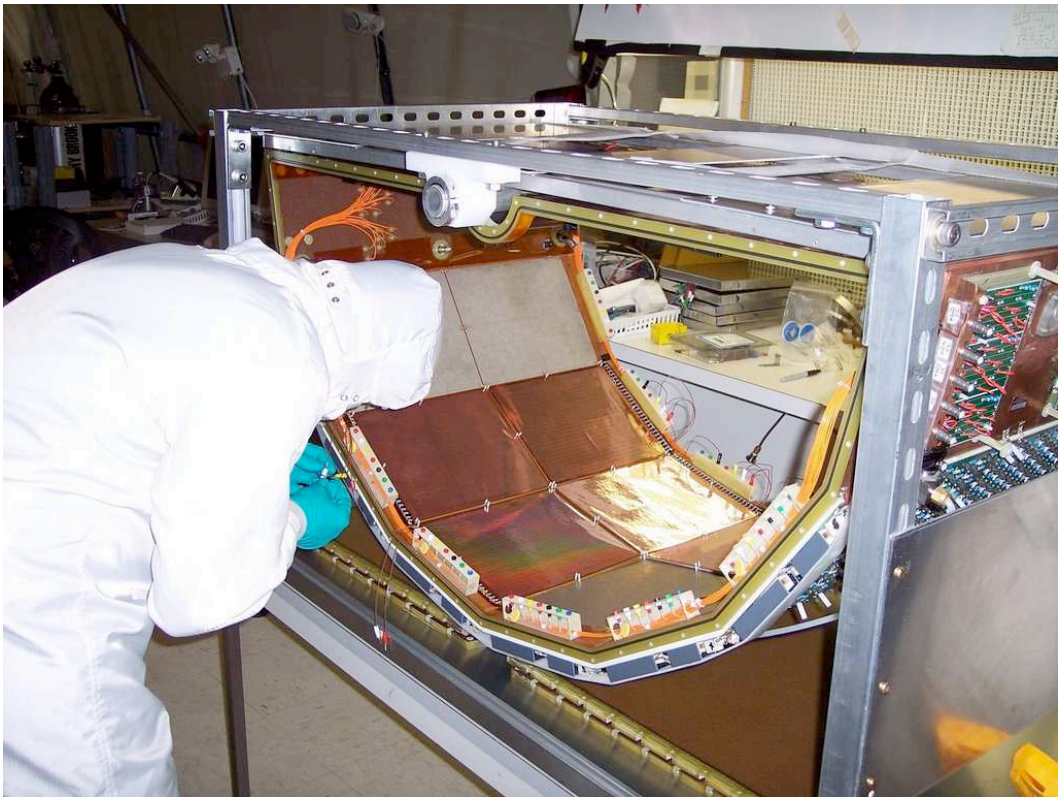

Figure 2.19: The Hadron Blind Detector vessel during assembly.

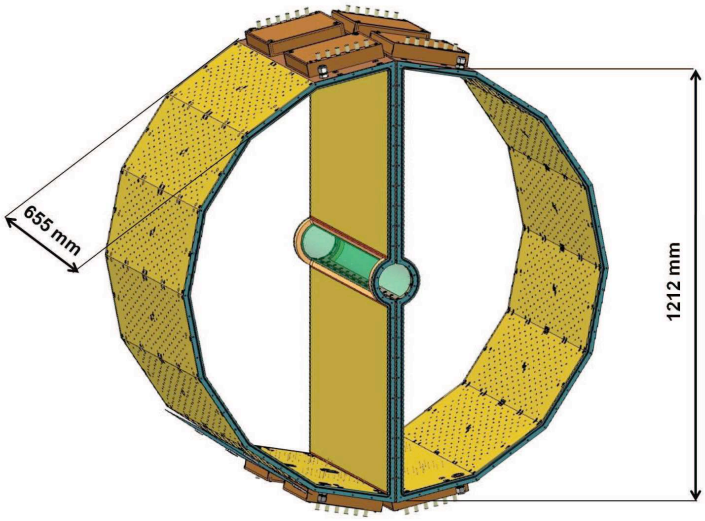


Figure 2.20: Both arms of the Hadron Blind Detector.

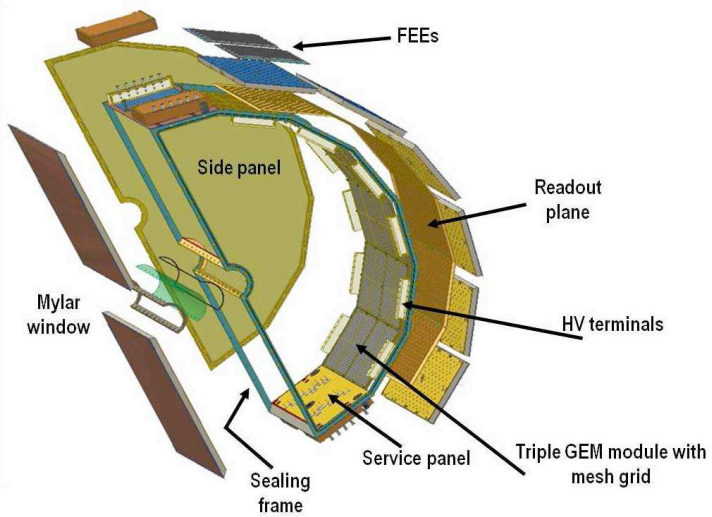


Figure 2.21: Exploded view of one arm of the Hadron Blind Detector.

of the top GEM. The hadron-blindness is a result of the electric field above the top GEM that drifts ionization away from the detector active area (see schematic in Fig. 2.22). When the HBD was installed in PHENIX for Runs 9 and 10, the central magnets were operated in the +- mode, which largely cancels the field in the region of the HBD. This preserves the orientation of electron pairs produced by collisions, so the HBD can be used to identify pairs with a small opening angle that are mostly a result of pion Dalitz decays or photon conversions.

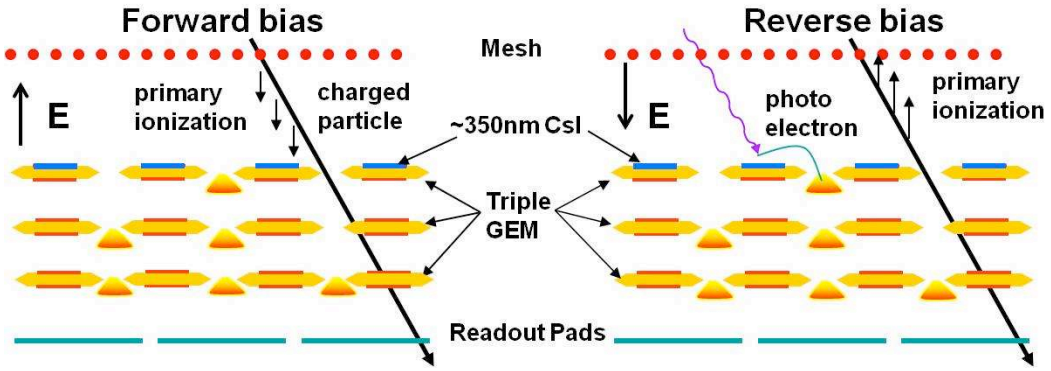


Figure 2.22: The principle behind hadron-blind operation of the detector. In forward bias mode (left panel), the ionization trail from charged hadrons is drifted toward the GEM stack and avalanched. In reverse bias mode, the ionization trail is drifted away from the GEM stack, while Cherenkov light from electrons shines onto the CsI photocathode. Photoelectrons liberated from the CsI avalanche through the GEM stack to produce an electron signal.

The coarse granularity of the HBD pad readout and its location close to the interaction region mean that Cherenkov blobs generated by electron pairs from pion Dalitz decays will usually overlap. Thus the charge deposited on a single pad or cluster of neighboring pads can determine if the electron is alone or accompanied by a low-$p_T$ partner that may not be detected in the central arms. To test the HBD response to single and double electron hits, we examine low mass pairs measured in the PHENIX central arms. Electron-positron pairs with a mass $m_{ee} < 0.15$ GeV/$c^2$, where the combinatorial background is negligibly small, are predominatly from photon conversions and pion Dalitz decays. Selecting pairs in this region gives a clean electron sample. The pairs are divided into two categories: open, where the individual tracks are matched to different clusters in the HBD; and close, where the tracks have a small opening angle and are matched to the same cluster in the HBD. The charge matched to open and close pairs is interpreted as the HBD response to single

and double electron hits, respectively. Figure 2.23 shows the response to single electrons, which shows a peak around 20 photelectrons. The double electron response is peaked around 40 photoelectrons. Efforts to use HBD information to reduce the combinatorial background for $e^+e-$ pair measurements using the Run-10 Au+Au data are ongoing. Further information on the construction and testing of the HBD can be found in Appendix A.

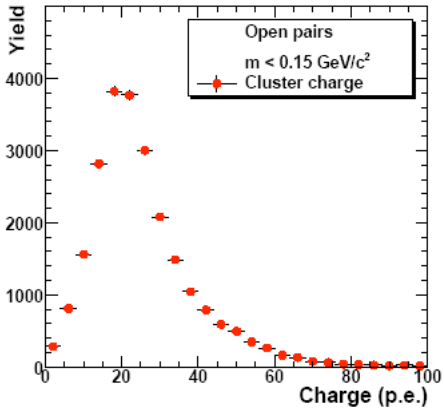


Figure 2.23: The HBD response to single electrons [57].

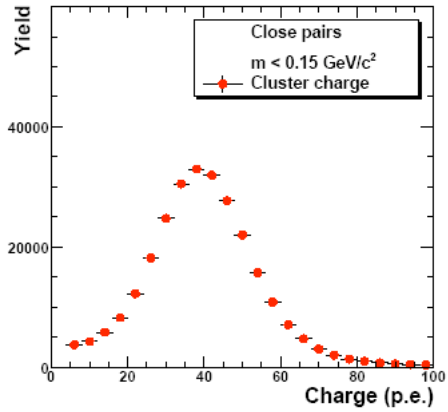


Figure 2.24: The HBD response to double electron hits.

### Silicon Vertex Detector and Forward Vertex Detector

The indirect method of measuring heavy flavor through semi-leptonic decays does not have the benefit of identifying the separate contributions from charm and bottom quarks. The separate spectra and flow of the two quark species can answer pressing questions on the mass dependence (or lack thereof) of energy loss in the medium created in Au+Au collisions. The separate measurement of the $v_2$ elliptic flow parameter can also provide contstraints on theoretical models.

Precision vertex location can allow discrimination between heavy quark species. The $D^{\pm}$ meson has a mean lifetime $c\tau = 311.8\mu$m, so the decay will happen, on average, outside of the medium produced in the heavy ion collision. The mean lifetime of the charged and neutral $B$ mesons are 491.1 and 457.2 $\mu$m, respectively. With a precise vertex measurement, the bottom contribution can be identified by the displaced $J/\psi$ vertex from the decay $B \rightarrow J/\psi + X$.

The PHENIX Silicon Vertex Detector (VTX) and Forward Vertex Detector (FVTX) are silicon tracking detectors that can locate the displaced decay vertices with a resolution of 20 $\mu$m [59].

This upgrade is divided into two sections: the central barrel, which covers $|\eta| < 1.2$ and nearly $2\pi$ in azimuth, and the forward vertex detector, which covers $1.2 < |\eta| < 2.2$ and full azimuth. The central barrel is four tracking layers wrapped around the beam pipe. The two inner layers, located at r = 2.5 and 5 cm, respectively, consist of 50 $\mu$m $\times$ 450 $\mu$m silicon pixels. The outer two layers are 80 $\mu$m $\times$ 1000 $\mu$m stripixels, and are located radially at 10 and 14 cm. The fine segmentation of the silicon sensors ensures and occupancy of less than 1% and 5% for the inner and outer layers, respectively, in central Au+Au collisions.

In addition to identifying heavy flavor via displaced vertices, the forward vertex tracker will complement muon tracking in the muon arms. Each of the two endcaps consist of 4 layers of silicon mini-strip planes. The mini-strips are arranged in wedges, which go from a width of 3.5 mm a small angles in $\phi$ to 11.3 mm at $\phi = 35^\circ$ and have a radial length of 75 $\mu$m.

The central VTX has been installed and took data during Run-11 $p + p$ collisions. The FVTX is scheduled to be installed prior to Run-12.

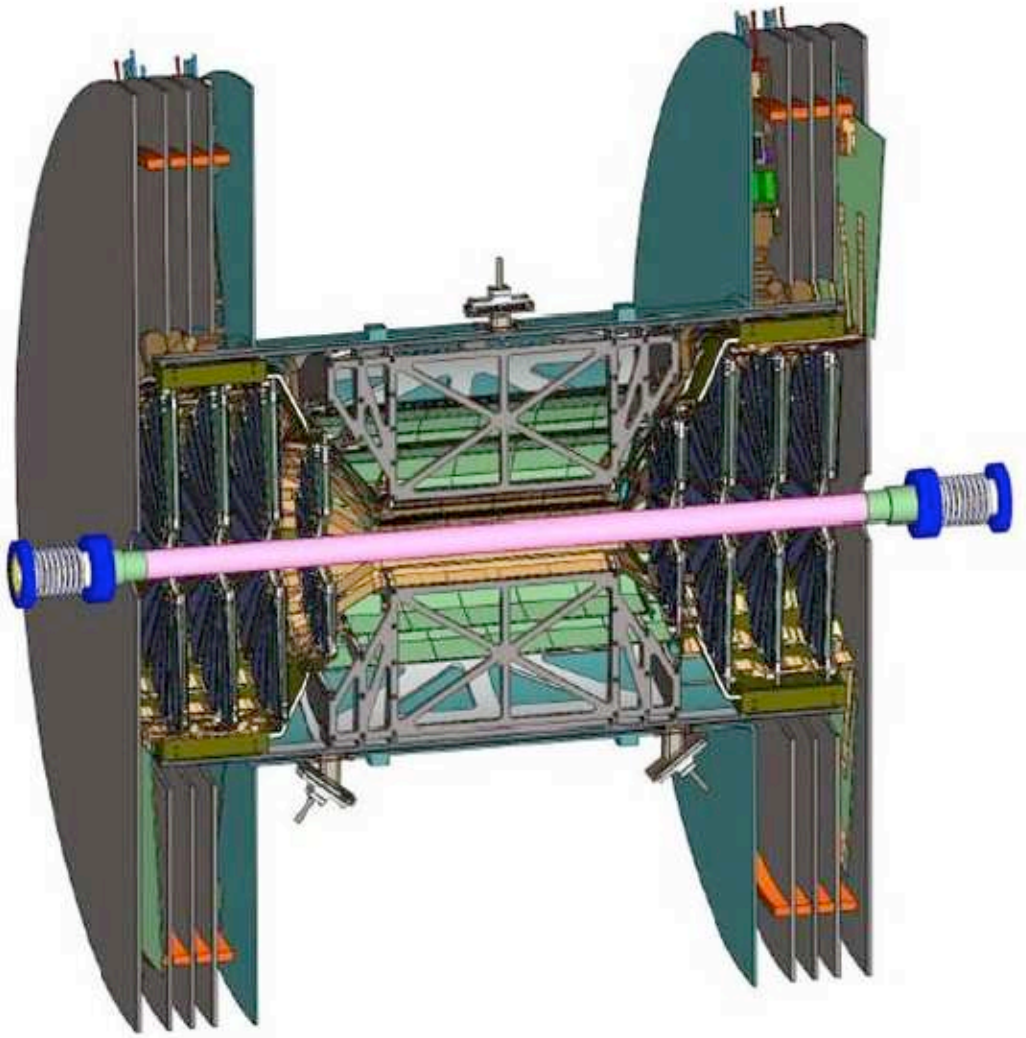

Figure 2.25: The completed PHENIX Silicon Vertex Tracker (barrel around beam pipe) and Forward Vertex Tracker (lobes at the left and right). These two subsystems will enable precise vertex determination for tracks measured by the central arms and muon arms, respectively.

# Chapter 3

# Inclusive Electron Measurement

This chapter describes a measurement of the inclusive electron spectrum from the 2008 RHIC $d$+Au Run using the PHENIX detector. Section 3.1 describes how the PHENIX experiment determines events of interest. Section 3.2 discusses how the PHENIX subsystems are used to identify electrons produced in collisions, and reject the large background of hadrons.

During this Run, the PHENIX experiment sampled 80nb$^{-1}$ of luminosity, far exceeding the Run-3 $d$+Au sample of 3nb$^{-1}$.

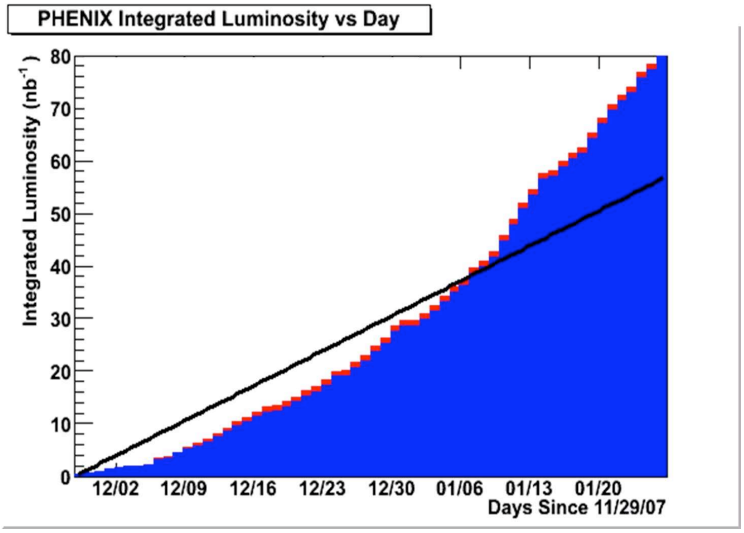


Figure 3.1: Integrated luminosity sampled by the PHENIX Experiment during Run-8. The black line shows the projected luminosity expectation from the BNL Collider Accelerator Division before the Run [45].

## 3.1 Event Selection

For an event to be recorded, one or more of the PHENIX triggers must be satisfied. The most basic trigger is the so-called "minimum bias" trigger. The name reflects the fact that this is the least selective of the triggers in PHENIX, so the events that satisfy the minimum bias trigger conditions should represent an average of all the possible impact parameters accessible in $d$+Au. For the 2008 $d$+Au Run, the minimum bias trigger required at least one phototube hit in the North (facing the incoming deuteron beam) and South BBC array (facing the incoming Au beam), and that the collision $z-$vertex be within $\pm$ 30 cm of the center of the PHENIX interaction region.

While the minimum bias triggered dataset reflects the dynamics of an average event, pressing physics questions often require knowledge of relatively rare processes (in this case, the production of an electron from a heavy quark decay). To enrich the statistical precision of measurements of these rare processes, other triggers with more specific conditions are introduced. The electron trigger considered in this analysis is called the EMcal RICH Trigger for Electrons (ERTE).

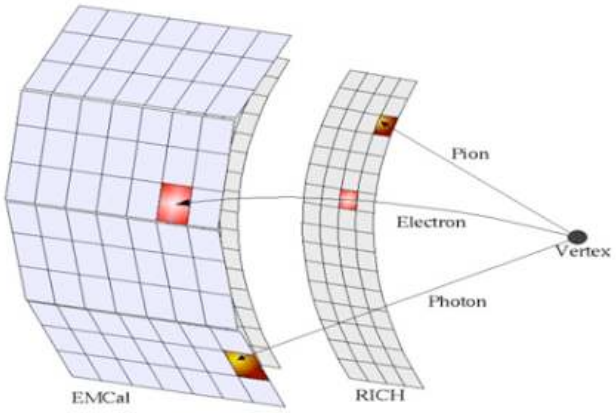


Figure 3.2: Schematic representation of the ERTE trigger. Electrons which produce a response in the RICH and EMcal will satisfy all the trigger conditions, while photons and pions generally will not.

This trigger requires a response in the RICH, followed by a deposit of energy in the EMcal over a certain threshold (either 600 MeV or 800 MeV), in addition to the requirements of the minimum bias trigger. The efficiency of this specialized electron trigger is determined by comparing tracks which satisfy the ERTE trigger to tracks from minimum bias triggered events. A

typical ERTE trigger efficiency is shown in Fig. 3.3. This trigger greatly enhances the statistics of the high momentum electron sample. Overall, this analysis considers a sample of $110\times10^9$ minimum bias events and $1.6\times10^9$ ERTE triggered events.

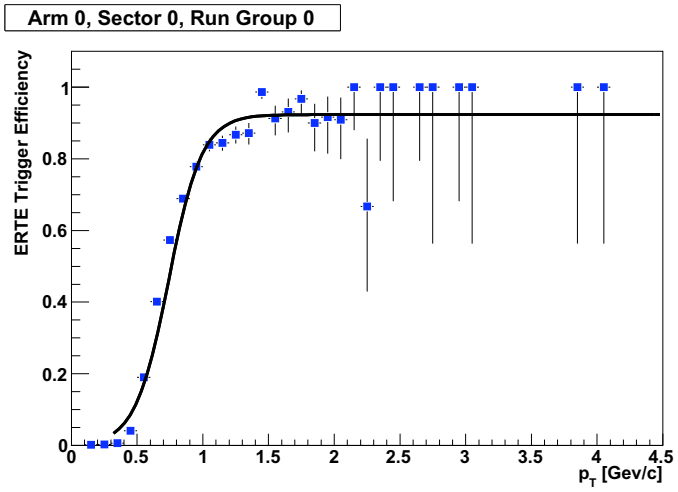


Figure 3.3: A typical ERTE trigger efficiency curve.

## 3.2 Electron Identification at PHENIX

This section describes how the various detector susbsytems are used to identify and count electron candidates at PHENIX.

## 3.3 The PHENIX Tracking Algorithm

The PHENIX tracking algorithm processes the response of the central arm tracking detectors (the drift chamber and pad chambers) to produce a set of tracks. Tracks are associated with a response from each detector subsystem they encounter. As discussed previously, the PHENIX magnetic field falls off sharply for $R > 200$ cm, where the active area of the first tracking detector begins. This allows the tracking algorithm to assume all tracks are straight after they enter the drift chamber. The algorithm also assumes all tracks originate from the $z-$vertex position determined by the BBCs.

Using the start time $t_0$ determined from the BBCs, the $x$ coordinate of tracks in the drift chamber is determined by

$$x = v_{drift}(t - t_0) \tag{3.1}$$

where $v_{drift}$ is drift velocity of ionization in the drift chamber working gas, about 50 $\mu$m/ns. Pattern recognition using a combinatorial Hough transform [55] reconstructs straight particle tracks in the $r - \phi$ plane, using hits in the drift chambers X1 and X2 wires (which are parallel to the beam axis), and gives two angles, $\phi$ and $\alpha$. The angle $\phi$ is defined at a reference radius at 220 cm inside the drift chamber (see Fig.3.4). The angle $\alpha$ is used to determine the transverse momentum $p_T$ and charge sign of the track.

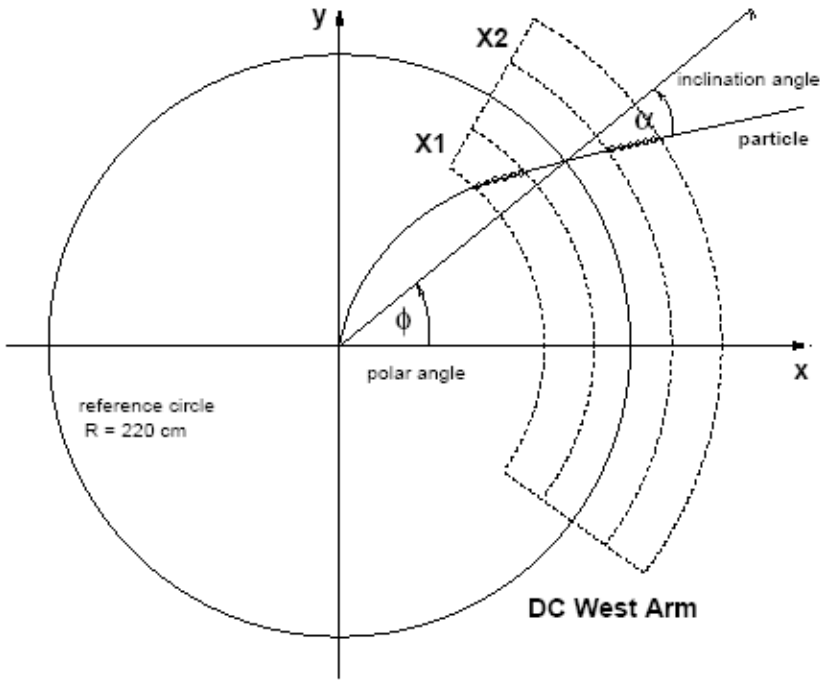


Figure 3.4: Variables used for track reconstruction in the PHENIX central arms.

Additional tracking information is necessary to determine a particle's total momentum. Tracks associated with a unique hit in PC1 use that information to fix the $z-$coordinate, and thus allow determination of the longitudinal momentum component. Tracks with multiple associations in PC1 use the PC1 hit assiciated with the most hits in the DC U and V wires. In the PHENIX software architecture, each track has an associated bit pattern, known as `quality`, that is determined by the hits in the DC and PC used in that track's recon-

struction. This analysis only considers tracks with hits in the drift chamber X1, X2, and UV planes, and an ambiguous hit in PC1 (`quality` = 31), or a unique hit in PC1 (`quality` = 63).

### 3.3.1 RICH and EMCal Response

Each subsystem that a track encounters reports a response associated with that track. For the electron measurement discussed here, the relevant subsystems are the RICH and EMcal, since they have specialized electron identification capabilities.

Electrons in the $CO_2$ radiator volume of the RICH produce on average 10 phototelectrons that are read out by the RICH phototubes. The Cherenkov angle in $CO_2$ and the geometry of the mirrors and phototubes causes the rings on the phototube array to have a radius of about 5.4 cm. The number of phototubes that fire in a ring with inner radius 3.3 cm and outer radius 8.4 cm around a track is called `n0` (see Fig. 3.5). Electron candidtate tracks are required to have `n0`$> 1$ to be considered in this analysis. At $p_T > 4.8\text{GeV}/c$, charged pions begin to radiate in the RICH, so the more strict requirement of `n0`$> 4$ is placed on tracks to help eliminate hadron contamination.

While the RICH has excellent electron identification capabilities, it lacks the precise position determination available in the tracking detectors. However, it can provide a reference point that the projection of each track can be compared to in order to place a constraint on the distance from the track to the hit in the relevant detector. In the case of the RICH, this variable is known as `disp` (short for displacement), and is defined as

$$\texttt{disp} = \sqrt{(z_{track} - z_{center})^2 - (\phi_{track} - \phi_{center})^2} \tag{3.2}$$

where $P = (z_{track}, \phi_{track})$ is the track's projection onto the RICH phototube array, and the $z$ and $\phi$ displacement are measured in cm. To be considered as electron candidates, tracks must be matched to a ring with `disp`$< 5$cm.

The electromagnetic calorimeter provides another layer of electron identification and hadron rejection, as well as providing the energy measurement for electrons and photons in PHENIX. The total energy of a relativistic electron is given by

$$E = \sqrt{m^2 + p^2} \tag{3.3}$$

in natural units. Electrons measured at PHENIX have $p >> m$, so to close approximation $E = p$. An electron will shower in the EMcal and deposit all of its energy, so the measured energy associated with the track, called `ecore`, will be equivalent to the true energy of the electron within the resolution of the

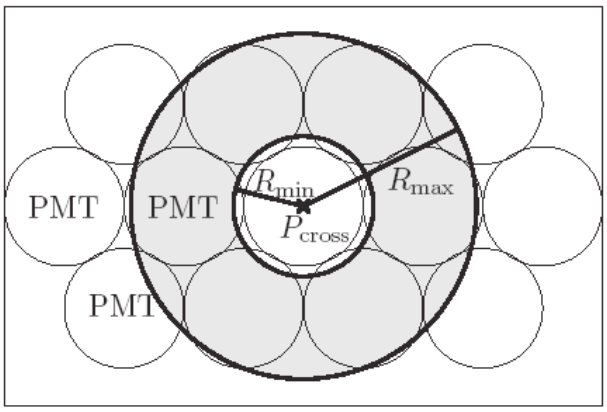


Figure 3.5: Ring definition on the RICH phototube array.

device. Thus the $E/p$ distribution of electrons from the collision vertex will be centered around one, with a width determined by a combination of the energy and momentum resolution of the PHENIX spectrometer. Charged hadrons, however, will generally not deposit all of their energy in the EMcal, and will therefore have $E/p < 1$. Conversion electrons produced away from the collisions vertex (in air or detector materials) will not experinece the full magentic field, and will have tracks that appear artificially straight to the tracking algortithm. These conversions will be reconstructed with an anomolously high $p_T$, but will have a correct energy measurement reported by the EMcal, and thus also have $E/p < 1$. Therefore a cut on $E/p$ can eliminate a large portion of the hadron background and conversions away from the vertex, while retaining the prompt electron signal.

Since the width of the electron $E/p$ distribution varies with momentum, the selection criteria is based on the sigmalized variable `dep`, which is defined as

$$\texttt{dep} = \frac{(E/p) - 1}{\sigma_{E/p}} \tag{3.4}$$

The width $\sigma_{E/p}$ is found by fitting the data (with some moderate elecron selection criteria applied) with a Gaussian. The momentum dependence of the width is parametrized by a fit with the function

$$\sigma_{E/p} = \sqrt{(A \times p_T)^2 + (\frac{B}{\sqrt{p_T}})^2 + C^2} \tag{3.5}$$

which is a quadrature sum of the momentum resolution of the PHENIX tracking systems and the energy resolution of the EMcal. To be considered in this analysis, charged tracks must have `dep` $< 2\sigma$.

The shape of showers in the EMcal can also be used to discriminate electrons from hadrons. Detailed GEANT simulations of electromagnetic showers give a predicted energy $E_{pred}$ deposited in the EMcal [60]. A measure of the "electromagnetic-ness" of the shower is defined by

$$\chi^2 = \Sigma_i \frac{(E_{meas} - E_{pred})^2}{\sigma_i^2} \tag{3.6}$$

This variable, normalized to be between zero and one, is called `prob`. Candidate electron tracks are required to point to a cluster in the EMCal within a circle of radius $2\sigma$ in $\phi$ and $z$ that has `prob`$> 0.01$, where $\sigma$ is the quadrature sum of the sigmalized track matching variables in the EMcal known as `emcsdphie` and `emcsdze`. At $p_T > 4.7\text{GeV}/c$, a more selective criteria of `prob`$> 0.2$ is applied to minimize contamination from hadrons that fire the RICH.

### 3.3.2 Global Variables and Fiducial Cuts

While the PHENIX aperture is designed to minimize conversion electrons, some are produced in the pole tips of the PHENIX central magnet, near the edges of the acceptance. These conversions are largely eliminated by restricting the $z-$vertex to be within $\pm$ 20 cm of the center of the PHENIX interaction region. Additional conversion electrons come from photon interactions in the support structures for the Hadron Blind Detector, which were present during Run-8 even though the HBD detector vessel itself was undergoing maintenance and not installed in PHENIX at that time. Additional cuts are applied to minimize the difference in active area between the data and simulation. Overall, these cuts remove about 20% of the PHENIX active area, and therefore 20% of the electron statistics, but this is an acceptable loss compared to the reduction of background and systematic uncertainties.

### 3.3.3 Run Groups

During data taking at PHENIX, the detector must be periodically disabled for maintenance, changes in the beam, and a host of other operations. As such, the data is divided into chunks called runs (with a lower-case "r" to distinguish from the annual Runs). Once the events determination and electron selection criteria are identified, the data can be inspected to check the stability of the

| Variable | Value |
|---|---|
| n0 | $> 1$ (>4 for $p_T > 4.7$ GeV/c) |
| dep | $> -2$ |
| disp | $< 5.0$ |
| prob | $> 0.01$ (>0.2 for $p_T > 4.7$ GeV/c) |
| EMcal Track Matching | emcsdphi_e$^2$ + emcsdz_e$^2$ $< 4$ |
| Track Quality | = (63 or 31) |
| Fiducial Cuts | See text |

Table 3.1: Electron identification criteria.

detector. Fig. 3.6 shows the average number of electrons with $1 < p_T < 4$ GeV/$c$ per event for minimum bias triggered $d$+Au data recorded during Run-8. The data is divided into five run groups, each of which are enclosed in red lines representing $\pm 3\sigma$ deviations from the average in the group. Any runs which fall outside this range are not considered in this analysis. As the $d$+Au Run progressed, some small sections of the PHENIX live area became unstable and had to be disabled. This small loss of live area is reflected in the gradual decrease in the average number of electron candidates per event for each subsequent run group. The data taken with the photon converter installed can clearly be seen by the dramatic increase in the number of electron candidates.

## 3.4 Hadron Contamination at High Momentum

Despite the selective electron identification criteria required at high transverse momentum, some hadron contamination can still remain in the electron candidate sample, mainly from high-$p_T$ charged pions that radiate in the RICH. Since the shower-shape variable prob is roughly independent of $p_T$ for high-$p_T$ hadrons, we can use this to estimate the hadron sample at high momentum.

First a sample of hadrons with $1 < p_T < 4$GeV/c is obtained by placing a veto on the RICH. These tracks pass all the high-momentum electron selection criteria described above, except for n0 (in order to select hadrons), prob(as described below) and the dep variable, because the $E/p$ distribution is used to examine the hadrons. This sample is divided into two groups based on their value of prob, namely those with prob greater than and less than 0.2. The $E/p$ distributions and ratio of these two samples are shown below.

To examine hadrons above the RICH threshold, we prepare $E/p$ distributions of hadrons that pass all of the tight electron cuts at high momentum,

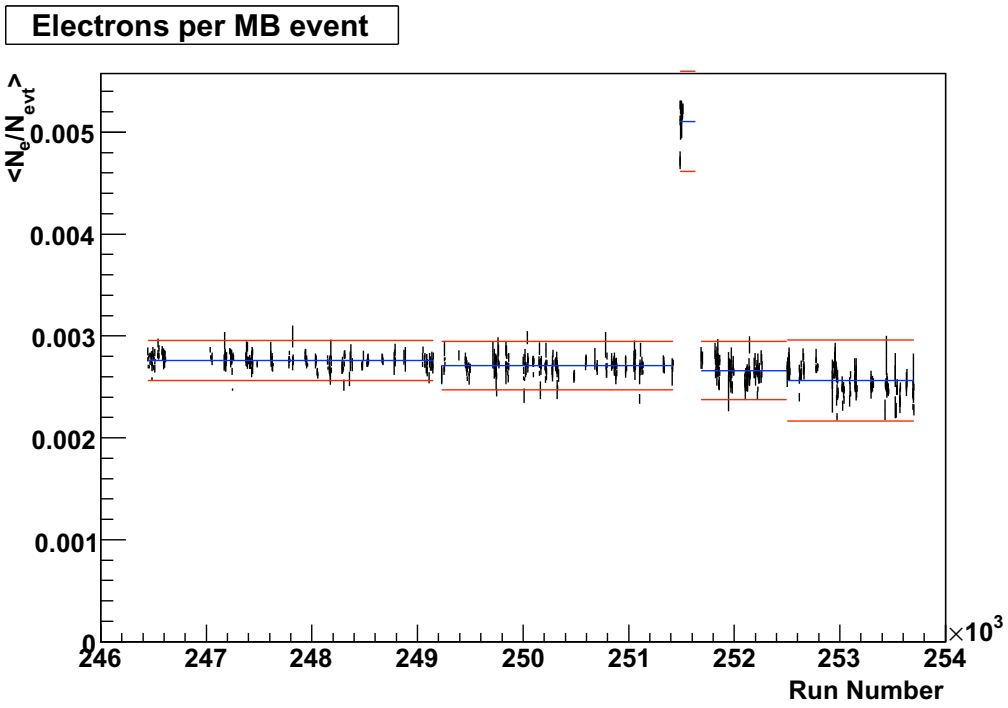


Figure 3.6: The average number of tracks passing the standard electron identification cuts per event for the runs used in this analysis. The blue and red lines represent the average $\pm 3\sigma$ for each run group.

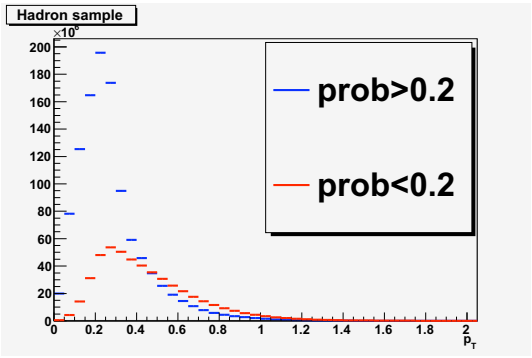


Figure 3.7: The two hadron samples.

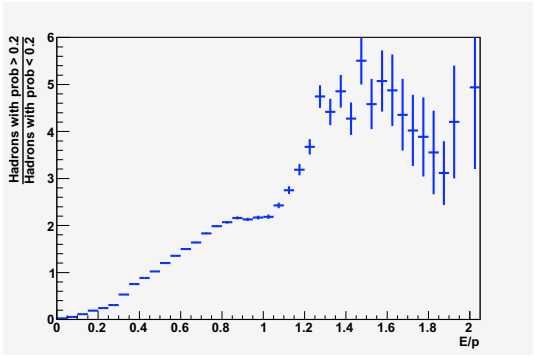


Figure 3.8: Ratio of the hadron distributions.

including `n0`, with the exception that the `prob` cut is reversed to `prob` $< 0.2$. This change removes the vast majority of electrons, providing us with a heavily contaminated sample. This distribution is multiplied by the ratio shown in Fig. 3.8, providing an estimate of the $E/p$ distribution of hadrons which pass the tight electron cuts. These distributions are shown in Fig. 3.9 below. Over the momentum range of this measurement, the hadron contamination is found to be negligible.

## 3.5 Correction to Full Azimuth

The purpose of this analysis is to count electrons from the decays of heavy quarks produced in $d$+Au collisions. As can be seen from Fig.2.2, the incomplete solid angle and pseudorapidity coverage of the PHENIX detector allows many of the electrons from the interaction to go undetected. In order to compare results with other experiments and theoretical calculations, it is desirable to correct the measured electron spectrum up to full acceptance in azimuth and $\pm$ 1 unit of rapidity. In addition to the losses due to detector geometry, the selection criteria used to identify electron tracks will inevitably eliminate some true electrons.

Both the acceptance and efficiency losses can be modeled with a GEANT simulation of the full PHENIX detector. In the virtual world of simulation, we know the complete dynamics of the input particles, and can use the differences between this known input and the simulated PHENIX measurement to determine the effects that are solely due to the detector. It is crucial that our input particles and simulated detector response accurately mimic the realities of the physical world to get an accurate picture of the detector effects.

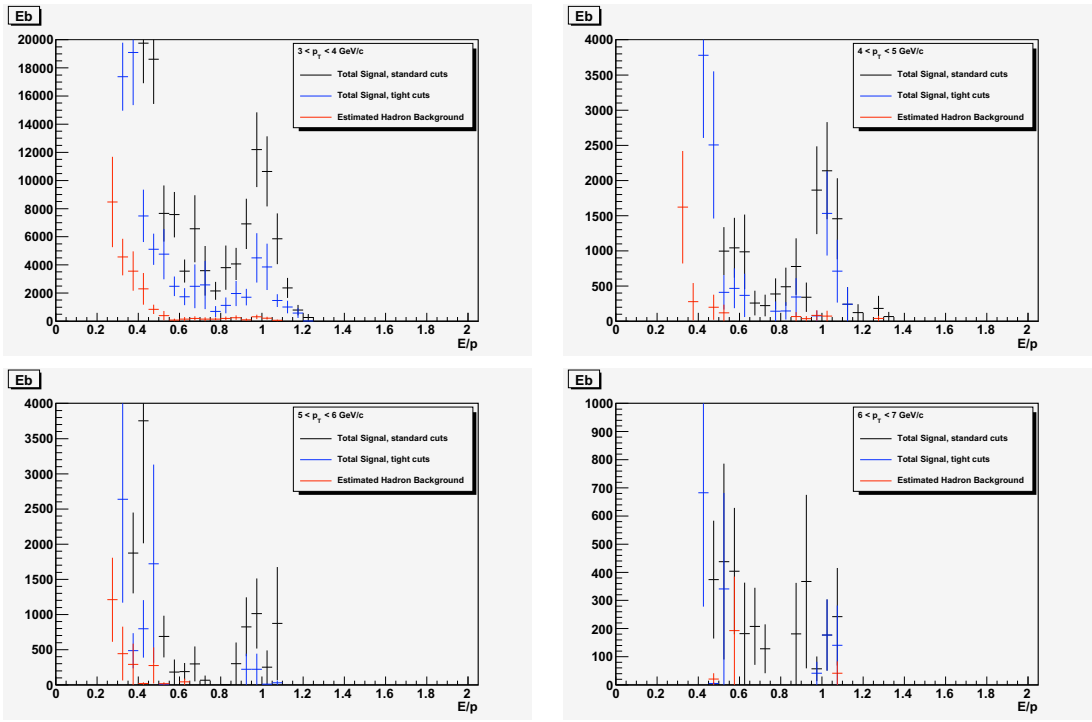


Figure 3.9: $E/p$ distributions used to estimate hadron contamination in the electron sample.

### 3.5.1 Simulation Input

To mimic the source of electrons of interest in PHENIX (a $d$+Au collision), we generate 5 million electrons and 5 million positrons with the following characteristics:

- Isotropic in azimuth, $0 < \phi < 2\pi$.
- Flat in rapidity, $-0.5 < y < 0.5$.
- A flat $z-$vertex distribution, -30 cm $< z-$vertex$<$30 cm.
- Flat in transverse momentum, $0 < p_T < 15$ GeV/c.

By convering the full azimuth and one unit of rapidity, the comparison of the simulated measured spectrum of electrons to the input spectrum will give the proper geometrical factors to correct up the incomplete PHENIX acceptance. The $z-$vertex distribution is wider than the accepted `bbcz` range of $\pm$20 cm, in order to simulate any "edge effects" that can occur due to the finite vertex resolution. In order to have meaningful statistics at high transverse momentum, the simulated electrons are generated flat in $p_T$, but then weighted by a fit to the raw electron $p_T$ spectrum (see Fig. 3.10) to more accurately resemble a natural electron distribution. The slight mismatch between the data and the fit parametrization at high $p_T$ is unimportant here, as the acceptance correction in this momentum range is flat (see Fig. fig:eff$_t$ot).

### 3.5.2 The Simulated PHENIX Detector

The GEANT simulation of the PHENIX detector uses Monte Carlo techniques to model the response of the various detector subsystems. The simulated response is processed by the same tracking algorithm used on the actual $d$+Au data to reconstruct the simulated electron tracks. To ensure the simulation represents an accurate model of the actual PHENIX detector, the simulated values of various parameters are compared to the measured values of those same parameters from the Run-8 $d$+Au dataset.

#### Geometric Match

A proper representation of the active area of the PHENIX detector is necessary to correctly compute the acceptance correction up to full azimuth and one unit of rapidity. The various subsystems in PHENIX produce maps of their live channels during a specified time period when the detector is stable (in this case, during run 248040), which are input into the detector simulation. The distribution of the $\phi$ variable in simulation and data is shown in Fig. 3.11.

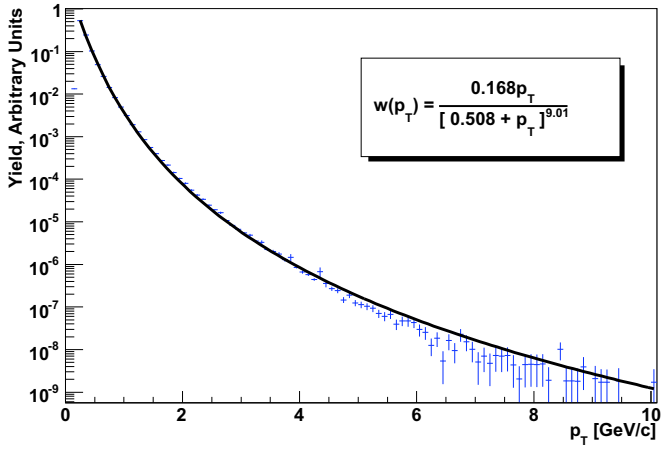


Figure 3.10: Weighting function for the simulated electron distribution. The function was determined by a fit to the raw (uncorrected for acceptance and efficiency) electron spectrum from the minimum bias triggered data.

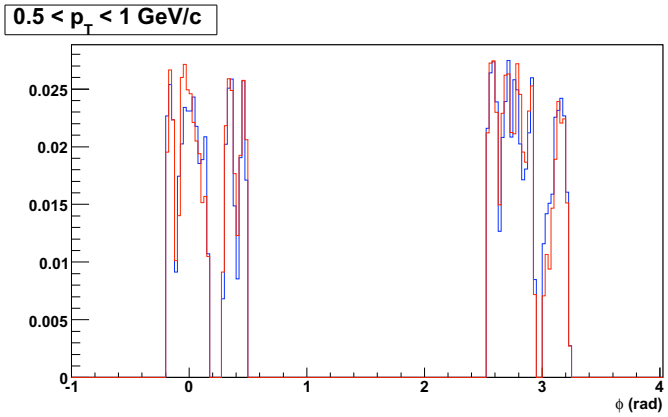


Figure 3.11: The distribution in $\phi$ of reconstructed tracks in simulation (blue) and data (red).

### Track Variable Match

It is inevitable that the electron selection criteria applied will eliminate some of the actual electron signal along with the background hadrons. This loss of efficiency must be modeled and corrected for in order to obtain the true inclusive electron yield. The distributions of the various electron identification variables are shown in simulation and data below (Fig. 3.12). The good agreement ensures that the detector response and efficiency is modeled correctly.

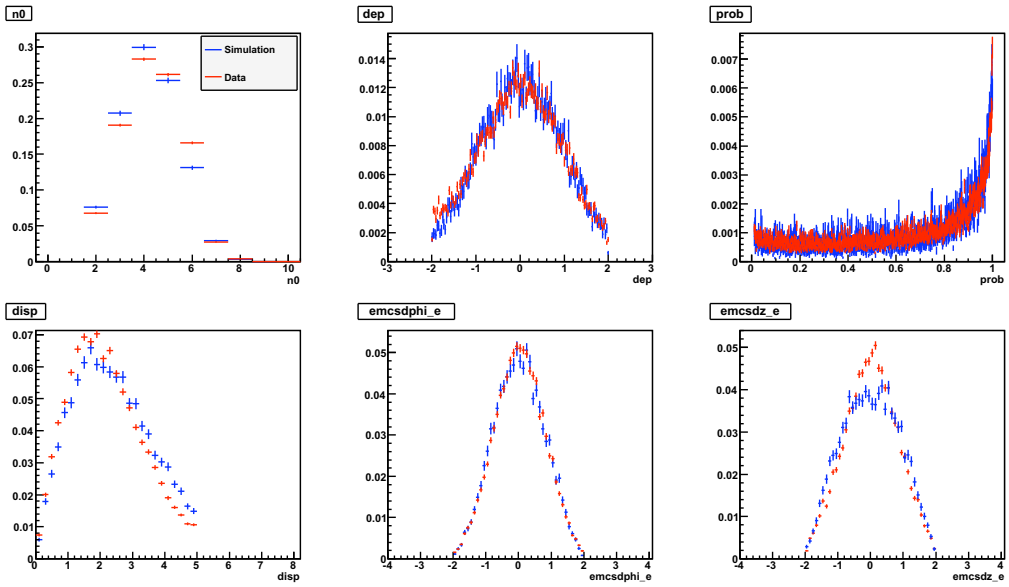


Figure 3.12: Electron ID variables in simulation and data.

## 3.5.3 Acceptance × Efficiency Correction

Once the simulation accurately matches the data, the acceptance × efficiency correction as a function of $p_T$ can be found simply by comparing the distribution of the simulated measured electrons to the known input of generated electrons, that is

$$\alpha \times \epsilon = \frac{dN^{rec}/dp_T^{rec}}{dN^{gen}/dp_T^{gen}} \tag{3.7}$$

The resulting correction is shown in Fig. 3.13, along with a fit.

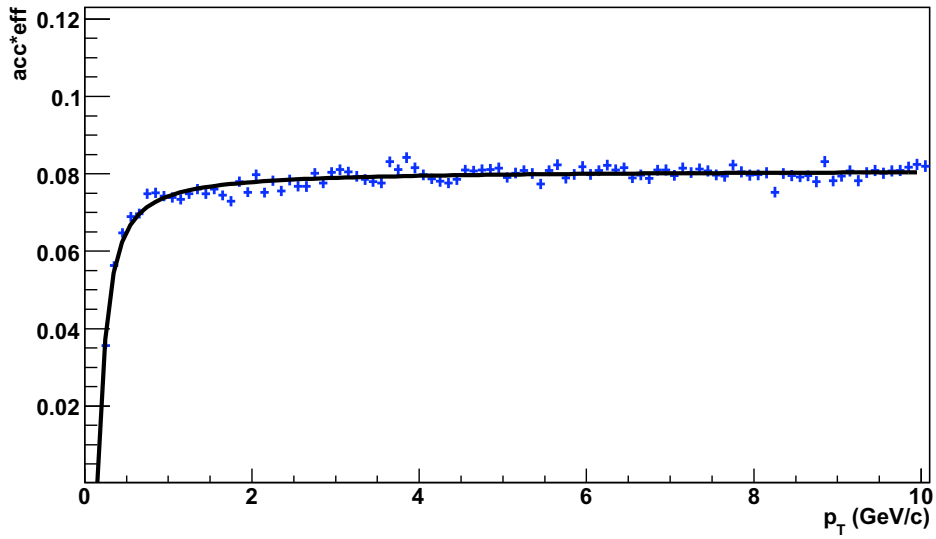


Figure 3.13: The acceptance × efficiency correction.

## 3.6 Systematic Uncertainties on the Inclusive Electron Yield

There are two basic sources of uncertainty in the measurement of the inclusive electron spectrum. The first is the mismatch in the detector geometry between the simulation and data, which is necessary for the solid angle correction up to full azimuth and one unit of rapidity. The other is the uncertainty in the model of the electron identification efficiency as calculated by the Monte Carlo PHENIX simulation. Both of these sources manifest themselves in several ways, which are discussed below.

### 3.6.1 Geometric Uncertainties

#### Changing Live Area

As can be seen in Fig. 3.6, the average number of electron candidates per event slighly decreases in each non-converter run group because of decreasing detector live area. The map of dead channels that is used to fix the live area in simulation was determined from data in run 248040, which is part of the first run group. Thus the acceptance correction will only be valid for the first run group. However, if the change in the number of electrons per event is truly only due to changing live area, a correction factor can be applied to the other

run groups to give the same yield per event as the first run group and thereby correct for the changing live area.

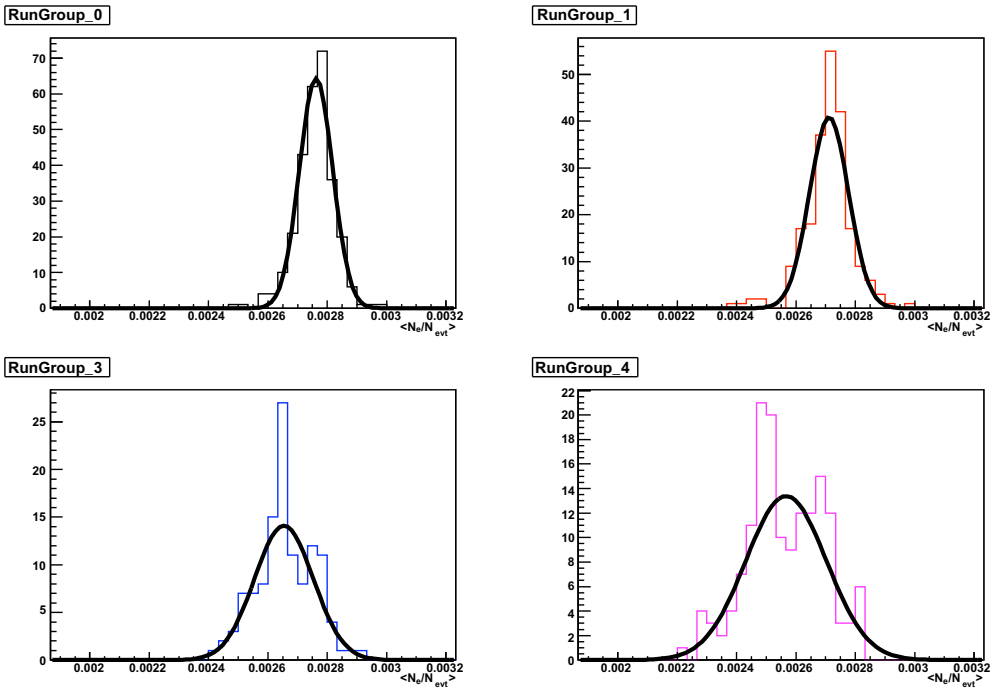


Figure 3.14: Fits for the average number of electrons per event for each non-converter run group.

The mean of a Gaussian fit to the distribution of $< N_e/N_{evt} >$ for each run group is compared to the mean for the first run group. The relative acceptance is found by calculating

$$\alpha_{rel}(i) = \frac{< N_e/N_{evt} >_i}{< N_e/N_{evt} >_0} \tag{3.8}$$

for each subsequent run group. The electron yield determined from this run group is divided by this factor to account for the missing live area. The statistical uncertainty on the mean determined from each run group is less than 1%, but the uncertainty on the correction factor is rounded up to an uncertainty on the inclusive yield of 1%.

### Geometric Match with Simulation

With the above correction factor in applied, all data should produce an electron yield corresponding to the live area of the first run group. The task at hand is

| | $< N_e/N_{evt} >$ | Relative Acceptance |
|---|---|---|
| Run Group 0 | 0.00276 $\pm$0.000003 | 1 |
| Run Group 1 | 0.00271 $\pm$0.000005 | 0.981 |
| Run Group 2 | N/A | 0.981 |
| Run Group 3 | 0.00265 $\pm$0.000010 | 0.960 |
| Run Group 4 | 0.00256 $\pm$0.000013 | 0.927 |

Table 3.2: Relative acceptance for each run group. Run group 2, containing the converter data, uses the relative acceptance calculated for run group 1. The error on $< N_e/N_{evt} >$ is the uncertainty on the mean of the Guassian fit to the data.

to calculate the uncertainty on the correction from the live area of the first run group to full azimuth and one unit of rapidity, as determined by simulation.

This uncertainty is estimated by calculating the integrated dN/d$\phi$ in simulation and data for one arm only of the PHENIX spectrometer. The data is then normalized to have the same integral as the simulation in that arm. The same normalization factor is then applied to the data taken by the opposite arm of the spectrometer and compared to simulation. The difference in integrated dN/d$\phi$ is found to be 4.8% when the procedure is done for either arm, so a systematic error of 5% is assigned to the inclusive electron yield.

### 3.6.2 Electron Identification Uncertainties

#### High Momentum Extension

As described previously, the electron selection criteria are tightened above $p_T = 4.7$ GeV/$c$ to remove contamination from charged hadrons that begin to radiate in the RICH (see Tab 3.1 for a summary). However, these criteria also remove a significant number of signal electrons. To estimate this loss, we examine the $p_T$ distribution of tracks that pass the standard and tightened electron identification criteria in Fig. 3.16. The ratio of these two spectra are shown in the right panel. At $p_T < 4.7$ GeV/$c$, the electron sample should be basically free of hadrons, and a fit to a constant value at $1 < p_T < 4$ GeV/$c$ shows that only about 40% of tracks that pass the standard selection

criteria also pass the tightened criteria. The gradual drop of the ratio for $p_T > 5$ GeV/$c$ shows that the more selective criteria are indeed removing hadron contamination that passes the standard cuts. To correct for this loss of signal, the efficiency loss determined by the constant fit at low momentum is divided out of the yields obtained with the tight selection criteria.

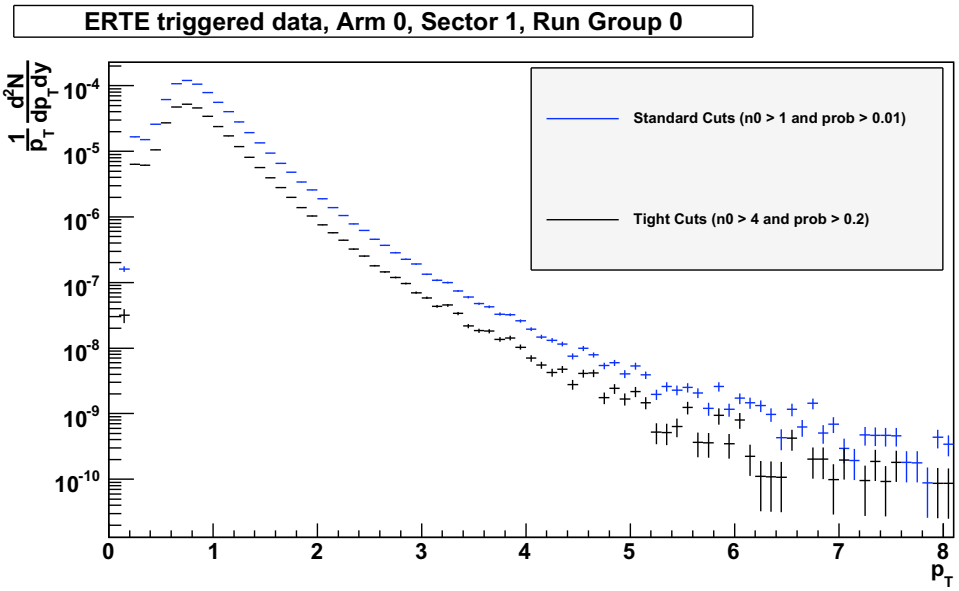


Figure 3.15: Tracks that pass standard and tight electron selection criteria.

Here we have made the assumption that the correction determined at low $p_T$ can be applied to the high $p_T$ data, or, equivalently, the assumption that the `prob` and n0 distributions for electrons are independent of momentum in this range. A systematic uncertainty of 2% is assigned to the yield determined with this method to cover this assumption.

### Electron ID Efficiency

As discussed previously, the electron identification efficiency is determined by a GEANT simulation of the PHENIX detector that models the individual subsystems response to electrons. If the simulation perfectly recreated the response to electrons, then any set of electron selection criteria would give the same electron yield, after correction for the detector efficiency determined by that set of cuts. To test the simulation's accuracy, we prepare three sets of

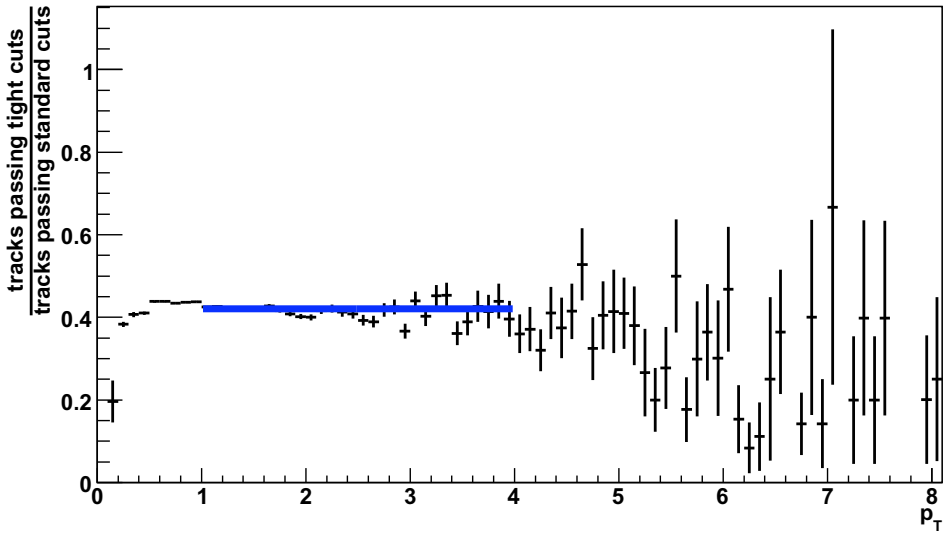


Figure 3.16: Ratio of the two spectra, with a constant fit at $1 < p_T < 4$ GeV/$c$.

electron selection criteria (see Tab. 3.3) and three corresponding acceptance $\times$ efficiency corrections, and compare the measured yields.

Figure 3.18 shows the $p_T$ spectra of tracks that pass the three different sets of selection criteria before any corrections, and Fig. 3.17 shows the acceptance $\times$ efficiency correction curves calculated for each set. As expected, the more selective criteria have a lower number of counts and lower efficiency, while the least selective criteria have higher yields and efficiencies.

The ratios of the efficiency corrected data are shown below. Note that the solid angle correction is also applied to obtain the corrected data shown in Fig. 3.19, but is a common factor that cancels out when making the ratios, leaving only the difference in the efficiency corrections. Each ratio indicates that the sets of electron identification criteria and efficiency corrections differ from the standard cuts by about 5%. A systematic uncertainty of 6% is assigned to the inclusive electron yield determined with the standard cuts to cover these discrepancies.

The total systematic uncertainty on the inclusive electron yield is obtained by adding each source of uncertainty in quadrature. A summary of the systematic uncertainties is given in Tab. 3.4.

| Parameter | Loose Cuts | Standard Cuts | Tight Cuts |
|---|---|---|---|
| n0 | $>= 1$ | $>= 2$ | $>= 5$ |
| disp | $< 10.0$ | $< 5.0$ | $< 5.0$ |
| prob | $> 0.001$ | $> 0.01$ | $> 0.2$ |

Table 3.3: The sets of electron identification parameters used to evaluate the systematic uncertainty on the efficiency correction.

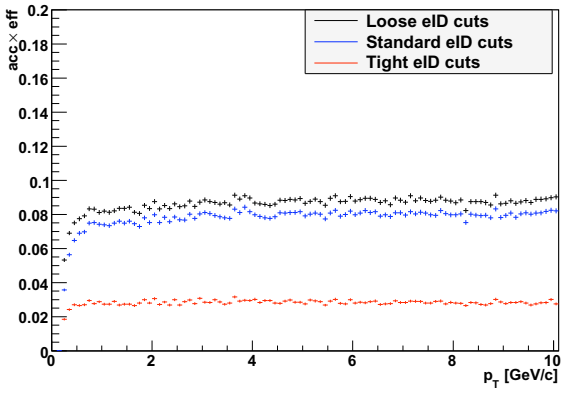


Figure 3.17: The acceptance $\times$ efficiency correction for the three sets of electron selection criteria.

| | |
|---|---|
| Live Area Correction | 1% |
| Geometric Matching | 5% |
| High $p_T$ Extension(only for $p_T > 4.7$GeV/c) | 2% |
| Electron ID Efficiency | 6% |

Table 3.4: Systematic errors on the inclusive electron spectrum.

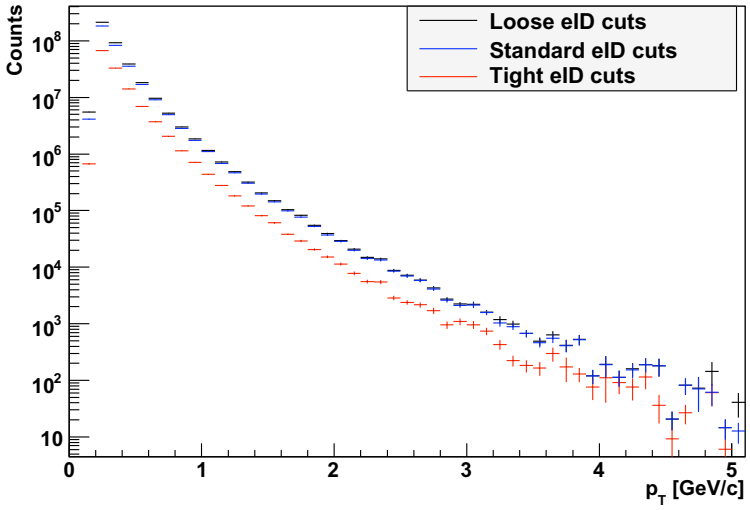


Figure 3.18: Transverse momentum distribution of tracks obtained with the three sets of selection criteria, before any efficiency corrections are applied.

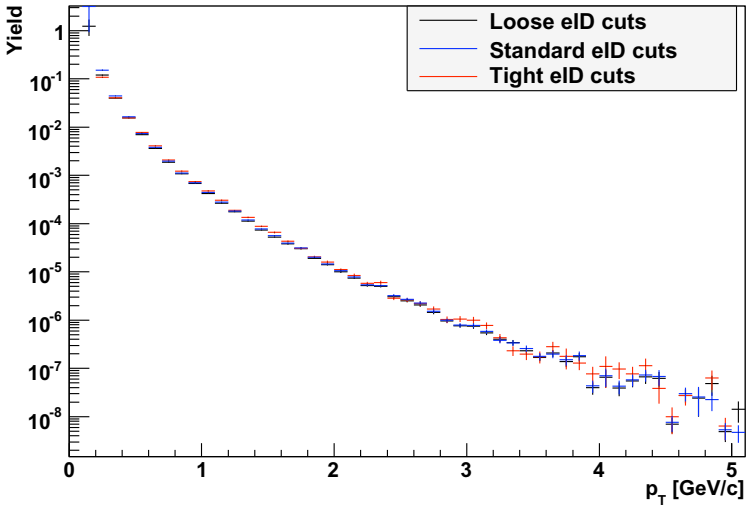


Figure 3.19: The same spectra, after efficiency corrections.

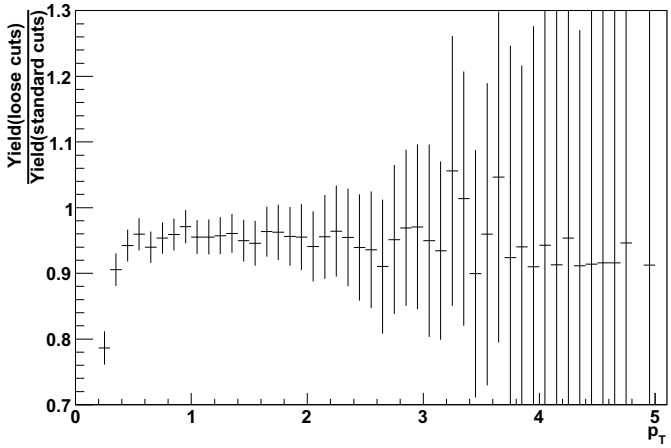


Figure 3.20: Ratio of the inclusive electron yield measured with the "loose" selection criteria to that measured with the standard selection criteria.

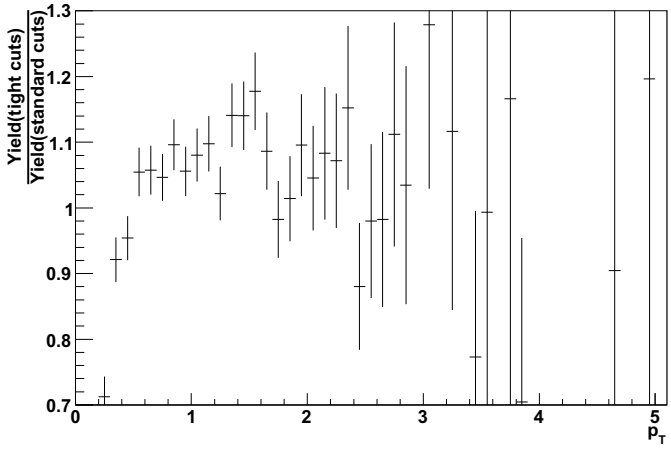


Figure 3.21: Ratio of the inclusive electron yield measured with the "tight" selection criteria to that measured with the standard selection criteria.

# Chapter 4

# Isolating the Heavy Flavor Signal

Most of the electrons measured in the PHENIX central arms come not from heavy flavor decays, but instead from a variety of background sources. The background electrons come from decays of light mesons, photon conversions, and internal and external conversions of direct photons. This chapter describes two different methods for determining the electron background and isolating the signal from heavy flavor decays. The consistency of the two methods is an important cross-check of the results, and is discussed in the final section of this chapter.

## 4.1 Cocktail Method

In this straightforward method, a cocktail of background electrons is subtracted from the inclusive electron measurement in order to isolate the contribution from heavy flavor. The versatility of the PHENIX detector has allowed precise measurements of many of the background sources of electrons; using these measurements as input to the background calculation reduces the assumptions one must make and thus minimizes systematic errors.

### 4.1.1 Cocktail Ingredients

#### Light Mesons

Electrons from the neutral pion Dalitz decay $\pi^0 \to \gamma e^+ e^-$ are the dominant source of background. The $\eta$ meson Dalitz decay is also important, contributing about 10% of the total background for $1 < p_T < 10$ GeV/c. Of less

significance are the decays of the $\eta', \rho, \omega$, and $\phi$ mesons, but these are included in the cocktail for completeness.

The general procedure is to parametrize the $p_T$ spectrum of the parent particles and use this as input to a Monte Carlo based decay generator. The following light meson decays are included in the cocktail calculations:

- $\pi^0 \to \gamma e^+ e^-$
- $\eta \to \gamma e^+ e^-$
- $\eta' \to \gamma e^+ e^-$
- $\rho \to e^+ e^-$
- $\omega \to \pi^0 e^+ e^-$ & $\omega \to e^+ e^-$
- $\phi \to \eta e^+ e^-$ & $\phi \to e^+ e^-$

PHENIX has measured both neutral [41] and charged pion [35] spectra in $d$+Au collisions. A modified Hagedorn function is fit to the combination of the $\pi^0$ data and the average $(\pi^+ + \pi^-)/2$ of the charged pion data for each centrality:

$$\frac{1}{2\pi p_T}\frac{d^2N}{dp_T dy} = \frac{c}{[e^{ap_T - bp_T^2} + p_T/p_0]^n} \tag{4.1}$$

The fit and a comparison with the Minimum Bias sampled data are shown in Fig. 4.1. A summary of the fit parameters for each centrality is given in Tab. 4.1. It is interesting to note that only the normalization parameter $c$ shows large changes between the different centrality classes. This suggests that the shape of the pion $p_T$spectrum is consistent across the range of impact parameters that is accessed in $d$+Au collisions. This is observed in the lack of strong modification of the pion $R_{dA}$, as previously discussed (see Fig. 1.9 and discussion).

The parametrization of the other light mesons is obtained by $m_T$-scaling the fit to the pion spectrum. The variable substitution

$$p_T \to m_T = \sqrt{p_T^2 + (M_{meson}^2 - m_{\pi^0}^2)} \tag{4.2}$$

gives the shape of the meson's $p_T$ spectrum, while the normalization is determined by the ratio of the meson to pion yield at high momentum (see Tab. 4.2).

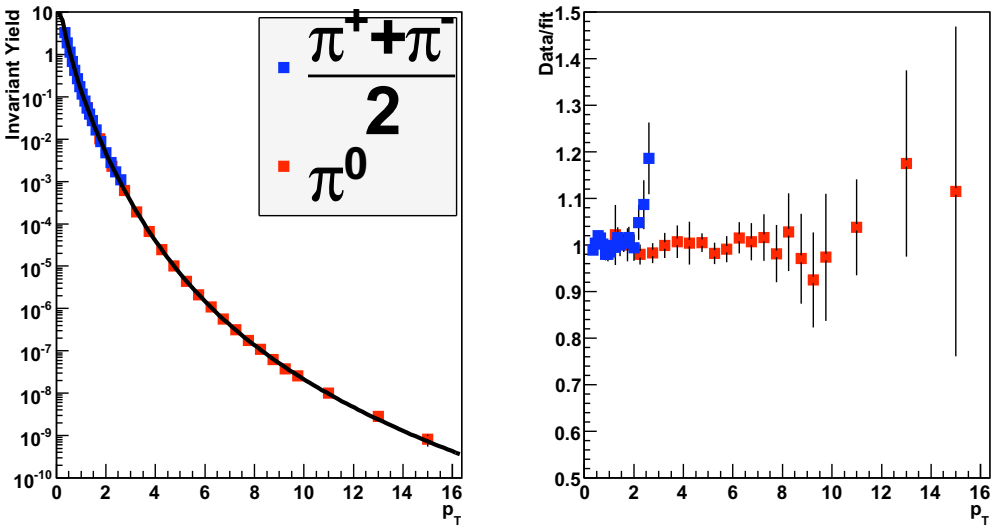


Figure 4.1: The fit function used to represent the parent pion spectrum in the Monte Carlo decay generator, and the ratio of the data to the fit.

| Centrality | $c$ [(GeV/c)$^{-2}$] | $a$ [(GeV/c)$^{-1}$] | $b$ [(GeV/c)$^{-2}$] | $p_0$ [GeV/c] | $n$ |
|---|---|---|---|---|---|
| Min. Bias | 36.1555 | 0.321832 | 0.0963188 | 0.778255 | 8.32398 |
| 0-20% | 54.4193 | 0.309235 | 0.104949 | 0.808066 | 8.41751 |
| 20-40% | 42.1531 | 0.315233 | 0.0870666 | 0.797958 | 8.37718 |
| 40-60% | 32.5864 | 0.345584 | 0.0822427 | 0.762228 | 8.26455 |
| 60-88% | 20.9207 | 0.362259 | 0.0846673 | 0.707429 | 8.1376 |

Table 4.1: Fit parameters for the Hagedorn function used to represent the pion spectrum in the Monte Carlo decay generator.

### Photon Conversions

Conversion electrons (mainly from external conversions of photons from $\pi^0 \to \gamma\gamma$ in material) are the next highest background source, behind the pion Dalitz decay. The PHENIX configuration prior to Run-6 included a helium bag in the inner detector to minimize the material (in this case, air) between the beam pipe and drift chamber, and thus minimize conversions. However, in Run-8, the helium bag was removed to make room for various detector upgrades. As in all Runs, the beam pipe also provides conversion material.

Since the majority of these conversion electrons come from the conversion

| | |
|---|---|
| $\eta/\pi^0$ | $0.47 \pm 0.03$ [ [42]] |
| $\rho/\pi^0$ | $1.00 \pm 0.30$ [ [19]] |
| $\omega/\pi^0$ | $0.90 \pm 0.06$ [ [19]] |
| $\eta'/\pi^0$ | $0.25 \pm 0.075$ [ [19]] |
| $\phi/\pi^0$ | $0.40 \pm 0.12$ [ [61]] |

Table 4.2: Meson/$\pi^0$ ratios at high momentum. Of these, only the $\eta$ meson is a significant source of background.

of a photon from $\pi^0 \to \gamma\gamma$, the kinematics of the daughter $e^+e^-$ pair will closely resemble those of electrons from pion Dalitz decays, $\pi^0 \to \gamma e^+e^-$. One can take advantage of this fact to estimate the conversion electron contribution simply by scaling up the pion Dalitz decay contribution by an appropriate factor $f^{\pi^0}$.

We use a full GEANT simulation of the PHENIX detector to determine this factor. As input to the simulation, the decay generator is tuned to give the spectrum of daughter products from the decays $\pi^0 \to \gamma\gamma$ and $\pi^0 \to \gamma e^+e^-$, using the Minimum Bias Hagedorn fit parametrization of the parent pion spectrum. The spectra of tracks passing the standard electron cuts shown in Tab. 3.1 from both input sources are shown in Fig. 4.2. Since the $\pi^0 \to \gamma\gamma$ decay does not produce any primary electrons, all tracks passing the electron cuts from this input must be the result of photon conversions.

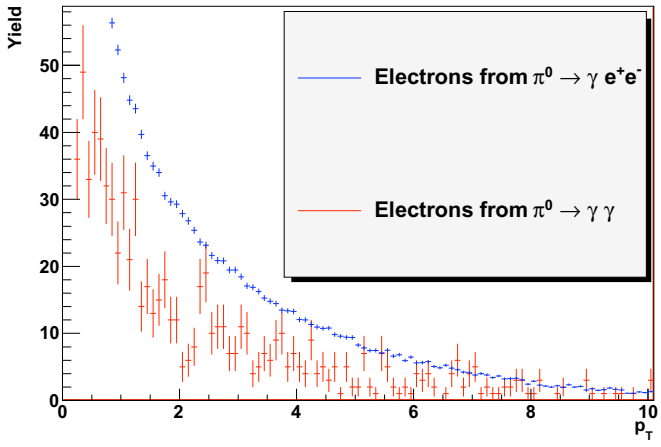


Figure 4.2: Spectra of simulated electrons from neutral pion decays. Electrons from the $\pi^0 \to \gamma\gamma$ decay are all conversions.

The ratio of the two spectra in Fig. 4.2 gives the appropriate conversion

factor $f^{\pi^0}$. As shown in Fig. 4.3, this ratio is basically flat across a wide range of $p_T$, which supports the assertion that the conversions can be accounted for simply by scaling up the pion Dalitz decay contribution. A fit to a constant gives a conversion factor $f^{\pi^0}_{Run-8} = 0.429$ . This is slightly higher than the equivalent value from Run-4 of $f^{\pi^0}_{Run-4} = 0.403$, which is expected since the Run-4 PHENIX configuration included the helium bag while the Run-8 configuration did not. A conservative systematic error of 10% is assigned to this factor to reflect the uncertainty in the amount of material in the PHENIX aperture and any discrepancies between the simulation and reality.

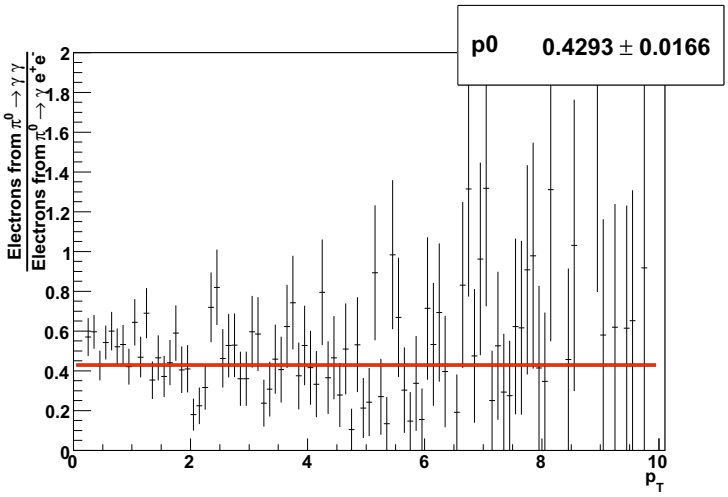


Figure 4.3: The ratio of electrons from simulated conversions to those from simulated pion Dalitz decays.

A similar factor $f^{\eta}$ is used to account for conversions of photons from the decay $\eta \to \gamma\gamma$. The two factors only differ by the relative branching ratio between their decays to photons and Dalitz decay, i.e. they obey the relation

$$\frac{f^{\pi^0}}{f^{\eta}} = \frac{\frac{BR(\pi^0 \to \gamma\gamma)}{BR(\pi^0 \to \gamma e^+ e^-)}}{\frac{BR(\eta \to \gamma\gamma)}{BR(\eta \to \gamma e^+ e^-)}} \tag{4.3}$$

where $BR(\pi^0 \to \gamma\gamma)$ is the branching ratio for the neutral pion decay to two photons. Using the values for the branching ratios found in [19], we find $f^{\eta} = 0.342$.

### Kaon Decays

Electrons from the $K_{e3}$ decay of charged kaons ($K^{\pm} \rightarrow \pi^0 e^{\pm} \nu_e$) must be handled in a somewhat different manner than the decays of other mesons. These decays occur away from collision vertex (for charged kaons, $c\tau = 3.7$ m), so the electrons from the decay do not experience the full field of the PHENIX magnet. Since the track reconstruction algorithm assumes all particles originate at the collision vertex, these electron tracks are reconstructed with an erroneously high momentum. The cut on $E/p$ (specifically the *dep* variable) eliminates most of this background, but a small amount manages to get through.

To estimate the remaining $K_{e3}$ background, we generate decays of kaons using a parametrization of the measured p+p kaon spectrum scaled up by $< N_{coll} >$ and put them through a full GEANT simulation of the PHENIX detector and magnetic field. These simulated tracks are reconstructed with the same algorithm used on actual PHENIX data to quantify the momentum mismatch. The resulting $K_{e3}$ background contribution is found to be about 5% of the total cocktail at $p_T = 0.5$ GeV/c, and quickly decreases to less than 1% for $p_T > 1.2$ GeV/c. A generous systematic error of 50% is assigned to this small background contribution.

### Direct Photons

Direct photons can provide background electrons via two mechanisms:

- Real direct photons that undergo external conversions in material.
- Virtual direct photons that internally convert and manifest as an $e^+e^-$ pair.

The relationship between real and virtual direct photons is naturally the same as that between the photons from the pion decay $\pi^0 \rightarrow \gamma\gamma$ and the electron pair produced in the pion Dalitz decay $\pi^0 \rightarrow \gamma e^+ e^-$. We can use this fact to tune the decay generator to provide the contributions from both real and virtual direct photons.

PHENIX has measured the $p_T$ spectrum of direct photons in $p+p$ collisions [43] over the momentum range that is relevant to this measurement. Additional measurements in Au+Au show that the direct photon nuclear modification factor $R_{AA}$ is consistent with unity at $p_T > 6$GeV/c [44], which is where the direct photon contribution becomes a significant source of background.

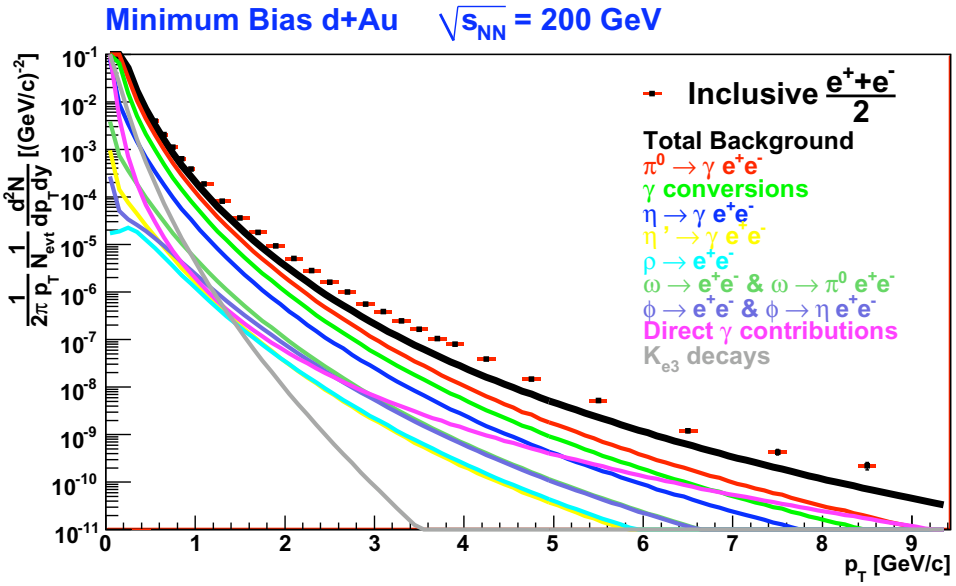


Figure 4.4: The Minimum Bias cocktail.

Therefore scaling the direct photon yield found in $p+p$ by $< N_{coll} >$ is a good approximation of the yield in $d$+Au.

By modifying the kinematics of the neutral pion in the decay simulation, we produce an artificial particle called a *directpion* ($\pi^{direct}$). Photons from the decay $\pi^{direct} \rightarrow \gamma\gamma$ have a $p_T$ spectrum that matches the measured direct photon yield in $p+p$ collisions. The electrons from the Dalitz decay of the $\pi^{direct}$ are used to represent the contribution from internal conversions of virtual direct photons in the cocktail. An important factor that must be correctly taken into account is the ratio between virtual and real direct photons, which is represented by the relative branching ratio between the Dalitz and $2\gamma$ decay modes for the $\pi^{direct}$. In the system of light neutral mesons, the relative branching ratio for Dalitz decays to $2\gamma$ is observed to increase with parent mass. A similar effect occurs for direct photons, only it is the photon $p_T$ that provides the increased phase space for Dalitz decay rather than mass. To reflect this, a logarithmic increase of the $\pi^{direct}$ relative Dalitz branching ratio with $p_T$ is included in the decay generator. Electrons from external conversions of real direct photons are estimated by the same method used for conversions from pion decays; by scaling the Dalitz decay contribution (which represents the virtual photon contribution) by an appropriate factor.

The resulting cocktails are shown below for each centrality. The data points representing the inclusive electron spectrum are included for reference.

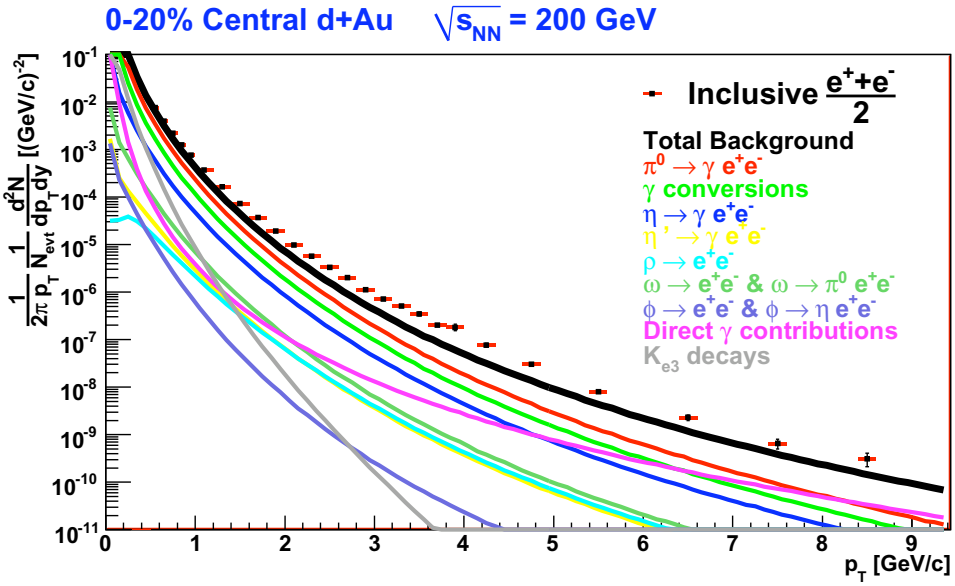


Figure 4.5: The cocktail for 0-20% centrality.

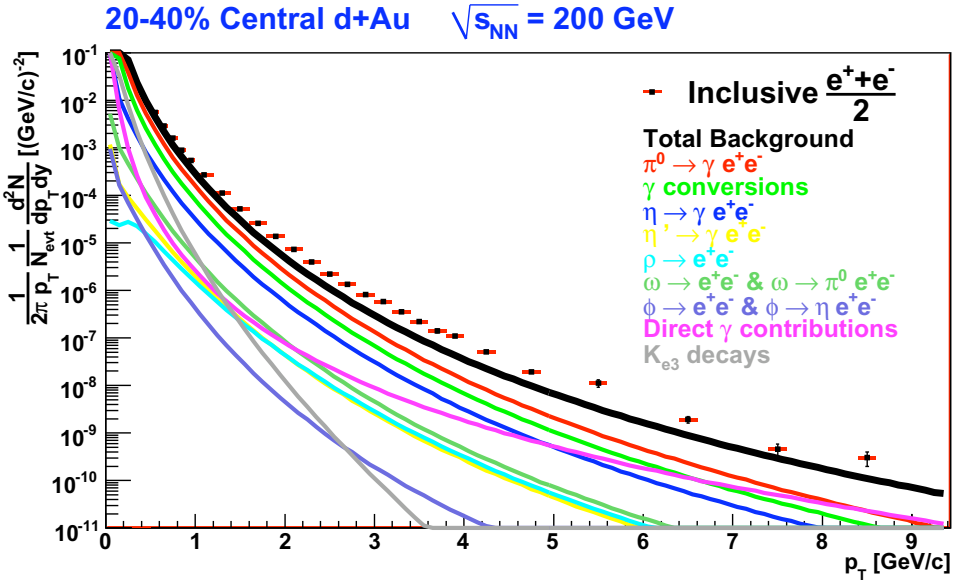


Figure 4.6: The cocktail for 20-40% centrality.

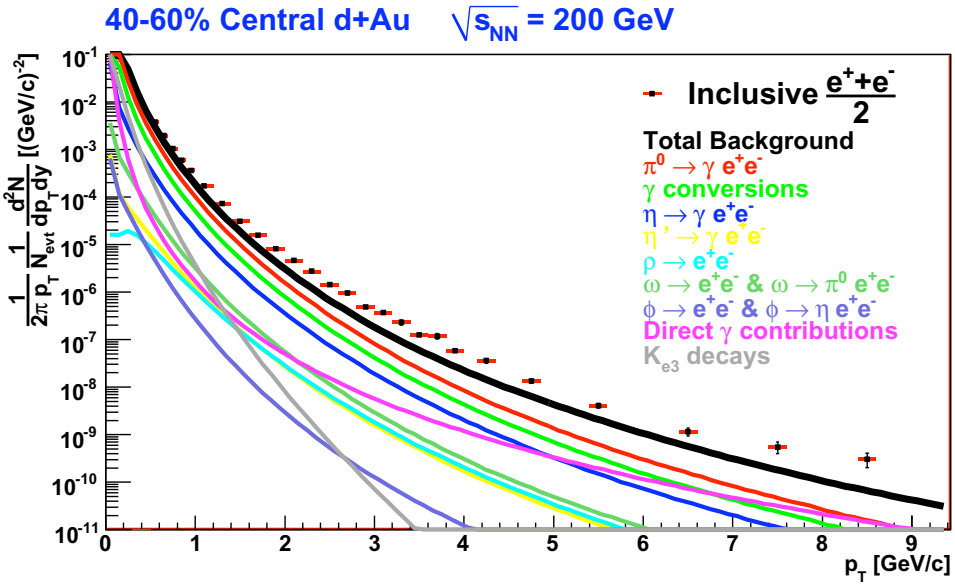


Figure 4.7: The cocktail for 40-60% centrality.

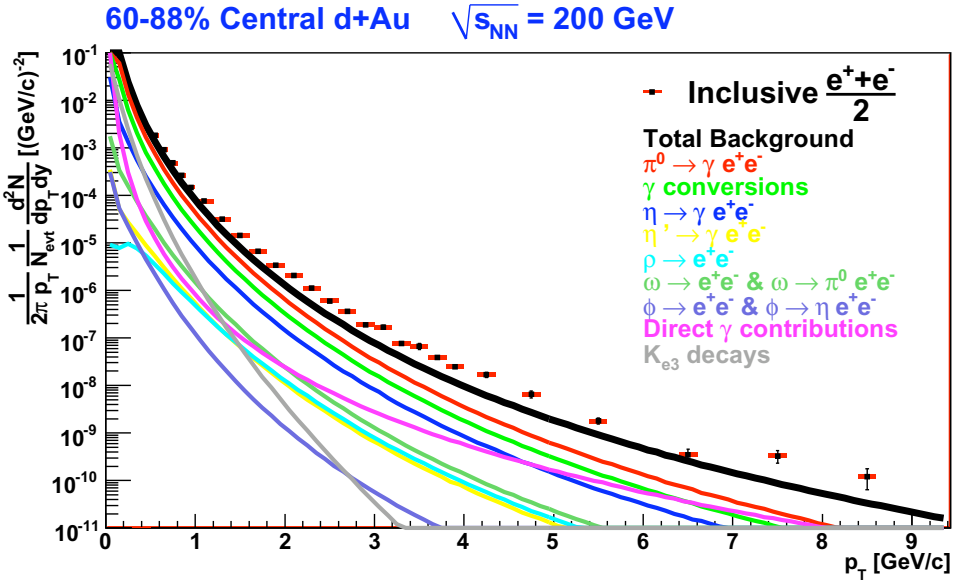


Figure 4.8: The cocktail for 60-88% centrality.

### 4.1.2 Systematic Uncertainties on the Cocktail Method

Each parent source of background in the cocktail has its own systematic uncertainty, which must be propagated through to the daughter electrons to find the uncertainty on the background subtraction from that component. The systematic uncertainties from each source are then added in quadrature to find the total systematic uncertainty on the cocktail.

#### Systematic Uncertainties on the Light Meson Contribution

The uncertainty on the neutral pion yield in $d$+Au is the dominant systematic error source out to about 5 GeV/c. The upper and lower bounds of pion parent spectra are found by raising and lowering each data point by its systematic error and re-fitting with the Hagedorn function (Eq. 4.1). These new upper and lower parent parametrizations are then put into the decay generator, and a full spectrum of decay electrons is found from each.

The other light mesons are increased and decreased by the systematic error on the ratio of meson/$\pi^0$ given in Tab. 4.2.

| Centrality | $c$ [(GeV/c)$^{-2}$] | $a$ [(GeV/c)$^{-1}$] | $b$ [(GeV/c)$^{-2}$] | $p_0$ [GeV/c] | $n$ |
|---|---|---|---|---|---|
| Min. Bias | 40.5304 | 0.33879 | 0.104251 | 0.763096 | 8.26278 |
| 0-20% | 61.2482 | 0.320761 | 0.112933 | 0.794931 | 8.36895 |
| 20-40% | 47.621 | 0.334669 | 0.0983569 | 0.775913 | 8.2866 |
| 40-60% | 36.3198 | 0.370399 | 0.0900298 | 0.743658 | 8.18208 |
| 60-88% | 23.0506 | 0.386472 | 0.0870125 | 0.697095 | 8.09066 |

Table 4.3: Fit parameters for the Hagedorn function used to represent the upper bound of the pion spectrum in the Monte Carlo decay generator, in order to determine upper systematic uncertainty band on the cocktail.

## 4.2 Converter Method

This alternative method recognizes the fact that the overwhelming majority of the background electrons are photonic in nature, that is, they originate from photons (either virtual photons, as in the Dalitz decay, or real photons, through conversions). The total amount of background from these sources is very sensitive to the amount of material in the PHENIX aperture. Signal electrons, on the other hand, come from the decays of heavy mesons containing

| Centrality | $c$ [(GeV/c)$^{-2}$] | $a$ [(GeV/c)$^{-1}$] | $b$ [(GeV/c)$^{-2}$] | $p_0$ [GeV/c] | $n$ |
|---|---|---|---|---|---|
| Min. Bias | 31.9947 | 0.299315 | 0.0898609 | 0.796117 | 8.39792 |
| 0-20% | 47.9081 | 0.293105 | 0.0977806 | 0.823563 | 8.47653 |
| 20-40% | 37.024 | 0.289036 | 0.0778028 | 0.82465 | 8.48922 |
| 40-60% | 29.0612 | 0.313897 | 0.0769892 | 0.784152 | 8.36424 |
| 60-88% | 18.8503 | 0.332555 | 0.0842593 | 0.719205 | 8.19205 |

Table 4.4: Fit parameters for the Hagedorn function used to represent the lower bound of the pion spectrum in the Monte Carlo decay generator, in order to determine lower systematic uncertainty band on the cocktail.

charm and bottom quarks, and are only generated in the primary interaction. The amount of material in PHENIX does not affect the rate of signal electrons. One can take advantage of this basic difference to precisely measure the amount of background electrons simply by changing the amount of conversion material present in PHENIX. Although limited by statistics, this alternative method provides an independent measurement of the heavy flavor electron spectrum.

By dividing the yield of electrons in a given $p_T$ bin into photonic ($N^{\gamma}$) and non-photonic ($N^{non-\gamma}$) contributions, the total electron yield measured in the standard PHENIX configuration can be expressed as

$$N^{conv-out} = N^{\gamma} + N^{non-\gamma} \tag{4.4}$$

For one day during Run-8 (about 3% of the total events analyzed), a 0.0254 cm thick brass sheet was wrapped around the beam pipe. The effect of this converter is to increase the photonic contribution by a factor $R_{\gamma}$. Due to the additional mass of the converter, the non-photonic electrons are attenuated by a small fraction $\epsilon$. Thus the total yield of electrons measured with the converter installed is given by

$$N^{conv-in} = R_{\gamma}N^{\gamma} + (1-\epsilon)N^{non-\gamma} \tag{4.5}$$

The quantity of interest here is $N^{non-\gamma}$. The above equations can be rearranged to give

$$N^{non-\gamma} = \frac{R_{\gamma}N^{conv-out} - N^{conv-in}}{R_{\gamma} - 1 + \epsilon} \tag{4.6}$$

$$N^{\gamma} = \frac{N^{conv-in} - (1-\epsilon)N^{conv-out}}{R_{\gamma} - 1 + \epsilon} \tag{4.7}$$

The quantities $N^{\gamma}$ and $N^{non-\gamma}$ are the unknowns in the above system of

equations. The measured quantities are the inclusive electron yields with and without the converter, denoted by $N^{conv-in}$ and $N^{conv-out}$, respectively. The factors $\epsilon$ and $R_\gamma$ must then be determined by simulation in order to be able to simultaneously solve the equations.

It is worth noting at this point that not all background is photonic in nature. Specifically, electrons from the decays $\rho \to e^+e^-$, $\omega \to e^+e^-$, and $\phi \to e^+e^-$ are not photonic and will not be correctly estimated with the converter method. Similarly, misreconstructed electrons from $K_{e3}$ decays are also non-photonic background. These small contributions are subtracted using the cocktail method described above.

Before turning to the rigorous determination of $R_\gamma$, it is instructive to study $R_{CN}$, which is simply the ratio of the inclusive yield of electrons with and without the converter installed (these spectra are shown in Fig. 4.9). From Eqns. 4.4 and 4.5, we see that this ratio can be expressed in terms of the non-photonic and photonic contributions as

$$R_{CN} = \frac{N^{conv-in}}{N^{conv-out}} = \frac{R_\gamma N^\gamma + (1-\epsilon)N^{non-\gamma}}{N^\gamma + N^{non-\gamma}} \ . \tag{4.8}$$

Note that in the absence of a non-photonic signal ($N^{non-\gamma} = 0$), the equation reduces to $R_{CN} = R^\gamma$. At the lowest $p_T$, where the signal to background ratio is much less than one, the value of $R_{CN}$ gives a decent first estimate of $R^\gamma$. From Fig. 4.10, we see that $R_\gamma$ should be slightly higher than 2. Although limited by the relatively poor statistics of the converter run, the decrease in the value of $R_{CN}$ with increasing $p_T$ is evidence of the emergence of a non-photonic signal.

### 4.2.1 Converter Simulation

A full simulation of the PHENIX detector with and without the converter installed is used to determine the factors $\epsilon$ and $R^\gamma$ that are necessary to solve Eqns. 4.6 and 4.7. First, we determine the fraction of non-photonic electrons that are lost due to the presence of the converter, $\epsilon$. Since the thickness of the brass converter sheet is precisely known, it can be realistically modeled in the GEANT simulation of the PHENIX detector. By studying the attenuation of electrons generated at the collision vertex from $\pi^0$ Dalitz decays, the magnitude of this blocking effect was determined to be $\epsilon = 0.021$, with a systematic error of 25%.

As discussed above, the majority of the photonic background is from the neutral pion, with the $\eta$ meson contributing about 10% of the total. Since the branching ratios of each meson to photons and Dalitz decays is different, the

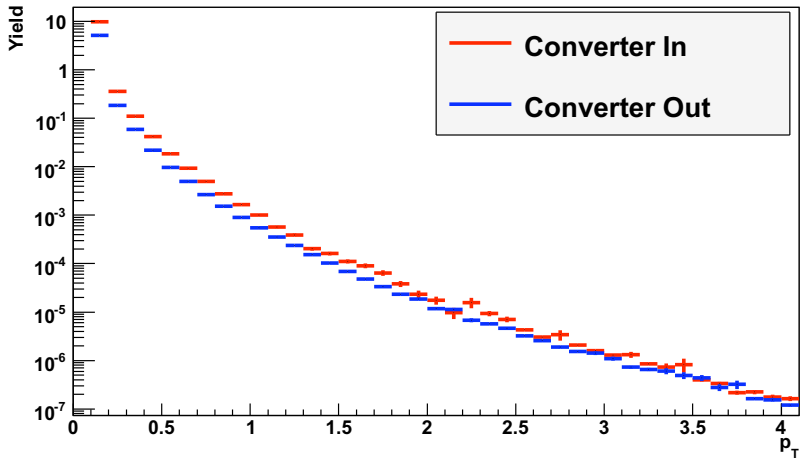


Figure 4.9: Measured inclusive electron spectra with and without the converter installed. Only statistical errors are shown.

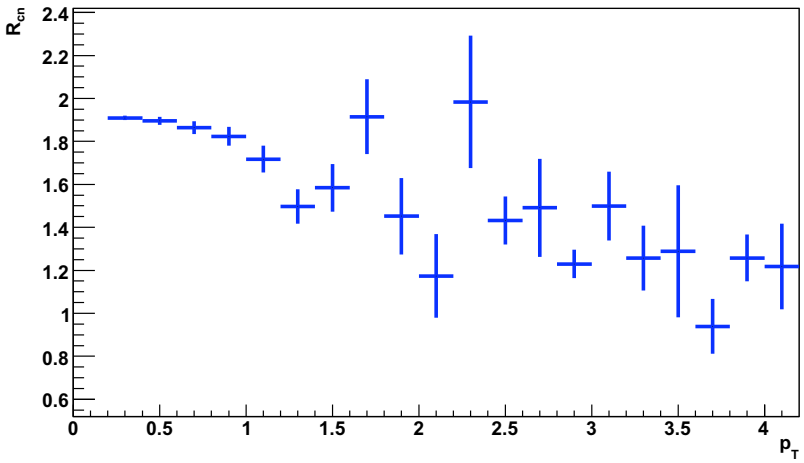


Figure 4.10: Ratio of the two spectra, $R_{CN}$. The decrease with increasing electron $p_T$ indicates the presence of a non-photonic component.

presence of the converter will affect each meson's contributions to the photonic electron spectrum differently. Recognizing this fact, the factors $R_\gamma^{\pi^0}$ and $R_\gamma^\eta$ are calculated separately for each species, then combined via a weighted average to find the total $R_\gamma$. Other mesons have a negligibly small contribution.

To determine $R_\gamma^{\pi^0}$, we study the effect of the converter on the photonic electron yield from neutral pion decays. Ten million neutral pions are decayed by the decay generator and passed through the GEANT simulation of the PHENIX detector with and without the converter (Fig. 4.11). Since all electron tracks which pass the selection criteria from this source are photonic in nature, the ratio of the $p_T$ spectra with and without the converter installed gives the factor $R_\gamma^{\pi^0}$ (see Fig. 4.12).

The method for obtaining the factor $R_\gamma^\eta$ is identical to the method for finding $R_\gamma^{\pi^0}$, except the input spectra come from simulated $\eta$ meson decays rather than $\pi^0$. The $\eta$ parent parametrization comes from $m_T$-scaling the Hagedorn fit to the minimum bias pion data. The resulting spectra of simulated electrons with and without the converter are shown in Fig. 4.13. Note that the value of $R_\gamma^\eta$ is slightly smaller than $R_\gamma^{\pi^0}$. This is due to the higher eta relative branching ratio of Dalitz decay/2 photon decay. For a given number of particles, the pion decays will produce on average more photons, and thus will be affected more by the presence of the converter, giving a larger $R_\gamma^{\pi^0}$.

Now that the seperate effects on the $\pi^0$ and $\eta$ mesons are known, they can be combined to find the total factor $R_\gamma$. An average of $R_\gamma^{\pi^0}$ and $R_\gamma^\eta$, weighted by the number of electrons from each source, gives the desired factor:

$$R_\gamma = \frac{R_\gamma^\pi N_e^\pi + R_\gamma^\eta N_e^\eta}{N_e^{\pi^0} + N_e^\eta} = \frac{R_\gamma^\pi + R_\gamma^\eta \frac{N_e^\eta}{N_e^\pi}}{1 + \frac{N_e^\eta}{N_e^\pi}} \tag{4.9}$$

The weighting factor $\frac{N_e^\eta}{N_e^\pi}$ is found by comparing the spectra of electrons from $\eta$ and $\pi^0$ decays, as determined by the Monte Carlo decay generator. The ratio (shown in Fig. 4.15) is fit with the curve

$$y = 0.278 - \frac{0.087}{\sqrt{p_T}} \tag{4.10}$$

The final combined value of $R_\gamma$ is found to be 2.32 by fitting a constant to the histogram determined from Eq. 4.9. Note that this agrees well with the approximate value of $R_\gamma$ that we expected from the first look at $R_{CN}$. We now have all the necessary information to simultaneously solve Eqns. 4.6 and 4.7 and extract the non-photonic electron spectrum.

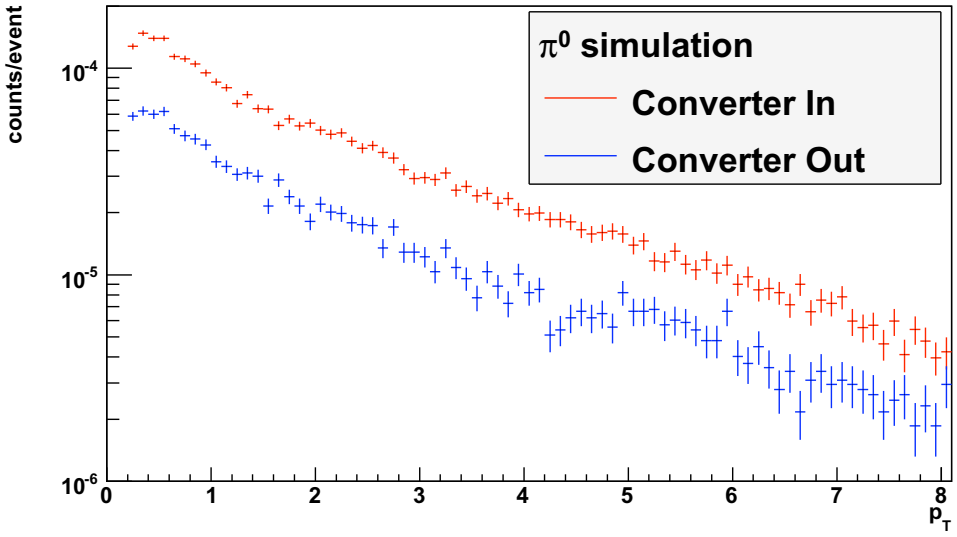


Figure 4.11: Simulated electron spectra from $\pi^0$ decays, with and without the converter installed.

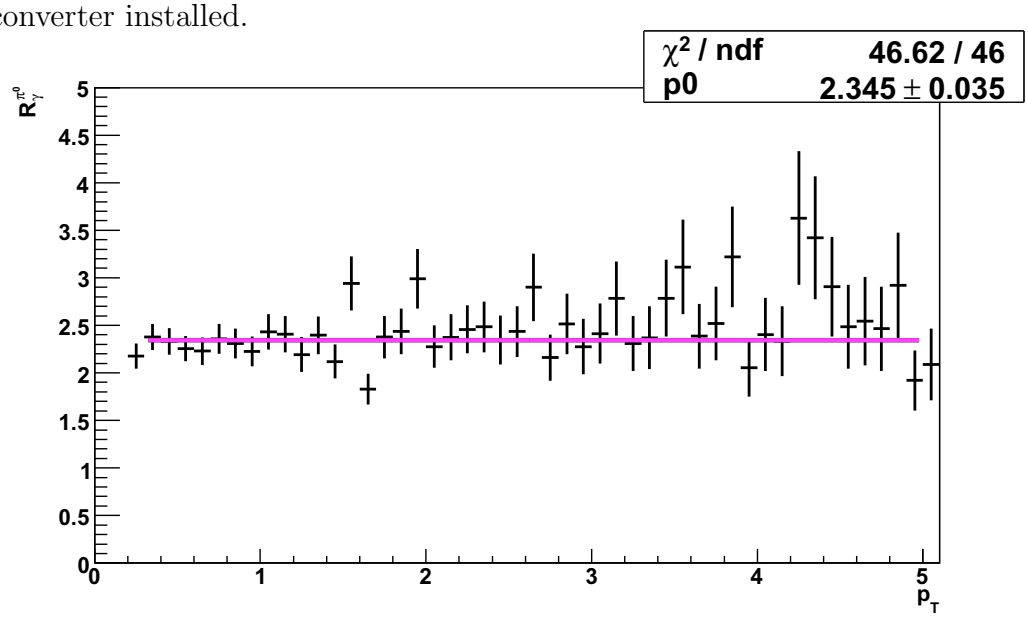


Figure 4.12: The ratio of the simulated electron spectra. A fit to this ratio gives the factor $R_\gamma^{\pi^0}$.

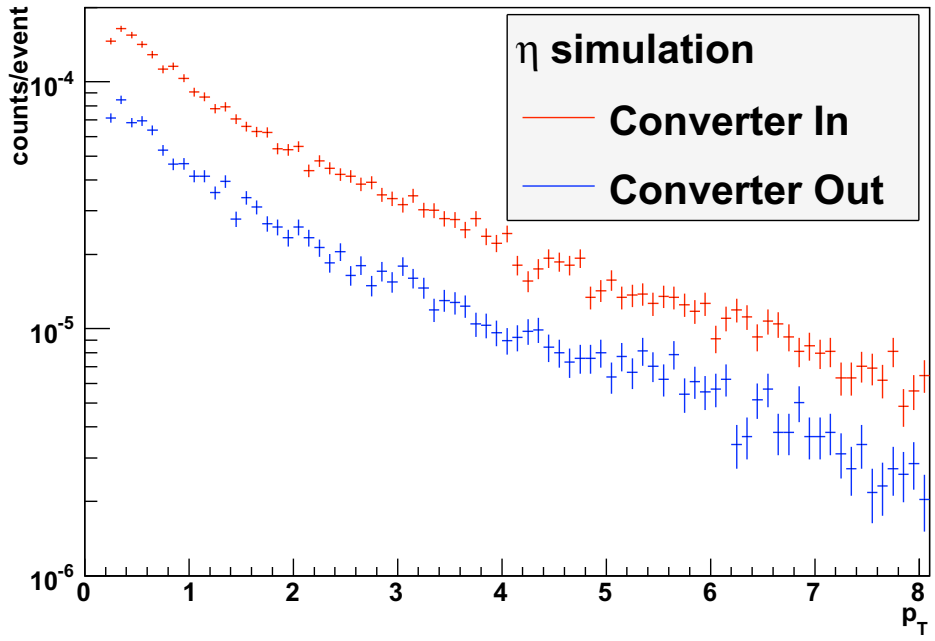


Figure 4.13: Simulated electron spectra from $\eta$ decays, with and without the converter installed.

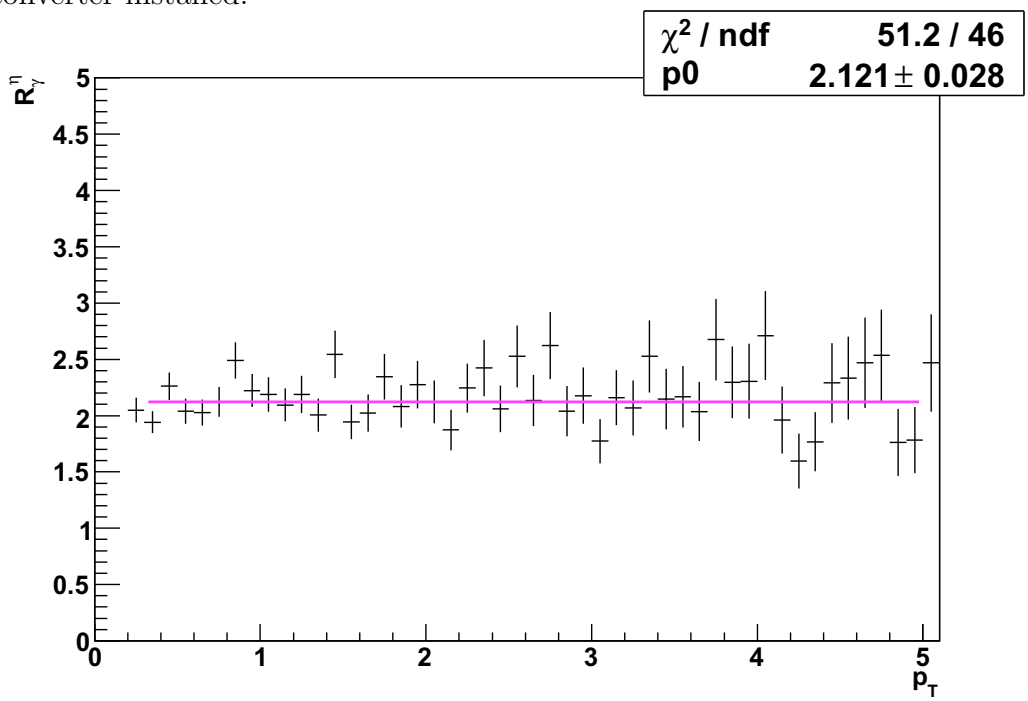


Figure 4.14: The ratio of the simulated electron spectra. A fit to this ratio gives the factor $R_\gamma^\eta$.

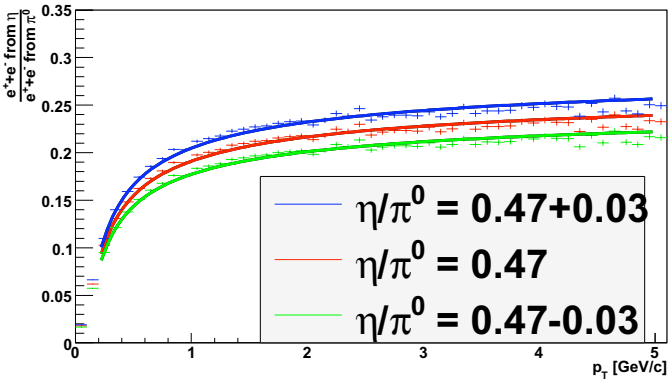


Figure 4.15: The ratio of electrons from $\eta$ decays and conversions to those from $\pi^0$ decays and conversions. The three curves correspond to the range of the $\eta/\pi^0$ ratio given in Tab. 4.2.

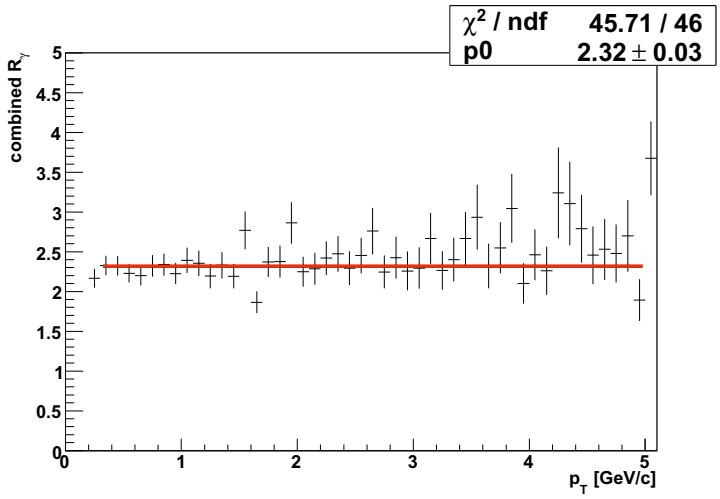


Figure 4.16: The combined $R_\gamma$.

### 4.2.2 Systematic Uncertainties from the Converter Method

The systematic uncertainties on the heavy flavor electron spectrum determined with this method can be broken into three broad categories:

- Systematic uncertainty on the fully corrected inclusive electron yield. The evalution of this uncertainty has been described in Sec. 3.6.
- Uncertainty on the non-photonic background subtraction. This was described in Sec. 4.1.2.
- The systematic uncertainties on the extraction of the non-photonic electron spectrum as determined with the converter subtraction, given by Eq. 4.6.

Since each of these sources of uncertainty are independent, they are determined separately and combined in quadrature to give the total systematic uncertainty. Here we will only discuss the third category, as the other have been explained previously.

The converter subtraction method relies heavily on the fact that the simulation accurately describes the material present on the PHENIX detector. To determine the difference, we examine the number of electron pairs measured with and without the converter in simulation and data, from an input sample of $\pi^0$ decays. Figure 4.17 shows electron pairs as a function of pair invariant mass after mixed event combinatorial background subtraction, with (red) and without (blue) the converter for Run-4 data and simulation. Since Run-8 used the same converter material and simulated converter parametrization, all the Run-4 results will apply here. Electrons from conversions in the beam pipe and converter are wrongly assumed by the PHENIX tracking algorithm to come from the event vertex. Their tracks are mis-reconstructed with an erroneous $p_T$ and thus the pairs have a non-zero invariant mass, which is determined by the radial position of the conversion point. Since the pair mass gives us a way to identify conversions, we can compare the number of conversions generated in the converter in simulation and data to get an idea of the uncertainty of the converter thickness, and thus the uncertainty on the calculation of $R_\gamma$.

Pairs measured at $M_{e^+e^-} < 10$ MeV/$c^2$ are dominantly the electrons from $\pi^0$ Dalitz decays. The mass region $10 < M_{e^+e^-} < 35$ MeV/$c^2$ contains a large sample of photon conversions in the beam pipe. This peak is clearly enhanced with the addition of the converter (which will cause an increase in the same mass region, since it is wrapped closely around the beampipe). We define the factor $R_\gamma^{pair}$ as

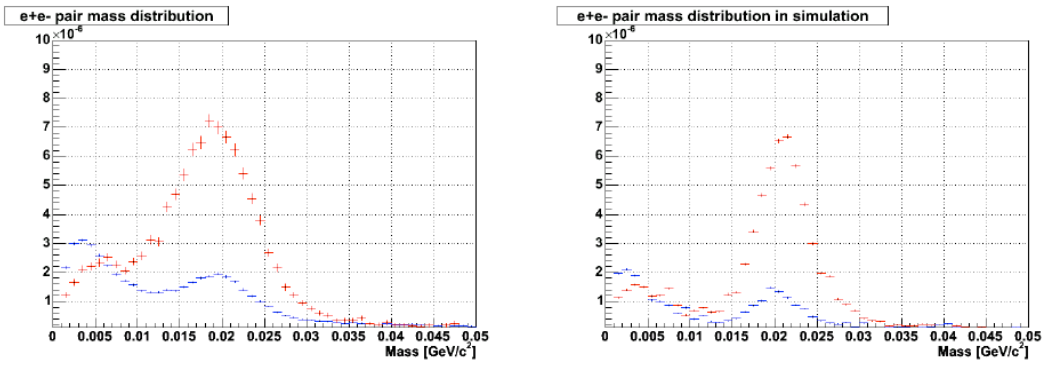


Figure 4.17: Measured (left) and simulated (right) electron pair yields from PHENIX Run-4 [58].

$$R_\gamma^{pair} = \frac{N_{pair}^{conv-in}}{N_{pair}^{conv-out}} \tag{4.11}$$

where $N_{pair}^{conv-in}$ is the number of $e^+e-$ pairs with mass $M_{e^+e-} < 35$ MeV/$c^2$ and a pair $p_T$ between 0.5 and 5 GeV/$c$, with the converter in. The double ratio $[R_\gamma^{pair}]_{data}/[R_\gamma^{pair}]_{simulation}$ gives an agreement of $0.999 \pm 0.027$, so we take 2.7% as the systematic uncertainty on the amount of material.

Additional uncertainty arises due to the difference in detector live area during the converter run (which gives us the quantity $N^{conv-in}$) and the non-converter run. This difference is estimated by the same method we used to determine the geometrical difference between the data and the simulation for the acceptance × efficiency correction (see Sec. 3.6). The $\phi$ distribution in one arm of the spectrometer is normalized to have the same integral for the converter and non-converter runs. This same normalization is then applied to the other arm. The difference in the integrated $\phi$ distribution of this second arm for the converter and non-converter data is 2.2%, which we take as a systematic uncertainty on the quantity $N^{conv-in}$.

The final source of systematic uncertainty is from the calculation of the blocking factor $\epsilon$.

The contribution from each uncertainty to the total non-photonic electron yield is found by modifying that quantity in Eq. 4.6. For example, the uncertainty in the non-photonic electron yield due to the uncertainty on $R_\gamma$ is found by calculating

$$N^{non-\gamma} = \frac{(R_\gamma \pm \delta)N^{conv-out} - N^{conv-in}}{(R_\gamma \pm \delta) - 1 + \epsilon} \tag{4.12}$$

where $\delta = 2.7\%$. The differences in the non-photonic electron yield by changing each parameter independently are added in quadrature. The upper and lower values are averaged to give the total systematic uncertainty on the converter extraction. This systematic uncertainty is the added in quadrature with the systematic uncertainty on the inclusive electron yield and the non-photonic background subtraction to obtain the total systematic uncertainty on the heavy flavor electron yield.

## 4.3 Comparing the Two Methods

A crucial cross-check of this measurement's accuracy is the consistency of the two methods. Each has their own strengths and drawbacks. The cocktail method of background subtraction is not limited by statistics, but relies on previous results (the pion measurement from the relatively low-statistics Run-3) and the assumption that the heavier mesons follow $m_T-$scaling. The converter method provides an empirical determination of the background, but is limited by the low statistics of the converter run.

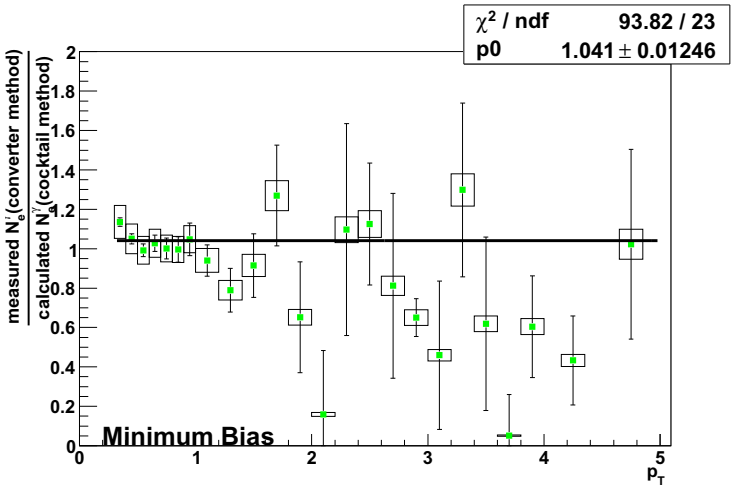


Figure 4.18: The ratio of the photonic background determined with the converter method to the background calculated using the cocktail method, for Minimum Bias collisions. The systematic error boxes are from the cocktail only.

Fig. 4.18 shows the ratio of the photonic backgrounds determined by the converter and cocktail methods. Although limited by statistics at high momentum, the converter sample gives a good measurement of the photonic background at low $p_T$. Since the converter method provides a measurement of the

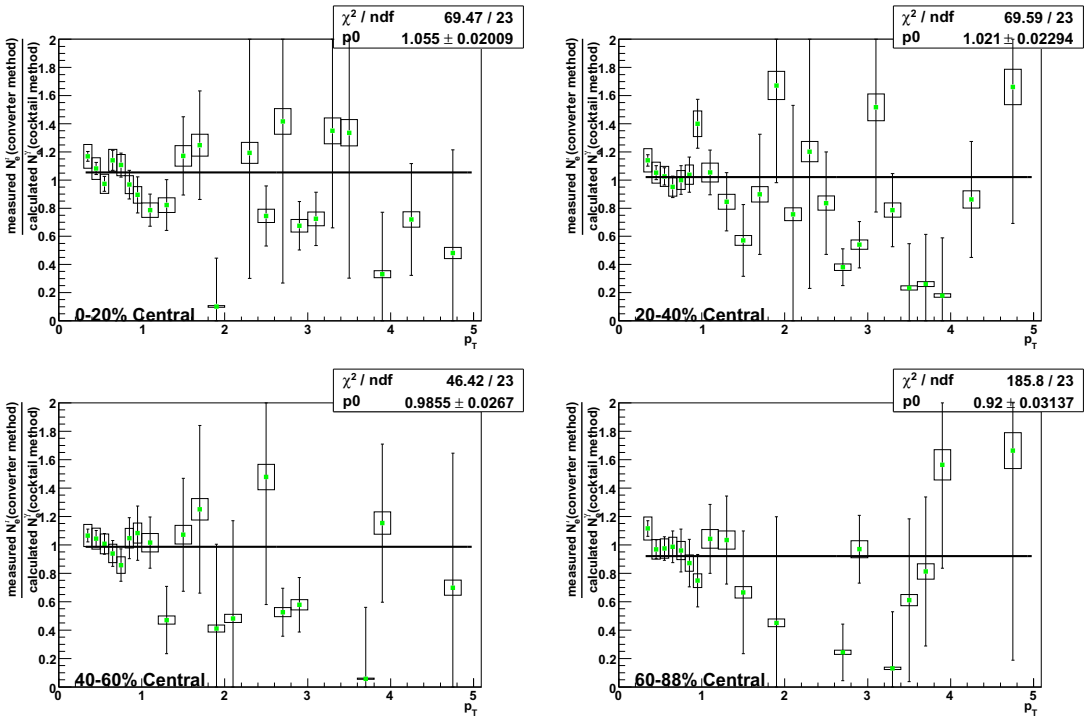


Figure 4.19: The ratio of the photonic background determined with the converter method to the background calculated using the cocktail method, divided by centrality. The systematic error boxes are from the cocktail only.

photonic background, while the cocktail method is a calculation of the same quantity, the cocktail is scaled to match the converter data. For each centrality (see Fig. 4.19), the difference is less than 10%, well within systematic uncertanties. The remarkable consistency of these two independent methods inspires great confidence in the veracity of the results.

# Chapter 5

# Results and Discussion

Figure 5.1 shows the spectrum of electrons from heavy flavor for each centrality category. The heavy flavor electron yield determined by the converter method at $p_T < 1.3\text{GeV}/c$, and by the cocktail method (with photonic components scaled to match the converter data) at higher momentum. The statistical uncertainties are shown as bars around the central values, while the systematic uncertainties are displayed as boxes. The boxes contain the uncertainties in the solid angle correction, electron identification efficiency, and trigger bias correction. Added in quadrature with those are the systematic uncertainties on the non-photonic electron extraction (from Eqn. 4.6), or the uncertainty from the cocktail subtraction, depending on the method used to determine the yield. The lines are a fit the the $p+p$ heavy flavor electron spectrum [21], scaled by $< N_{coll} >$ for each centrality.

The $d$+Au electron spectra can be compared to the $p+p$ reference data by computing the nuclear modification factor $R_{dA}$, given by

$$R_{dA} = \frac{dN^e_{dA}/dp_T}{< N_{coll} > \times dN^e_{pp}/dp_T} \tag{5.1}$$

for each centrality. The factor $R_{dA}$ is shown as a function of $p_T$ for the various centrality bins below. As in Fig. 5.1, the statistical (systematic) uncertainties are represented by bars (boxes). For points at $p_T < 1.6\text{GeV}/c$, the nuclear modification factor is found by dividing the $d$+Au yield by the $< N_{coll} >$-scaled $p+p$ yield point by point. At higher transverse momentum, where the $p+p$ heavy flavor electron spectrum is consistent with the shape determined from pQCD, a fit is used to represent the $p+p$ yield. The statisical error on the fit is included as a systematic error on $R_{dA}$. The global scaling error from the uncertainty in $< N_{coll} >$ and the total sampled $p+p$ luminosity is given by a box on the right.

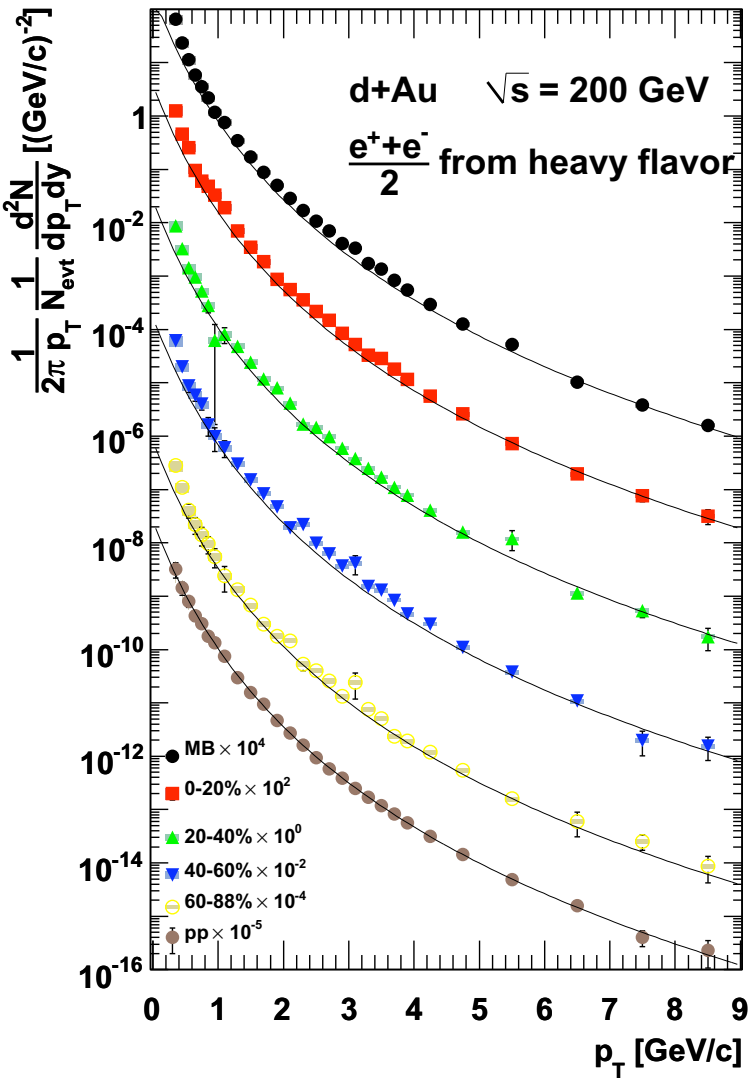


Figure 5.1: Electrons from heavy flavor decays, separated by centrality. The lines represent a fit to the $p+p$ result [21], scaled by $N_{coll}$.

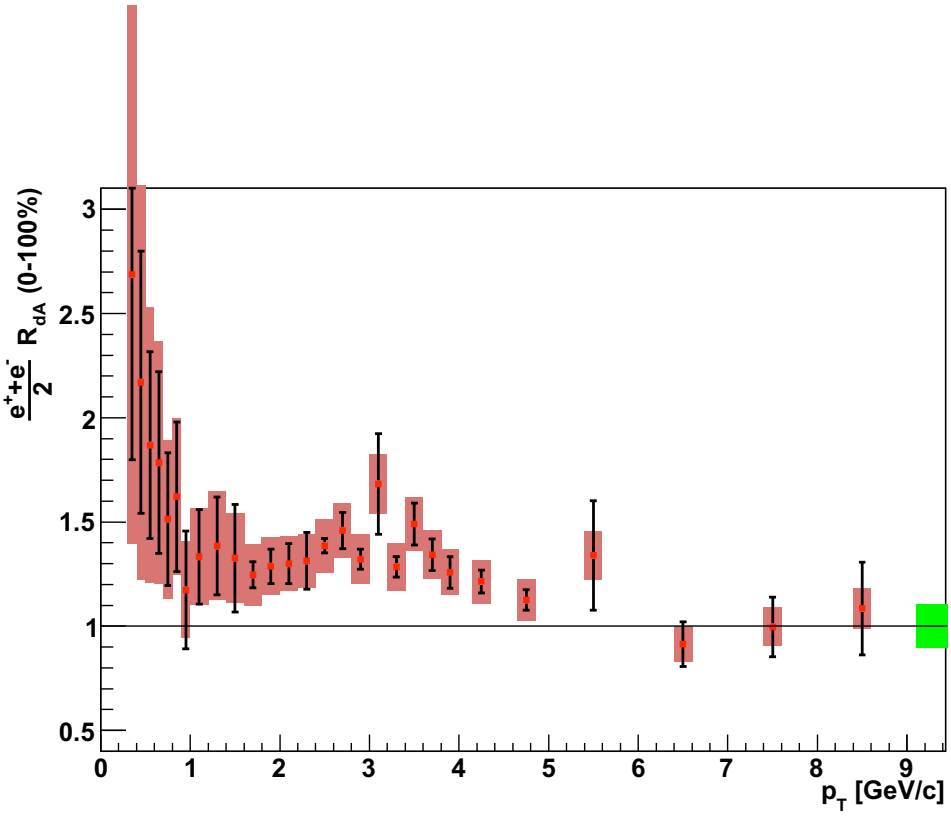


Figure 5.2: The nuclear modification factor for unbiased collisions.

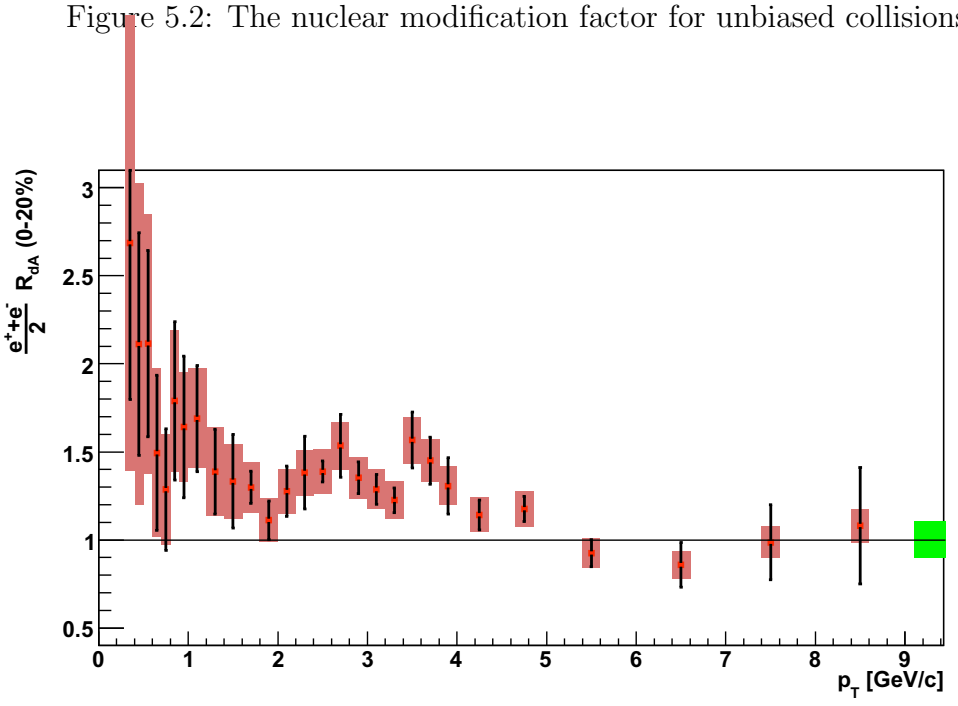


Figure 5.3: The nuclear modification factor for central collisions.

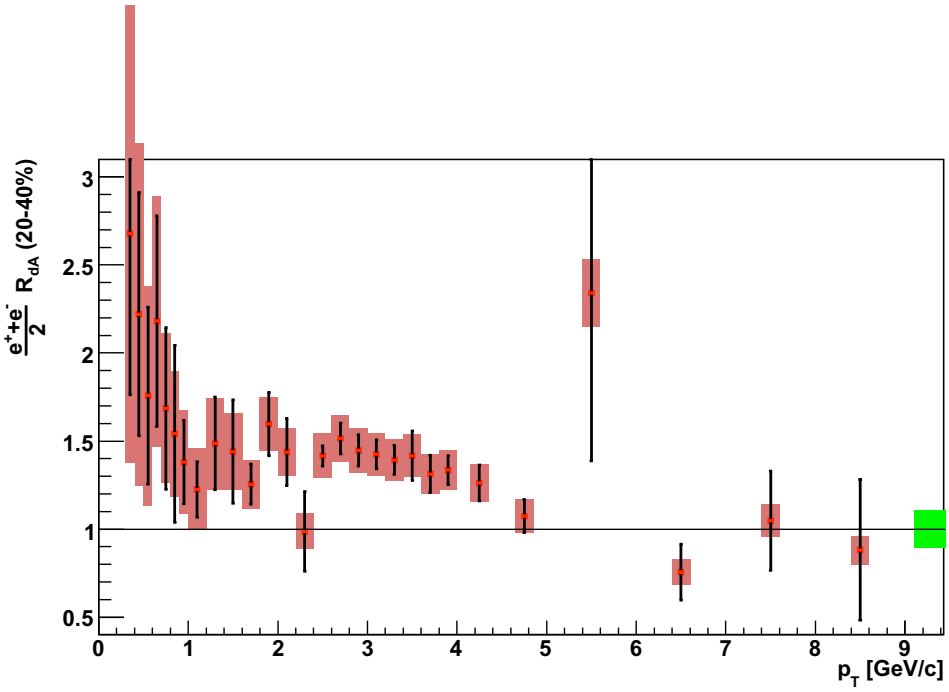


Figure 5.4: The nuclear modification factor for semi-central collisions.

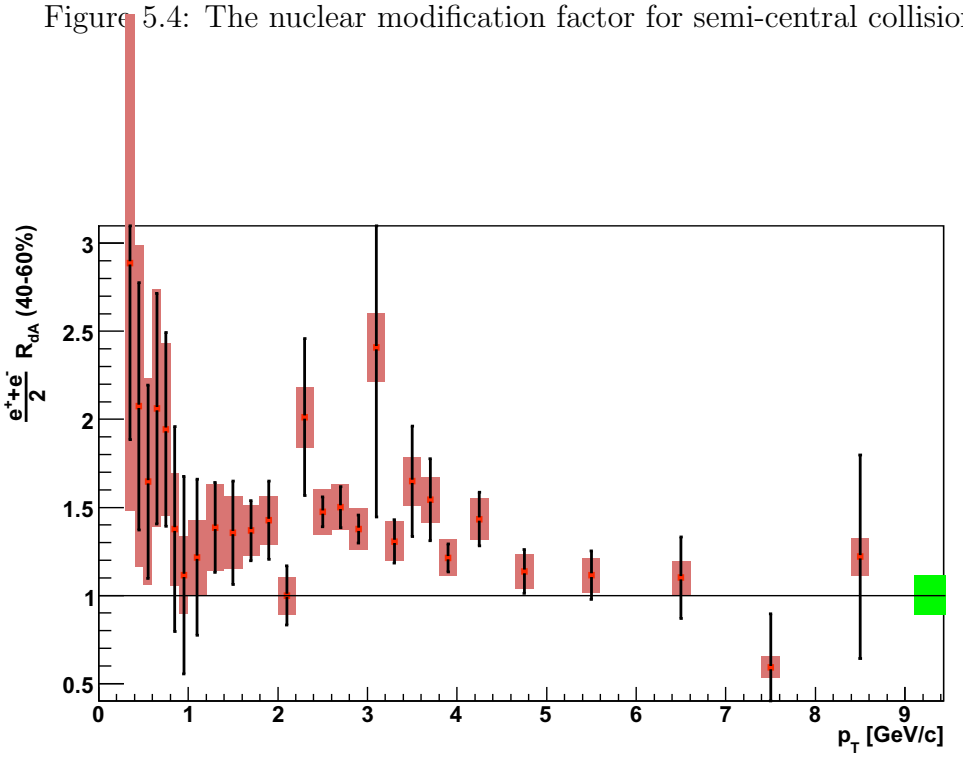


Figure 5.5: The nuclear modification factor for semi-peripheral collisions.

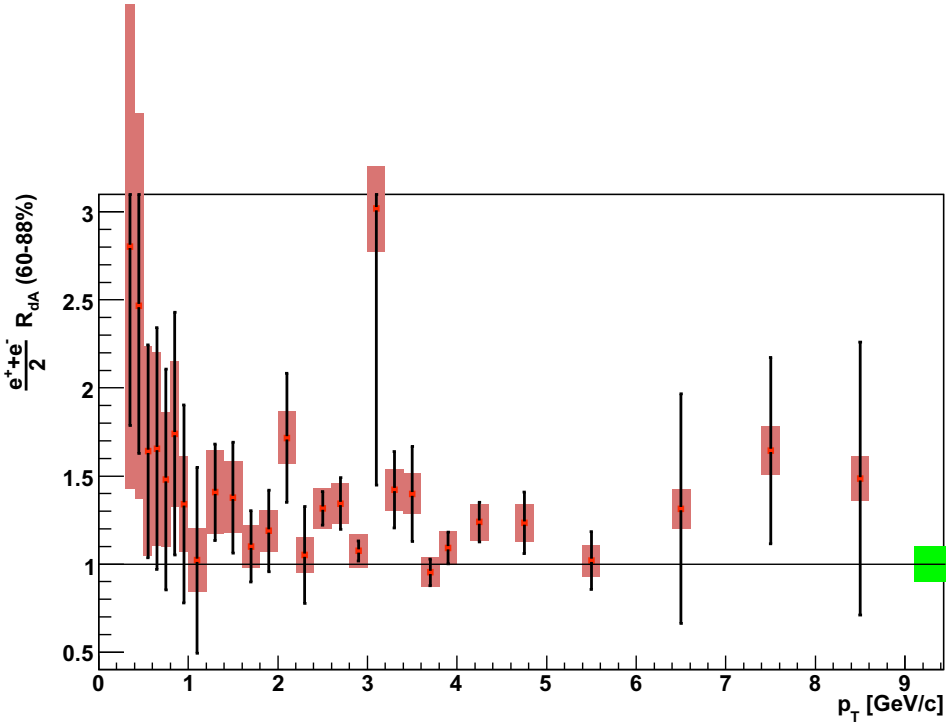


Figure 5.6: The nuclear modification factor for peripheral collisions.

A clear enhancement of the heavy flavor electron signal is seen in $d$+Au collisions, out to a $p_T$ of about 5 GeV/$c$. Some enhancement is present in peripheral collisions, with the effect increasing for more central collisions. Above 5 GeV/$c$, electrons from the decays of mesons containing bottom quarks begins to dominate, suggesting that the large electron enhancement is due primarily to charm. This measurement is similar to the predictions of charm and bottom production based on gluon saturation models [40], although the observed enhancement here is higher than predicted (see Fig. 1.13). This possibly suggests that the enhancement is due to a combination of gluon saturation effects and a parton scattering based Cronin enhancement of $D$ mesons.

The enhancement seen here seems to rule out a suppressed charm production mechanism as the explanation for $J/\psi$ suppression in $d$+Au collisions [36]. The suppression may be due to a final state effect, such as break-up of bound $c\bar{c}$ pairs in the cold nuclear medium.

The large enhancement observed in $d$+Au should also be present in Au+Au collisions, however, energy loss by charm quarks in the medium makes this enhancement difficult to observe experimentally. Looking back at Fig. 1.6, we see that the heavy flavor electron $R_{AA}$ is different from the $\pi^0$ $R_{AA}$ in exactly the transverse momentum region where this large enhancement is observed. Where the cold nuclear matter effects are small ($p_T > 5$ GeV/$c$), the heavy flavor electron and $\pi^0$ have very similar values of $R_{AA}$. If we take the heavy flavor electrons to represent heavy quarks, and the $\pi^0$ to represent light quarks,

this suggests that the difference in $R_{AA}$ is due only to cold nuclear matter effects, rather than different magnitudes of energy loss in the medium.

In an attempt to quantitatively account for these cold nuclear matter effects in Au+Au collisions, we present a simple model. A generic cross section for interactions not sensitive to isospin effects, such as heavy quark production, can be found by calculating

$$d\sigma(Q^2, \sqrt{s})_{pA\to a+X} = \sum_{i,j=q,\bar{q},g} f_i^p(x_1, Q^2) \otimes A f_i^A(x_2, Q^2) \otimes d\hat{\sigma}(Q^2, x_1, x_2)_{i,j\to a+X} \tag{5.2}$$

where $\hat{\sigma}(Q^2, x_1, x_2)_{i,j\to a+X}$ is the cross section for producing parton $a$ from interactions of partons carrying momentum fractions $x_1$ and $x_2$, and $Q^2 >> \Lambda^2_{QCD}$. The parton distribution functions (PDFs) of the proton and nucleus with mass number $A$ are given by $f_i^p(x_1, Q^2)$ and $f_i^A(x_2, Q^2)$. The initial state effects of the nucleus on heavy quark production are contained within the modified nuclear PDF.

Following the cross section given above, the number of heavy quarks produced in a $d$+Au collision are related to a convolution of the proton PDF and the nuclear PDF:

$$N_Q^{dA} \sim f_i^p \otimes A \cdot f_i^A \tag{5.3}$$

Similarly, the quark production in $p+p$ collisions are related to the proton PDF:

$$N_Q^{pp} \sim f_i^p \otimes f_i^p \tag{5.4}$$

and in A+A,

$$N_Q^{AA} \sim A^2 \cdot f_i^A \otimes f_i^A \tag{5.5}$$

In this simple model, we assume all initial state effects are contained within the quantities $N_Q$.

The task at hand is to isolate the medium effects on heavy quarks produced in a collision of two large nuclei. At a given $p_T$, we parametrize the observed yield of heavy quarks (or, in our case, electrons from heavy quark decay) with the function

$$Y_Q^{AA} \sim M \cdot N_Q^{AA} \tag{5.6}$$

where $M$ is a factor that represents the attenuation of the produced yield $N_Q^{AA}$ in the nuclear medium that is formed in A+A collisions. The nuclear

modification factor $R_{AA}$ is thus

$$R_{AA} = \frac{Y_Q^{AA}}{< N_{coll} > \times Y_Q^{pp}} = M \cdot \frac{f_i^A \otimes f_i^A}{f_i^p \otimes f_i^p} \tag{5.7}$$

Since there is no hot medium formed in $p+p$ or $d+Au$ collisions, M = 1 for these systems. Therefore the $d$+Au nuclear modification factor is given by

$$R_{dA} = \frac{Y_Q^{dA}}{< N_{coll} > \times Y_Q^{pp}} = \frac{f_i^p \otimes f_i^A}{f_i^p \otimes f_i^p} \tag{5.8}$$

In order to isolate the medium attenuation factor $M$, we compute the ratio

$$\frac{R_{AA}}{R_{dA}^2} = \frac{\frac{Y_Q^{AA}}{<N_{coll}^{AA}>Y_Q^{pp}}}{(\frac{Y_Q^{dA}}{<N_{coll}^{dA}>Y_Q^{pp}})^2} = \frac{M \cdot \frac{f_i^A \otimes f_i^A}{f_i^p \otimes f_i^p}}{(\frac{f_i^p \otimes f_i^A}{f_i^p \otimes f_i^p})^2} \tag{5.9}$$

In this simple model, we assume that the convolutions of the parton distribution functions are perfectly factorizable, in which case the above equation reduces to

$$\frac{R_{AA}}{R_{dA}^2} = M \cdot \frac{f_i^A \otimes f_i^A}{f_i^p \otimes f_i^p} \cdot (\frac{f_i^p \otimes f_i^p}{f_i^p \otimes f_i^A})^2 = M \tag{5.10}$$

Therefore the ratio $R_{AA}/R_{dA}^2$ will, in some sense, cancel out the initial state effects involving in heavy quark production in the nucleus and isolate the effects due to the medium. In practice, this ratio is calculated with the measured yields of the heavy flavor electrons in the three systems,

$$\frac{R_{AA}}{R_{dA}^2} = \frac{(1/N_{coll}^{AA})\frac{Y^{AA}}{Y^{pp}}}{((1/N_{coll}^{dA})\frac{Y^{dA}}{Y^{pp}})^2} = \frac{(N_{coll}^{dA})^2}{N_{coll}^{AA}} \times \frac{Y^{AA}Y^{pp}}{(Y^{dA})^2} \tag{5.11}$$

The top panel of Fig. 5.7 shows the nuclear modification factors $R_{dA}$ and $R_{AA}$ for electron from heavy flavor decays, for minimum bias collisions. The bottom panel shows the ratio $R_{AA}/R_{dA}^2$ for these electrons from heavy flavor decay, and the neutral pion. Since the $\pi^0$ nuclear modification factor $R_{dA}$ is close to one (i.e. cold nuclear matter effects are small), the division by $R_{dA}^2$ does little to modify the factor $R_{AA}$. However, with this modification, the heavy flavor electron and pion data match well within uncertainty. This simple models suggests that the difference in $R_{AA}$ between the $\pi^0$ and electrons from heavy quarks is due to cold nuclear matter effects. Taking the $\pi^0$ to represent light quarks and the heavy flavor electrons to represent heavy quarks, this suggests that level of quark suppression in the hot medium created in Au+Au

collisions is independent of quark mass.

Future measurements with the PHENIX Silicon Vertex Tracker will allow separation of charm and bottom $R_{AA}$. Since the heavy flavor electron $R_{dA}$ indicates rather small cold nuclear matter effects on the upsilon (within the transverse momentum range covered by this measurement), I expect that the bottom quark $R_{AA}$ will be similar in magnitude to the neutral pion $R_{AA}$ for $p_T < 9$ GeV/$c$.

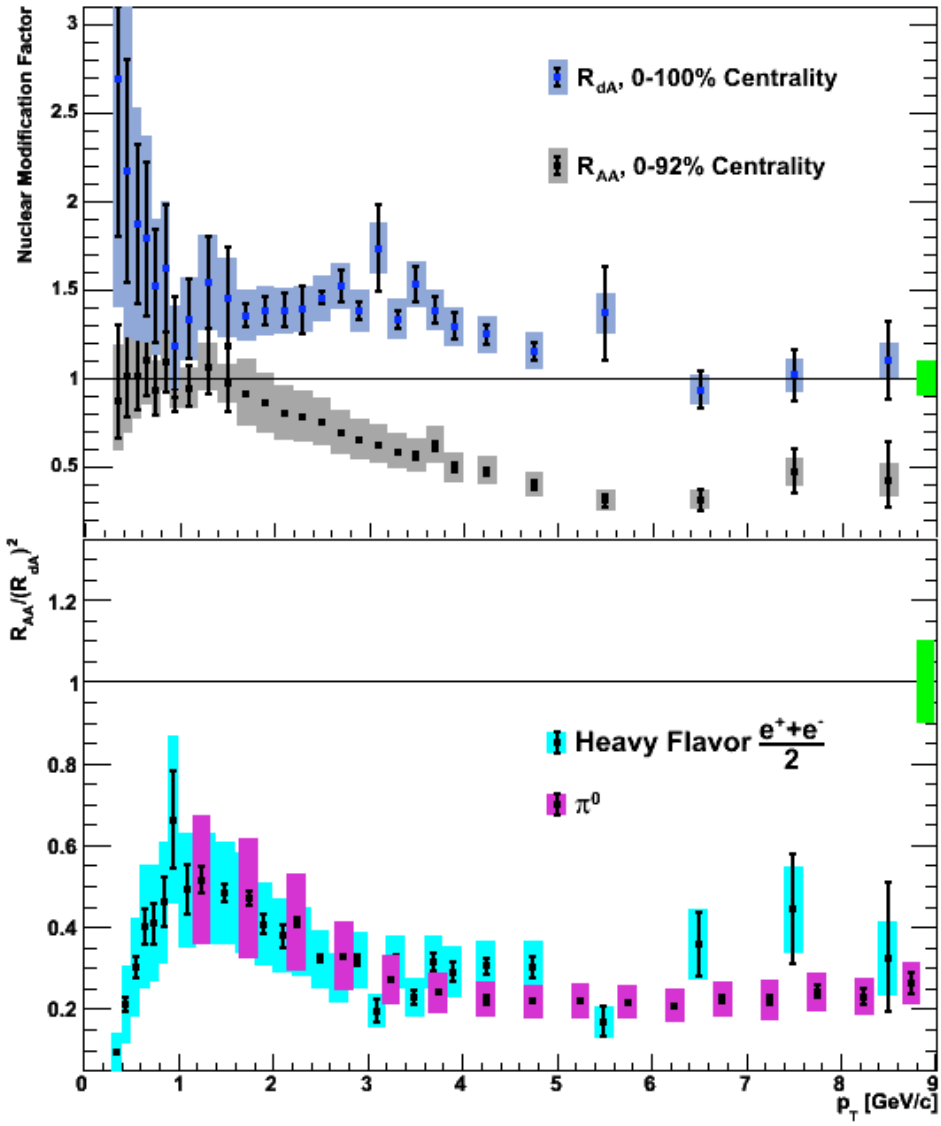


Figure 5.7: The nuclear modification factors $R_{AA}$ and $R_{dA}$ for Minimum Bias $d$+Au and Au+Au collisions. The ratio $R_{AA}/R_{dA}^2$ for this centrality is shown in the bottom panel for electrons from heavy quark decays and the neutral pion.

# Bibliography


[1] E.V. Shuryak, Phys. Repts. 61, 71 (1980).

[2] F. Karsch, Lect. Notes Phys. 583 (2002).

[3] K. Adcox *et al.*, Nucl. Phys. A757, 184 (2005).

[4] I. Arsene *et al.*, Nucl. Phys. A757, 1 (2005).

[5] B. B. Back *et al.*, Nucl. Phys. A757, 28 (2005).

[6] J. Adams *et al.*, Nucl. Phys. A757, 102 (2005).

[7] A. Adare *et al.* Phys. Rev. C 76, 034904 (2007).

[8] E. Wang, X.-N. Wang, Phys. Rev. Lett. 87 142301 (2001).

[9] Phys. Rev. C 77, 064907 (2008).

[10] S. Wicks, W. Horowitz, M. Djordjevic, M. Gyulassy, Nucl. Phys. A784, 426 (2007).

[11] Yu. L. Dokshitzer, D.E. Kharzeev, Phys. Lett. B519 199 (2001).

[12] T. Matsui and H. Satz, Phys. Lett. B178,(1986) 416.

[13] A. Adare *et al.* Phys. Rev. Lett. 98, 232301 (2007).

[14] R. L. Thews and M. L. Mangano, Phys. Rev. C73, 014904 (2006).

[15] Grandchamp *et al.*, Phys. Rev. Lett. 92, 212301 (2004).

[16] A. Adare *et al.* (PHENIX Collaboration), arXiv:1105.1966 .

[17] M. Cacciari, hep-ph/0407187 .

[18] D. Acosta *et al.* (CDF II Collaboration), Phys. Rev. Lett. 91, 241804 (2003)

[19] K. Nakamura *et al.* (Particle Data Group), J. Phys. G 37, 075021 (2010).

[20] M. Cacciari *et al.*, Phys. Rev. Lett. 95, 122001 (2005).

[21] A. Adare *et al.* (PHENIX Collaboration), Phys. Rev. Lett. 98, 172301 (2007).

[22] A. Adare *et al.* (PHENIX Collaboration), Phys. Rev. Lett. 97, 252002 (2006).

[23] A. Adare *et al.* (PHENIX Collaboration), Phys. Rev. Lett. 103, 082002 (2009).

[24] N. Armesto, *et al.*, Phys. Lett. B637, 362 (2006).

[25] G. D. Moore and D. Teaney, Phys. Rev. C71, 064904 (2005).

[26] H. van Hees, V. Greco, and R. Rapp, Phys. Rev. C73, 034913 (2006).

[27] P. K. Kovtun, D. T. Son, A. O. Starinets, Phys. Rev. Lett. 94, 111601 (2005).

[28] M. M. Aggarwal *et al.* (STAR Collaboration), Phys. Rev. Lett. 105, 202301 (2010).

[29] P. Sorensen and X. Dong, Phys. Rev. C 74, 024902 (2006).

[30] J. Adams *et al.* (STAR Collaboration), Phys. Rev. Lett. 92, 052302 (2004).

[31] J.J. Aubert *et al.* (EMC Collaboration), Phys. Lett. 123B, 275 (1983).

[32] M. Arneodo, Phys. Rep. 240 (1994) 301.

[33] K. J. Eskola, V. J. Kolhinen, R. Vogt, hep-ph/0104124.

[34] J. W. Cronin *et al.* Phys. Rev. D11, 3105 (1975).

[35] S.S. Adler *et al.* (PHENIX Collaboration), Phys. Rev. C 74, 024904 (2006).

[36] A. Adare *et al.* (PHENIX Collaboration), arXiV:1010.1246 .

[37] D. Kharzeev and K. Tuchin, Nucl. Phys. A735, 248 (2004).

[38] K. J. Eskola, H. Paukkunen, and C. A. Salgado, JHEP04, 065 (2009).

[39] R. Vogt (2005), nucl-th/0507027.

[40] K. Tuchin, hep-ph/0705.2193.

[41] S.S. Adler *et al.* (PHENIX Collaboration), Phys. Rev. Lett. 98, 172302 (2007).

[42] S.S. Adler *et al.* (PHENIX Collaboration), Phys. Rev. Lett. 96, 202301 (2006).

[43] S.S. Adler *et al.* (PHENIX Collaboration), Phys. Rev. Lett. 98, 012002 (2007).

[44] S.S. Adler *et al.* (PHENIX Collaboration), Phys. Rev. Lett. 94, 232301 (2005).

[45] M. Leitch, *PHENIX Run-8 Summary*, presented at the 2008 RHIC Retreat, March 2008.

[46] J. Alessi *et al.*, *Construction of the BNL EBIS Preinjector*, PAC09, Vancouver, p. 407 (2009).

[47] C. Adler *et al.*, Nucl. Instr. and Meth. A 470 (2001) 488.

[48] K. Ikematsu *et al.*, Nucl. Instr. and Meth. A 411, 238 (1998).

[49] M. Allen *et al.*, Nucl. Instr. and Meth. A499 549-559 (2003).

[50] S.S. Adler *et al.* (PHENIX Collaboration), Phys. Rev. C77, 014905 (2008).

[51] S.H. Aronson *et al.*, NIM A499 480-488 (2003).

[52] K. Adcox *et al.*, NIM A499 489-507 (2003).

[53] M. Aizawa *et al.*, NIM A499 508-520 (2003).

[54] Y. Akiba *et al.*, *Ring imaging Cherenkov detector of PHENIX experiment at RHIC,* in Proc. of the Third Inernational Workshop on Ring Imaging Cherenkov Detectors (RICH98), Ein-Gedi, Israel, 1998.

[55] S. C. Johnson *et. al, Three-Dimensional Track Finding in the PHENIX Drift Chamber by a Combinatorial Hough Transform Method*, in Proc. of Int. Conf. on Computing in High-Energy Physics (CHEP '98), Chicago, IL, 1998.

[56] L. Aphecetche *et al.*, NIM A499 521-536 (2003).

[57] W. Anderson *et al.*, arXiv:1103.4277

[58] Y. Akiba, R. Averbeck, A. Dion, F. Kajihara, PHENIX Internal Analysis Note 557.

[59] M. Brooks *et al.*, *Management Plan for the Forward Silicon Vertex Tracker for PHENIX*

[60] G. David *et al.*, IEEE Trans. Nucl. Sci. 47 (2000) 1982.

[61] Y. Riabov (PHENIX Collaboration), J. Phys.G34, S925 (2007).

[62] J. Almeida *et al.*, Nucl. Instr. and Meth. A361 (1995) 524.

[63] F. Cusanno *et al.*, Nucl. Instr. and Meth. A502 (2003) 251.

[64] F. Cusanno *et al.*, Nucl. Instr. and Meth. A525 (2004) 163.

# Appendix A

# HBD

This section details the testing and assembly procedures used in the construction of the Hadron Blind Detector. For a full account of the HBD performance, see [57].

### A.0.1 GEM Testing

To ensure a dust and water-free environment, GEMs are stored under high vacuum. A turbo-molecular pump is used to generate vacuum in the low $10^{-6}$ Torr range. Prior to insertion in vacuum, each GEM is further washed and tested. GEMs are gently sprayed with deionized water for ∼30 seconds, followed by a rinse with clean isopropyl alcohol. The GEMs are then blown dry with compressed gas that was passed through a gas ionizer to facilitate removal of any dust particles. The GEMs are then placed in high vacuum for 24 hours to ensure removal of all moisture from the kapton and FR4 frames. GEMs that contain moisture are found to have large leakage currents (on the order of a few $\mu$A at $dV = 100$ V). This washing process is repeated on any GEMs which develop anomalously high leakage current and successfully recovers ∼30% of these GEMs. After drying in vacuum, each GEM is moved to a high voltage test station on a laminar ow table with an ISO Class 1 atmosphere. Three electrical tests are then performed in air:

1. The leads of each GEM are checked to have continuity to the top or bottom of the GEM. This is most easily tested by confirming the capacitance of the GEM through the leads with a hand-held multimeter.

2. Each individual strip on the top side of the GEM is tested for continuity through the resistors to the HV input trace. With the bottom of the GEM grounded, the top side of the GEM is raised to -100 V. A voltage probe is used to determine that the proper voltage is present on each

of the 28 strips on the top side of the GEM. During this process, the leakage current is carefully monitored. GEMs drawing less than 5 nA are accepted.

3. High voltage is finally applied to the GEM to monitor stability and leakage current. A current limit of 1 $\mu$A is set on the power supply to limit damage to the GEM in the event of a discharge. With the bottom side of the GEM grounded, the top side is slowly brought to 550 V. GEMs that are stable and have leakage currents less than 5 nA are accepted. GEMs which initially display moderately high leakage currents ($\sim$10-500 nA), but no discharges, are left at voltage for up to an hour. Often the current falls back into the acceptable range.

GEMs that pass these tests are returned to high vacuum for storage, while those that fail are rewashed and tested again. GEMs which continue to fail after two cycles of washing are not used in the HBD.

### A.0.2 Copper GEM Assembly

All GEMs are dust sensitive and must be handled in a clean room or (preferably) upon a laminar ow table. Once coated with CsI, the devices are also water sensitive and will lose their quantum effciency if exposed to an atmosphere with high water concentration for an extended period of time. For this reason, CsI-coated photosensitive GEMs are handled in the inert atmosphere of a glovebox. Unfortunately, since a glovebox is a closed-loop system it cannot maintain the level of cleanliness found on the laminar table. Because of this, strategies that minimize handling of the HBD (and GEMs) in the glovebox were found to produce the best results. The most successful procedure for HBD assembly involved assembling the bottom two layers of all GEM stacks in the cleanest available environment (the laminar flow table), and then adding the CsI-coated GEMs in the dry glovebox environment. This procedure limited exposure to the glovebox environment to 2-3 weeks. For installation of the Cu GEMs, the HBD vessel is mounted on a rotating fixture and placed in front of the laminar ow table. With clean air blowing through the interior of the vessel, the standard copper GEMs (two per module) are mounted in place over the readout pads as shown in Fig. 2.19. After mounting, each GEM is re-tested in situ for continuity and stability (tests no. 1 and 3 above) to ensure no damage was caused during installation.

Once all standard GEMs are installed and re-tested, the vessel is moved into a sealed glovebox to accept the CsI-coated gold GEMs at the top of the triple- GEM stack. Once sealed, the glovebox recirculates nitrogen through

a purifier and achieves H2O concentrations of $< 10$ ppm. Regular sweeps of the interior of the glovebox with an ULPA vacuum cleaner mounted inside the glovebox atmosphere ensure that particulate contamination is at an acceptable level. One critical choice for the glovebox was the selection of the material of the gloves themselves. While Butyl gloves provide the best water barrier, they are not highly rated with regard to generation of particulate matter. Hypalon gloves were selected as having the best rating for particulate matter, and were found to elevate the baseline water concentration of an empty glovebox from 2-3 ppm to 7-8 ppm, which was still quite acceptable.

### A.0.3 Evaporation of CsI onto Au plated GEMs

GEMs are made photosensitive by the evaporation of a thin layer of CsI on the GEM electrode surface. This layer is not chemically stable on a copper substrate since CuI is more tightly bound than CsI. For this reason, a special subset of the GEM production included GEMs whose metallic surface was overlayed with Ni (diffusion barrier) and then Au (chemically inert layer) [62]. Not surprisingly, these GEMs were seen to have identical gain and voltage stability characteristics as the standard copper GEMs and were handled in an identical manner during the testing and framing stages performed at the Weizmann Institute of Science. Reflective photocathodes exhibit a quantum effciency that saturates as a function of the cathode thickness. For CsI, this saturation point is found at $\sim$200 nm thickness. HBD photocathodes were made to have 300 nm thickness to ensure full sensitivity in spite of possible non-uniformities of the coating. GEM photocathodes are manufactured at Stony Brook by evaporating a $\sim$300 nm- thick layer of CsI to their top surface using an evaporator that was on loan from INFN [63]. The evaporator was used many times in the past to evaporate photocathodes for RICH detectors used in CEBAF Hall A kaon experiments [64] and is of sucient size to evaporate 4 HBD photocathodes simultaneously. Gold GEMs are mounted four at a time into a sealed transfer box and placed into the evaporator for CsI photocathode deposition. Additionally, several small (2 cm $\times$ 2 cm) Cu-Ni-Au circuit cards (called chicklets) are also mounted into the box to be used as a monitor of the quantum efficiency (QE). Once in the evaporator, the lid of the transfer box is removed to expose the GEMs. The evaporator is pumped down to a vacuum of $2 \times 10^{-8}$ Torr with a combination of a turbopump and a cryopump. While pumping, the transfer box containing the GEMs is heated to 40C to drive off water and other contaminants. Facing each GEM is a molybdenum crucible with a single piece of CsI weighing 0.8 g. Once ultra high vacuum is achieved, the crucible is resistively heated to vaporize the CsI. A quartz thickness monitor positioned near the GEM surfaces is used to determine the

deposition rate of the CsI. By varying the current through the crucibles, the rate is kept near 1 nm/s. The final thickness of the CsI layer is typically ∼300 nm. After CsI deposition, the transfer box is moved to the QE measurement section of the evaporator. It was observed that the QE of newly deposited photocathodes can change (typically improve) by a factor of ∼2 over a period of ∼8 hours, so the measurement is not performed until this time has passed. A deuterium lamp shines through a 160 nm filter, enters the vacuum via a $MgF_2$ window, and shines onto a movable mirror. This mirror can be rotated to allow the light to be directed either onto the GEM surface or onto a reference phototube of known QE. Once the light source has been calibrated using this phototube, the QE of the new CsI photocathode can be determined relative to the tube. A mesh with 300 V is used to draw photoelectrons from the CsI surface, which is measured as current by a picoammeter. The transfer box and phototube can both be translated inside the evaporator, allowing a scan of the entire surface of each photocathode. This measurement ensures the photo-sensitivity of each cathode across its entire surface, but only at a single wavelength. The small chicklets are later transferred to Brookhaven National Laboratory, where a scan across the wavelength range 120 nm to 200 nm is performed using a vacuum photospectrometer. It was found that every evaporation during the entire history of the project produced identical photo-sensitivity and uniformity.

### A.0.4 Installation of GEM Photocathodes

After the QE scan, the evaporator is backfilled with ultra high purity argon up to atmospheric pressure. The transfer box containing the gold GEMs with CsI photocathodes is then sealed in the argon atmosphere before the evaporator chamber is opened to air. The sealed transfer box is put into the glovebox through a load-lock system, which prevents any room air from entering the glovebox. The transfer box is not opened until it is inside the dry nitrogen atmosphere of the glovebox, ensuring that no humidity affects the photocathodes.

The glove box is set up in three modules, each with a distinct purpose. The first module has the rail system that accepts the transfer box from the evaporator, with a winch mounted on the ceiling to lift the transfer box lid. The second module serves as the high voltage testing station for the gold GEMs after CsI deposition. Here the gold GEMs undergo all the above mentioned electrical tests, with the exception that the voltage in step 3 is decreased from 550 V to 500 V in the nitrogen atmosphere of the glove box. It is common for a gold GEM to exhibit several discharges upon the first application of high voltage after CsI deposition, but stabilize afterwards. Rarely a gold

GEM exhibits a short or anomalous leakage current after deposition. If so, it is washed and the testing/deposition process is repeated. The third station houses the HBD vessel. The vessel is mounted in a rotating fixture that can be turned to allow access to the edge modules (normally out of reach of the gloves). After the gold GEMs are mounted, all three GEMs in a stack are tested in situ under high voltage. The mesh is then installed over the stack, and 500 V is applied across the drift gap to ensure that there is no electrical continuity between the GEM and mesh. A completed HBD vessel is shown in Fig. A.1. The irredescent color of the GEM surfaces is created by the CsI coating.

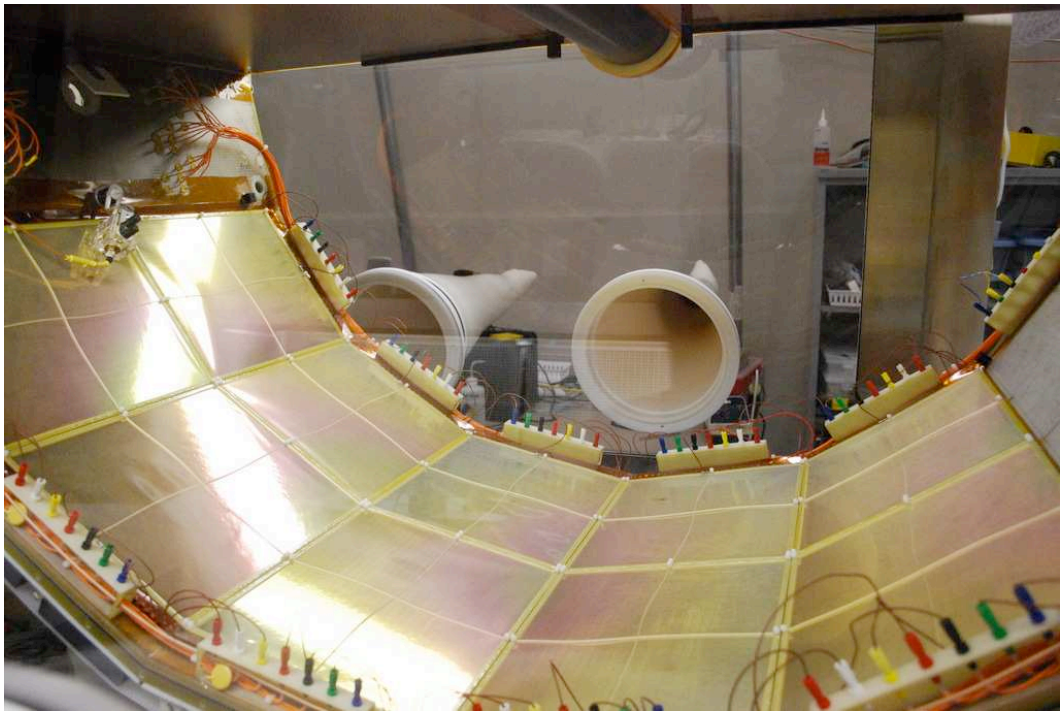

Figure A.1: A complete HBD in the glovebox following installation of all photocathodes.

Once all the interior components of the HBD are assembled, final tests are done to ensure that the device is fully functional. Each GEM is tested by measuring the capacitance across its HV input leads, and finally for high voltage stability. Following these tests, the sides of the vessel are installed while the vessel is still inside the glovebox, sealing the dry nitrogen atmosphere inside. The vessel is then brought out of the glovebox and onto a test bench, and purged with $CF_4$.